Engineering Hard-Soft Interfaces: Insights from the Root-Soil Interaction for Bioinspired Design

By

Giulia Ricci

Student number: 5450896

Thesis Manuscript

in partial fulfilment of the requirements for the degree of

Master of Science

in Biomedical Engineering and Mechanical Engineering

at the Delft University of Technology

Daily supervisor:

Lorenzo B. Kunkels TU Delft

Under supervision from:

Dr. Mohammad J. Mirzaali TU Delft

Dr. Angelo Accardo TU Delft

October 31, 2024

Abstract

A hard-soft interface refers to the boundary between two materials or regions with significantly different mechanical properties, where one is rigid or hard and the other is flexible or soft. These interfaces are common in both engineered and natural systems and are characterized by the contrast in how each material deforms, transfers loads, or responds to environmental stress. Engineered hard-soft interfaces often experience failure due to high interfacial stresses, poor adhesion, and localized stress concentrations caused by mismatched mechanical properties. An example of engineered hard-soft interfaces can be found in tissue engineering, where they are used to replicate natural transitions between tissues, such as those between bone and cartilage. In contrast, hard-soft interfaces in nature, such as the root-soil system, demonstrate remarkable strength and adaptability, efficiently distributing loads and reducing stress concentrations despite differences in material properties.

The pull-out force was chosen to assess the strength of the root-soil interface, capturing the mechanical interactions of roots with their environment. This study focused on barley and mung bean seeds, chosen for their distinct root structures, barley with a fibrous system and mung bean featuring a taproot system. Over a 15-day growth period, various root characteristics such as length, diameter, tortuosity, and branching patterns were analyzed across soil and hydrogel substrates, each with distinct material properties and stiffness. The methodology included measuring growth in terms of days and stem height, along with 2D root trait extraction to analyze characteristics such as length, diameter and number of branches. Additionally, 3D computed tomography (CT) scanning was used to visualize root architecture, while pull-out tests provided key data on resistance and force-displacement curves, and finite element method (FEM) simulations enabled sensitivity analyses of various root structure configurations in a non-destructive manner. Lastly, experiments with hydrogel tested its viability for root growth, involving detailed protocols for hydrogel composition and seed preparation.

Plant growth measurements revealed a consistent increase in stem height over time, effectively captured by the logistic growth model. Laboratory pullout tests and root extraction demonstrated that increases in root characteristics such as length, diameter, and branching significantly improve pullout force in both barley and mung bean seeds. Moreover, pullout test results showed that barley roots have greater mechanical resistance and higher maximum forces than mung bean roots, although with greater variability in the data. FEM simulations indicated that a 45° vertical branching angle yielded the highest pullout force for barley in soil (5.09 N), while an 80° angle was most effective in hydrogel (4.98 N). In contrast, radial branching angles had negligible effects in both substrates. Tortuous root configurations significantly increased pullout force in soil, nearly doubling it from 5.09 N for straight roots to 9.80 N, but only slightly improved it in hydrogel, from 3.20 N to 3.61 N. The addition of branches in mung beans significantly increased pullout forces in both substrates due to the greater surface area, which enhanced root-substrate interaction. The FEM simulations showed that pullout forces were generally higher in soil due to its rigidity, which leads to a rapid increase in pullout force until root failure. Hydrogel, with its elastic properties, allowed roots to stretch more under load, providing uniform and gradual resistance. The FEM model was also validated through energy history output results and mesh convergence analysis. Lastly, initial experiments growing roots in hydrogel show promise for this substrate as a soil alternative, however further research is required to optimize its properties for plant growth.

Overall, this study provides a better understanding of the factors optimizing root anchorage and interface strength, offering design strategies for bioinspired engineered hard-soft interfaces. It also emphasizes the need to tailor natural design principles to the specific material properties of substrates in engineered contexts.

KEY WORDS: Root-Soil Interface, Root-Hydrogel Interface, Pullout Tests, Root Geometry, Root Architecture, Mechanical Properties, Hydrogel Soilless Substrate, CT Scanning, FEM Analysis

Contents

List of Figures

List of Tables

1. Introduction

1.1. Background and Research Significance

Hard-soft interfaces are boundary regions where materials with different mechanical properties, rigid (hard) and flexible (soft), come together. These interfaces combine the strength of rigid materials with the adaptability of softer ones [1]. Artificially creating strong hard-soft interfaces has diverse applications across several fields. For instance in biomedical engineering, particularly in tissue engineering, these interfaces are used to mimic natural transitions between tissues, such as bone and cartilage. The goal is to aid soft tissue regeneration by creating surfaces that guide cell growth and support tissue repair [2]. However, these interfaces often pose challenges due to the contrasting mechanical properties involved, which can become points of potential failure. Significant differences in material properties can lead to high interfacial stresses and uneven deformation, both of which increase the likelihood of crack propagation and failure. Additionally, mismatched properties may result in poor adhesion, further raising the likelihood of failure at the interface [3].

Despite extensive efforts, engineered constructs often fall short of replicating the efficiency of natural hard-soft interfaces, which have evolved over millions of years to form highly adapted connections where rigid structures seamlessly integrate with flexible ones. Hard-soft interfaces in nature are characterized by remarkable mechanical performance, often experiencing minimal failures at the interface despite the presence of mechanically mismatched biomolecular tissues [1]. The robustness of natural soft-hard tissue interfaces comes from their gradual transitions in composition and structure, which reduce stress concentrations and prevent failure [4]. These transitions integrate inorganic and organic elements across multiple hierarchical scales, from nano to meso, creating a resilient design [5]. Examples that illustrate the seamless integration of hard-soft interfaces in living systems include the squid beak, the crab exoskeleton and the root-soil interface. The beak, known as one of the hardest and stiffest entirely organic materials, is deeply embedded within the soft buccal envelope and exhibits a significant stiffness gradient from its stiff tip to its compliant base [3, 6, 7]. The crab exoskeleton comprises various layers, including the exocuticle, which forms the outer layer and is characterized by notably high stiffness and hardness, and the endocuticle, the inner layer, which exhibits significantly lower stiffness and hardness [8]. Soil and roots form a composite material with enhanced mechanical properties that benefit slope stabilization, soil structure improvement, and water management, contributing to overall environmental stability [9].

Among natural hard-soft interfaces, this study focuses on the root-soil interface because it offers valuable insights for engineered applications. The root-soil interface is a dynamic system where roots continuously adapt to different soil types and changing environmental conditions [10]. Mechanically, this interface demonstrates resilience, withstanding environmental stressors such as strong winds and rainfall through adaptive anchoring [11]. Additionally, the root-soil interface features a hierarchical structure, from fine root hairs to larger roots, which optimizes transitions in material properties and efficiently distributes mechanical loads across the network [12]. Among all aspects of the root-soil interface that could be studied, the focus will be on the pullout force of root systems, a key measure of interface strength, indicating the maximum force required to extract roots from soil [13]. Factors such as root geometry and architecture have a much greater influence on pullout force compared to microscopic interactions or material properties [9]. Understanding how root geometry and architectural characteristics contribute to the mechanical resilience of the root-soil interface can inspire design strategies for engineered hard-soft interfaces, reducing their likelihood of becoming the weak points of a system.

In addition to root characteristics, the surrounding substrate properties significantly impact the strength of the root-soil interface [14, 15]. This study also explores how variations in substrate stiffness and material properties affect interface strength by comparing soil to an alternative medium, such as hydrogel, and determinate whether traits that strengthen the interface in soil have a similar effect in a mechanically distinct substrate. Hydrogel was chosen as an alternative to soil for its versatile properties, including tunable 3D structure and mechanical characteristics. Its architecture can be modified to mimic complex natural geometries, while its mechanical properties, such as stiffness and degradation rate, can be tailored by adjusting its chemical composition and crosslinking density [16, 17]. Furthermore, as a hydrophilic polymer with a three-dimensional network, hydrogel provides a porous structure where water fills the interstitial spaces, creating an environment that supports root growth with access to air, water, and nutrients [18, 19].

To investigate these aspects, pullout tests will be conducted to experimentally measure the pullout force of roots in soil. Root extraction and computed tomography (CT) scans will be used to analyze and extract both 2D and 3D root geometry and architectural characteristics. Specifically, CT scans will be combined with automated segmentation using a deep learning method. Finite Element Method (FEM) simulations will also be employed to numerically evaluate the pullout force of root structures in both soil and hydrogel substrate. Models for the simulations will be developed from CT scan data to ensure accuracy. Finally, roots will be grown directly in hydrogel to explore its potential as a soil substitute, allowing for future experimental tests on root structures in this medium.

1.2. Research Question and Objective

This study aims to gain new insights from natural interfaces like the root-soil interaction to improve the design of engineered hard-soft interfaces and address existing challenges. Extensive research on the root-soil interface has examined how individual root shapes, structures, microscopic elements, material properties, and soil characteristics influence tensile strength of the composite root-soil material. Employing a multidisciplinary strategy, these studies integrate field experiments, laboratory tests, numerical simulations, and imaging techniques. While numerous studies have effectively isolated specific factors such as root length, diameter, and tortuosity in 2D to determine their impacts on pullout force, a significant gap remains in the understanding of 3D root traits. Most investigations into 3D root morphology depend on mathematical models, which often fail to accurately replicate actual root structures, thus challenging the validation of these models [15].

While soil has traditionally been the focus in studying root-medium interactions, recent interest has shifted toward alternative growth media, such as hydrogel, to better control environmental variables and observe root behavior [20]. Studies investigate how hydrogel contributes to plant growth by stabilizing nutrient release, altering water availability, and creating beneficial structural gradients within the soil matrix [21-23]. In these applications, soil remains the principal substrate, with hydrogel added to modify and tailor the growth environment to meet specific research objectives. Although many studies focus on using hydrogel as an additive to soil to boost agricultural performance, research on its effects as a soilless substrate is limited. In particular, few investigations have examined its impact on plant growth or the strength of the root-hydrogel interface [18]. Most studies examining interface strength have used soil or sand, or a mix of soil and hydrogel, to assess the effects of hydrogel on slope stability [24]. When hydrogel alone is tested, the focus is typically on evaluating its material properties through shear and pullout tests [25, 26].

However, despite these studies, significant gaps remain in the current literature. For soil-based studies, there is a need to experimentally investigate how 3D root traits influence pullout force, rather than relying only on mathematical models. For hydrogel, it is necessary to investigate whether roots can grow in it as a soilless substrate. Additionally, in the context of pullout testing, studies have predominantly focused on natural substrates like soil or sand. This creates a notable gap, as the interface strength between root systems and alternative substrates such as hydrogel has not been explored. Furthermore, there is limited understanding

of how root traits that increase the interface strength when soil is the medium, might translate to or interact with non-natural medium like hydrogel.

Based on the identified research gaps, the global research question and its corresponding subquestions are formulated as follows.

Global Research Question: What driving factors, including root geometry, 3D root architecture, and changes in substrate stiffness and material properties, affect the strength of the root-soil interface and could inspire the design of bioinspired engineered hard-soft interfaces?

Subquestions:

1. Root-Substrate Interface Mechanics:
    a. How do 3D root traits influence pullout force and overall interface strength within a substrate?
    b. What are the key mechanisms by which these 3D root traits improve the mechanical strength of the root-substrate interface?
    c. How do specific root traits contribute to strain and stress distribution within the substrate during pullout tests?
2. Comparative Analysis of Soil and Hydrogel:
    a. How do root traits that improve interface strength in soil translate in hydrogel?
    b. What are the material properties of hydrogel that affect its interaction with roots, and how do these differ from soil?
    c. What are the similarities and differences in stress and strain distribution patterns in soil versus hydrogel during root pullout?
3. Engineering Applications:
    a. Which specific insights from root-soil and root-hydrogel interactions are most applicable to designing engineered hard-soft interfaces?
    b. How can findings on root-substrate interface strength inform the development of bioinspired materials and structures in engineering?
4. Hydrogel as a Growth Substrate:
    a. Can seeds grow in hydrogel when used as a soil substitute?
    b. What protocols need to be developed to support root growth in hydrogel?
    c. What nutrients, hydration levels, and environmental conditions support optimal root growth in hydrogel?

1.3. Thesis Structure

This thesis is organized into five main chapters that comprehensively cover the study of engineered hard-soft interfaces inspired by natural systems. The first chapter introduces the concept of engineered and natural hard-soft interfaces, setting the stage for the subsequent investigation. The second chapter details the methodologies employed in this research, including seed planting, pullout testing, computed tomography (CT) scanning, finite element method (FEM) simulations, and hydrogel preparation, ensuring a detailed understanding of the experimental and simulation approaches used. The third chapter presents the results obtained from these methods, providing numerical data as well as plots and images to illustrate the quantitative and qualitative aspects of the findings. In the fourth chapter, the discussion begins with an analysis of each result, offering a thorough examination of the findings. It also explores how these insights contribute to the overarching research question. Finally, the concluding chapter synthesizes the research outcomes, reflects on the contributions to the field and suggests potential directions for future research. Each chapter is designed to build upon the previous one, gradually unfolding the research narrative and leading to comprehensive conclusions. Lastly, the appendices provide all the figures and tables which support the data and analyses presented in the main text, offering additional detail and resources.

2. Methodology

The methodology used in this project combines several practices, which are described in detail below to ensure they are easily reproducible and comparable. First, the process of seed preparation and planting is outlined, designed to ensure sample homogeneity and maximize repeatability. Next, the pullout tests are presented, conducted to study and evaluate the complex interactions between roots and soil during pullout tests. The materials and methods used for these tests were selected to simulate the natural interaction between soil and roots as accurately as possible, while also allowing for precise and controlled measurements. These tests provide important information, such as pullout resistance, which is the maximum force required to extract the root from the soil, and force-displacement curves, which illustrate how the pullout force varies with root displacement.

The methodology for CT scanning and automated segmentation using a deep learning method is then described. This approach enables intact 3D visualization of root architecture within natural soil, providing valuable insights into the root system's morphological characteristics, such as root position and orientation. The models used in the FEM simulations are based on data extracted from the CT scans, including the number and orientation of the roots. These simulations enable sensitivity analysis of various root structure configurations, providing a non-destructive method for studying interface strength [27]. Lastly, the methodology for selecting the correct hydrogel composition is described in detail, along with the protocol for seed preparation and insertion.

2.1 Planting Seeds

2.1.1 Seeds and Soil Type

For the experiments, two types of seeds were chosen: barley and mung beans. Both seeds germinate and grow rapidly, with barley showing visible germination within 5 days and mung beans typically germinating within 2 to 5 days, allowing for quick testing and results [28, 29]. Additionally, they are easily accessible and generally inexpensive, which is important for repeated experiments. These two seed types develop completely different root systems from a morphological perspective. Mung beans develop a taproot system, characterized by a prominent primary root with a single, dominant axis. This primary root develops numerous lateral roots that extend outward, as shown in Figure 1a and b. In contrast, barley seeds develop a fibrous root system, which lacks a dominant primary root. Instead, the root system consists of numerous fibrous roots branching out in various directions. In Figure 1c, the typical structure of 14-day-old barley roots can be seen. Type A roots are called seminal roots, while Type B roots are known as adventitious roots. Seminal roots emerge early, right after the germination stage, whereas adventitious roots develop later during plant growth. Adventitious roots arise from the crown nodes of the main shoot and tillers, which are specialized parts of the plant's stem that grow at the base [30]. Overall, taproot systems display a clear hierarchy with a primary root and lateral branches, while fibrous root systems lack this hierarchy and spread out in a network-like style [31].

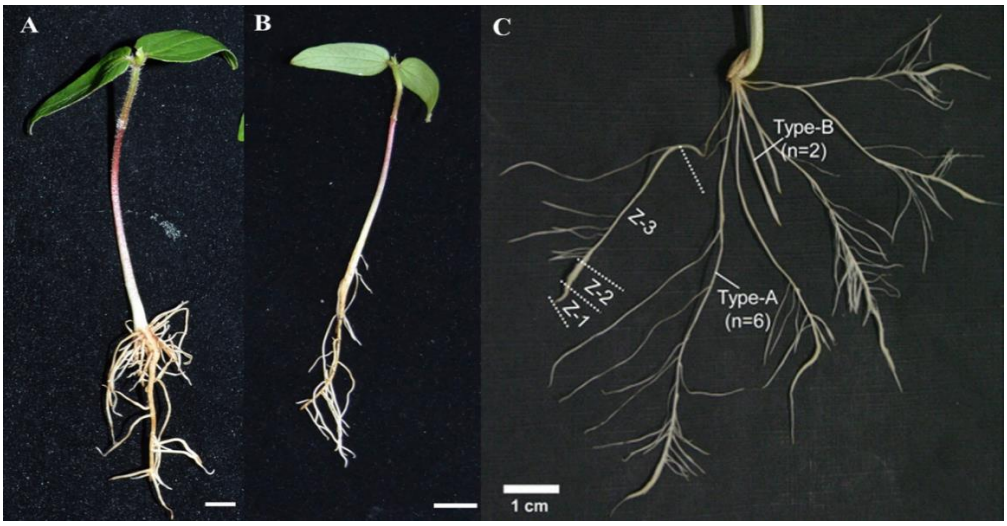

Figure 1: A-B) Pictures of mung beans roots [32], C) Picture of barley roots [33].

Regarding the type of soil used for planting, it was decided to use universal potting soil. This decision was made for several reasons. First of all, universal potting soil is easily accessible and offers a standardized substrate. By minimizing variables related to soil composition, it improves the reproducibility of experiments [34]. Additionally, it is generally formulated to provide a balanced mix of nutrients suitable for a wide range of plants and has a structure that supports both drainage and water retention. This is important for root growth, as it helps prevent waterlogging while ensuring proper air circulation [35]. The specific product information is summarized in Table 16, which can be found in the appendices.

2.1.2 Protocol

The seed planting protocol involved the use of truncated cone-shaped pots with a diameter of 59 mm at the top, 47.8 mm at the base, and a height of 67.5 mm, corresponding to an internal volume of approximately 151.73 cm^3. Prior to planting, seeds were soaked in water for 8 to 12 hours to accelerate germination. The universal potting soil was first sieved using a sieve with 2mm openings to minimize clumps, ensuring that the maximum clump size expected is 2mm. Each pot was filled with 28 g of universal potting soil, occupying approximately 94.41 cm^3 (corresponding to a pot height of 42 mm), which is about 62% of the pot's internal

volume. The soil was then compacted to occupy 71.93 cm^3 (corresponding to a pot height of 32 mm), or about 47% of the internal volume, resulting in a soil density of 0.39 g/cm^3. After leveling the soil, 15 mL of water was added to moisten it. This step was performed before placing the seed to prevent displacement during sowing. Seeds were planted at a depth of 1 cm in the center of the pot, then lightly covered with soil and gently pressed down to ensure proper contact between the seeds and soil. The pots were placed under artificial grow light, following a consistent 12-hour light cycle to replicate spring/summer daylight conditions, which are favorable for plant growth. The environmental conditions were maintained at an average temperature of 20°C with a relative humidity of 40%. Watering was carried out once a week with 15 mL of water, starting on the day of planting, to provide consistent moisture for seed germination and growth.

2.1.3 Growth Measurement and Root Observation

Barley seeds were planted, and the correlation between stem height and days of growth was investigated by recording measurements over time. A total of 18 samples were measured at four specific time points: 3, 5, 6, and 12 days after planting. These time points were chosen based on observed growth patterns. Day 3 was selected because it marked the first visible appearance of stem growth; before this, during the first two days, stem development is typically not observable. The intermediate days, 5 and 6, were included to capture the progression of growth between the early and later stages. Day 12 was chosen as the final point for measurement because by this stage, the roots had extended significantly, becoming visible at the bottom of the pot. When roots reach the bottom of the pot, they can become root-bound, meaning they run out of space to grow properly. This can limit the plant's access to nutrients and water, affecting its overall health and growth. Additionally, in an experiment, it could lead to unnatural growth patterns that might distort the results.

Similarly, the same process was followed for mung bean seeds. For these, a total of 8 samples were measured over three time points: 5, 7, and 15 days after planting. The time points were chosen based on the same reasoning as for barley, however mung beans typically do not sprout until around day 4 or 5, making it difficult to observe stem growth earlier. By day 15, the roots become highly visible at the bottom of the pot, while day 7 was selected as an intermediate point.

After measuring the stem height, a few samples from both barley and mung bean seeds were carefully removed from the soil and cleaned. This provided a visual reference to observe how the roots changed and developed over time.

2.2 Pullout Test

2.2.1 Pullout Testing Apparatus

The tensile test machine used in the experiments is the Lloyd LR5K, a dual-column, tabletop tensile test machine. The technical specifications of tensile testing machine can be found in the appendices in Table 17. It features an easy-to-use control panel that provides the operator with all the necessary information for conducting simple tests. The machine uses a load cell to measure force and a displacement sensor to track the movement. Grips and attachments specific to the test can be secured to the machine with a rivet.

Several considerations were made when designing the final attachment system for the experiment. The pot needed to be firmly fixed in place to prevent any movement during testing, and the soil had to be restrained to avoid it being lifted or escaping from the pot while the roots were being pulled. Additionally, the system required adjustable height for the component holding down the soil, as slight differences in soil height may occur between samples. The machine had to be properly calibrated to ensure that the weight of any components used during the experiment would not affect the force measurements. It was also important to design a setup that would prevent any damage to the roots during the preparation phase, as even minor damage could invalidate the test results.

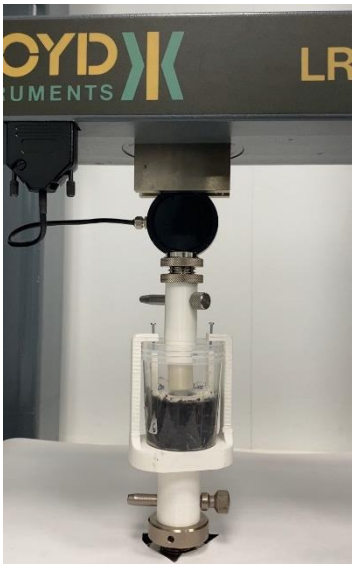

Figure 2: Set up of tensile test machine Lloyd LR5K for laboratory pullout testing.

The final setup, shown in the Figure 2 and rendering of Figure 3, with and without the pot, consists of five components. The technical drawing of the each component and the assembly is presented in the appendices, from Figure 38 to Figure 43. At the top of the setup, the connector (Part 1) links directly to the tensile machine and extends into the grip component (Part 2), which is specifically designed to hold the root securely without causing damage. Instead of using clamping methods which could crush the root, the grip component utilizes an adhesive method through an opening to affix the root, ensuring its integrity based on prior research recommendations [36-38]. Part 3 acts as a stabilizing connector that locks the base plate (Part 4) in place, providing a firm foundation for the pot. This base plate ensures the pot remains stationary during testing. Attached to the base plate, the retainer (Part 5) holds the soil within the pot, preventing any uplifting of soil that could affect the test's outcome. This setup is made to keep the root and soil stable and in place during the tensile test, making sure the results are accurate and reliable. All the components mentioned are securely connected to each other using screws or rivets. Lastly, Table 1 provides all the necessary information for producing the components used in the setup, which were 3D printed using the Ultimaker 3+ printer.

Table 1: 3D Printing Parameters for Manufacturing Components of the Tensile Test Machine.

Category	Details
Printer	Ultimaker 3+
Filament	Generic PLA
Nozzle Size	0.04 mm
Resolution	0.1 mm
Infill Density	40%
Infill Pattern	Lines
Shell Thickness	0.8 mm
Support Type	Normal (when needed)

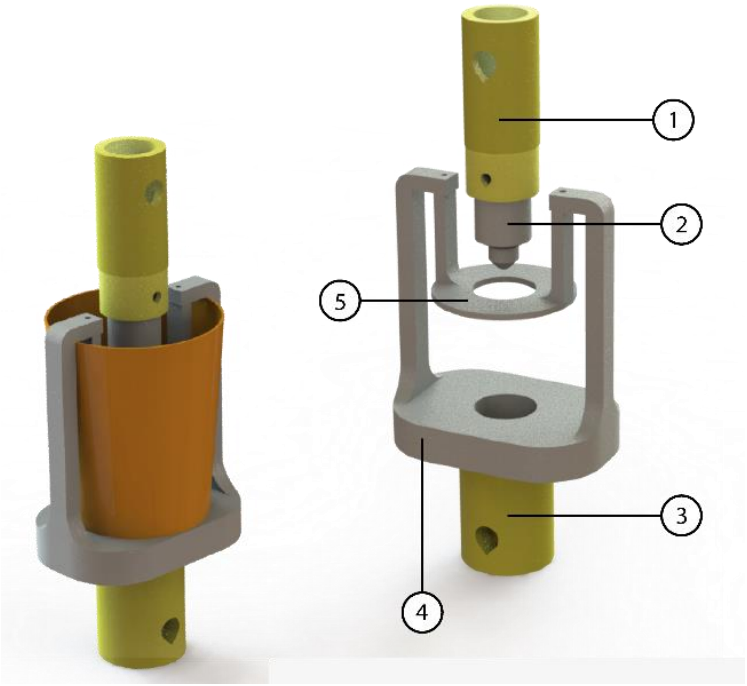

Figure 3: Rendering of the final setup selected, with and without the pot. The setup consists of five components: Part 1 (Connector), which links directly to the tensile machine and extends into Part 2 (Grip), designed to hold the root securely. Part 3 (Stabilizing Connector) locks the base plate (Part 4) in place, ensuring stability, while Part 5 (Retainer) holds the soil within the pot, preventing any uplifting during testing. All components are securely connected using screws or rivets.

2.2.2 Testing Setup Procedure

To begin setting up the tensile testing machine, the 5N load cell is mounted, and the console on the computer is configured for remote control. It is important to verify the machine's setup, ensuring that the load limit is below the load cell's capacity (4.5N) to prevent damage to the load cell. Once confirmed, assembly of the components can begin. Part 1 is attached to the upper section of the tensile machine using a rivet. The calibration button is pressed to make sure all measurements are accurate, especially to exclude the weight of the attachment. Following this, Part 3 is connected to Part 4 with a screw, and the pot is inserted into Part 4. The soil holder (Part 5) is placed on top of the pot and screwed into Part 4 to secure the soil. The stem is trimmed to the appropriate length to ensure it fits securely within Part 2 without extending through to Part 1. It is then inserted through the small opening at the bottom of Part 2, stopping at the seed for barley or the root starting point for mung beans, and secured with super glue. Enough time is given for the glue to fully dry before proceeding. Figure 4 show a rendering of the pullout test setup, displaying a cross-section of the apparatus with the barley and mung bean seed secured in place for a clearer understanding of its positioning. Once the root is securely attached, Part 3 is connected to the bottom section of the testing machine. Part 1

is then carefully lowered until it can be connected to Part 2, ensuring all components are properly aligned. Throughout the tests, the pre-tension is recorded. The days of growth and stem height, for each seed, are documented beforehand to be able to relate the physical characteristics of the plant to the tensile test results, providing insights into how root development impacts the pullout force. Once the assembly is complete, the machine settings are adjusted to terminate the test at a displacement of 100 mm. This limit is set based on the pot's total depth of 67.5 mm and the root lengths observed in Section 3.1, ensuring that all relevant data is collected before the test ends. The speed of the test is set to 1 mm/s, balancing efficiency with a pace slow enough to avoid damaging the root by pulling it out too quickly. Upon completion of the test, the results are exported, including 1,000 data points along with timestamp information for each point.

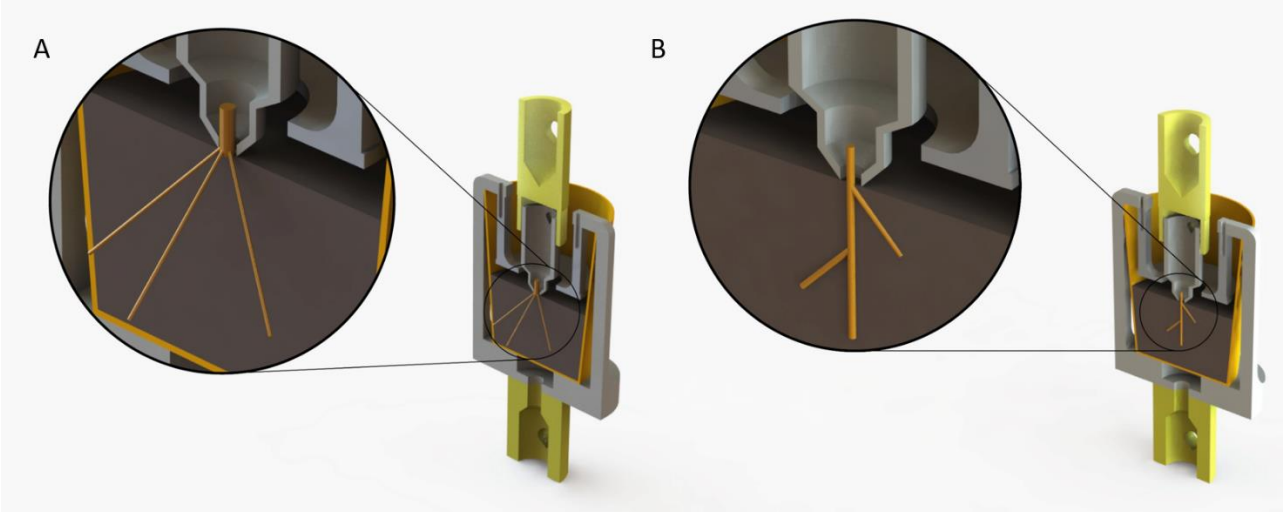

Figure 4: Rendering of the pullout test setup, showing a cross-section of the apparatus with the seed securely positioned for better clarity. A) Barley seed and B) Mung bean seed.

2.3 CT Scanning

2.3.1 Equipment Used and Scanning Parameters

The scanner used to perform the CT scan is the CoreTOM MicroCT. This is a micro-computed tomography scanner designed to characterize the microstructures of a wide variety of materials, but it is especially suited for handling a broad range of geological samples. It combines the typical field of view of a medical CT system with the high-resolution imaging performance capabilities of laboratory micro-CT systems. The technical specifications of Micro-CT system machine can be found in the appendices in Table 18. Table 2 summarizes the scan settings used in the CT scans performed. These settings were refined and adjusted through trial runs to achieve optimal image quality.

Table 2: Optimized Scan Settings for CT scan.

SCAN INFO	VALUES
Tube Voltage	100 kV
Tube Power	20 W
Voxel Size	20 µm
Exposure	185 ms
Projections	2160
Average	2
Time/360°	~ 13 m
Filter	No filter used

Starting with the scan settings, the x-ray tube voltage is set to 100kV. Higher voltages can penetrate denser materials, while lower voltages enhance contrast in softer materials. Since roots and soil are both considered soft materials, a lower voltage setting is more appropriate. The x-ray tube power affects the brightness of the x-ray source, influencing the image quality and the speed of acquisition. This is determined by the x-ray tube voltage and current values. The voxel size determines the resolution of the 3D image. A smaller voxel size provides higher resolution, capturing more detailed information. This is especially important here, as it helps distinguish between soil and roots, which have very similar densities.

The exposure represents the amount of time that each projection (or image capture) is exposed to x-rays during the scan. Longer exposure times can improve image clarity but also increase the radiation dose to the sample. In this case, since the CT scans focused on capturing the 3D root system morphology, a higher exposure was preferred. The total number of individual projection (2D images) captured during one complete rotation of the sample also impacts the quality of the reconstructed 3D image. Here, the choice of 2160 projections was a balance between the time each scan consumed and the quality of the resulting image. Each scan took approximately 15 minutes to complete a full 360-degree rotation, with 13 of those minutes dedicated to acquisition time. The average represents the number of times each projection is averaged during the scanning process to increase image quality by reducing noise. Similar to the number of projections, this was a trade-off between image quality and scan duration. Lastly, no filter was used during the scanning process. Generally, a filter can modify the energy spectrum of the x-ray beam, which can be useful for increasing contrast or reducing the radiation dose.

The parameters in Table 3 represents the positional coordinates used, which are determined once the sample is mounted onto the scanning plate and selected through the computer interface. The COR value specifies the exact position of the center of rotation in the scanner's coordinate system. This is important for accurate 3D reconstructions because it determines the pivot point around which the sample rotates.

Table 3: Optimized positional coordinates of the scan settings.

SCAN SETTING	VALUES
COR	~ 1428.00
VC	~ 1427.42
HV	~ 1428.00
SDD	~ 1007.78
SOD	~ 134.37
Tilt, Skew, Slant	0
Magnification	~ 7.5

The VC represents the vertical center of the field of view. It aligns the sample vertically within the scanner to achieve uniform resolution. The HC, on the other hand, is the horizontal center. It ensures the sample is centered horizontally, affecting both focus and symmetry. The SDD represents the distance from the X-ray source to the detector. A longer distance makes the image sharper but smaller. The SOD is the distance between the X-ray source and the sample being scanned. Shorter SOD results in higher magnification. The magnification is determined by the ratio of the SDD to the SOD. Higher magnification produces larger images of the sample, providing more detail but reducing the field of view [39].

2.3.2 Post-Processing with Dragonfly

Dragonfly is a software platform designed for scientific image processing and analysis, including CT scan data. The software helps extract information about objects and materials, making it a powerful tool for analyzing complex structures like roots in soil or other biological materials. Segmentation is one of the most powerful features in Dragonfly, particularly when dealing with complex structures. Segmentation helps separate specific areas of interest within an image, such as distinguishing roots from the surrounding soil. Dragonfly offers both manual and automated segmentation methods.

When working with raw CT data, it is best to start with manual segmentation to first define and then refine the region of interest (ROI). This process reduces the dataset to a smaller, more relevant subset, focusing on the critical data, such as the roots, while minimizing irrelevant information, like the soil. This process can be done by adjusting intensity ranges to isolate specific features, manually adding or removing parts of the region, and automatically eliminating irrelevant objects based on voxel count. Once the ROI is sufficiently refined, automated segmentation, such as machine learning or deep learning models, can be applied for faster and more accurate results. After the image is properly segmented, the segmented roots can be modeled in 3D and meshed to create a final 3D representation of the roots.

For the automated segmentation process, a deep learning model was chosen over a machine learning model because it works much better with complex and large datasets. Deep learning models can automatically learn high-level features, making them more accurate for tasks like segmenting intricate structures such as roots. The model was trained using Dragonfly's Segmentation Wizard. After over 10 rounds of training, the results were considered satisfactory, as the algorithm reliably identified the main roots structure, although some root segments were missing and some soil was mistakenly included. The specific deep learning model used was U-Net, a type of fully convolutional network (FCN) popular for image segmentation. U-Net is highly effective for fast and precise segmentation of 2D images [40]. The model was configured with a depth level of five, meaning there were five layers in the network. It had an initial filter count of 64, which refers to the number of filters in the first convolutional layer. The input dimension was set to 2D, so the images were processed slice by slice.

2.4 FEM Simulation

2.4.1 Modeling Techniques with Abaqus

The simulations, conducted using the Finite Element Method in Abaqus 2023, utilized root models created in SolidWorks with varying geometries to examine the impact of specific parameters on pullout force. These parameters were identified through a detailed analysis of the 3D structures of barley and mung bean roots, obtained from CT scans, documented in Section 3.3. Analysis of the CT scan data revealed common traits among each root type, as well as characteristics that varied between scans. These variable traits were selected as parameters for the simulations, enabling a systematic assessment of how different root geometries and architecture influence pullout force. The tested root models included six variations for barley seeds and three for mung bean seeds. Soil and hydrogel were used as substrates to compare the interface strength of identical root models across different environments. This approach enables a direct comparison of root-soil and root-hydrogel interfaces, providing insights into how substrate stiffness and material properties influence root anchorage and pullout strength.

Barley root models

Three parameters were chosen to create variations in the barley root models. The first parameter, vertical branching angle, measures the deviation of a seminal root from the vertical axis extending through the seed. The second parameter, radial branching angle, measures the angle between two seminal roots as they emerge from the seed within a horizontal plane [41]. Lastly, root tortuosity, or curvature, describes how much a root deviates from a straight path [42].

Each model is based on precise root dimensions obtained from CT scans, ensuring accurate representation of the root's actual size. The barley root model features a seed modeled as a cylinder with a base diameter of 2 mm and a height of 5 mm. From this seed, six roots extend, each modeled as a cylinder with a diameter of 0.5 mm and a height of 25 mm. Figure 5 shows a sketch of the root structure with the specified dimensions, while Figure 6 presents the renderings of the different barley root models tested.

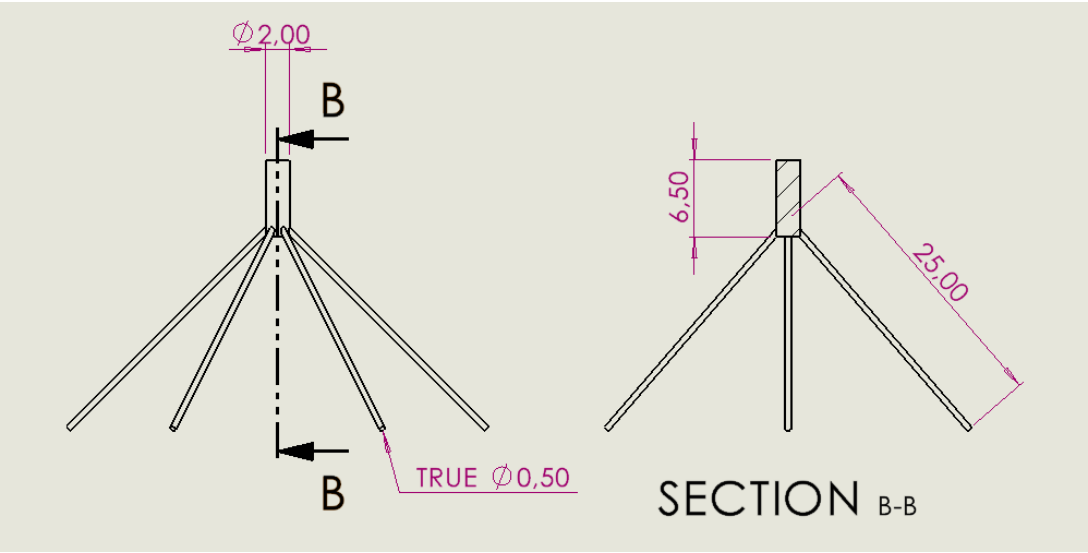

Figure 5: Sketch of the barley root structure with indicated construction dimensions. All measurements are provided in millimeters (mm).

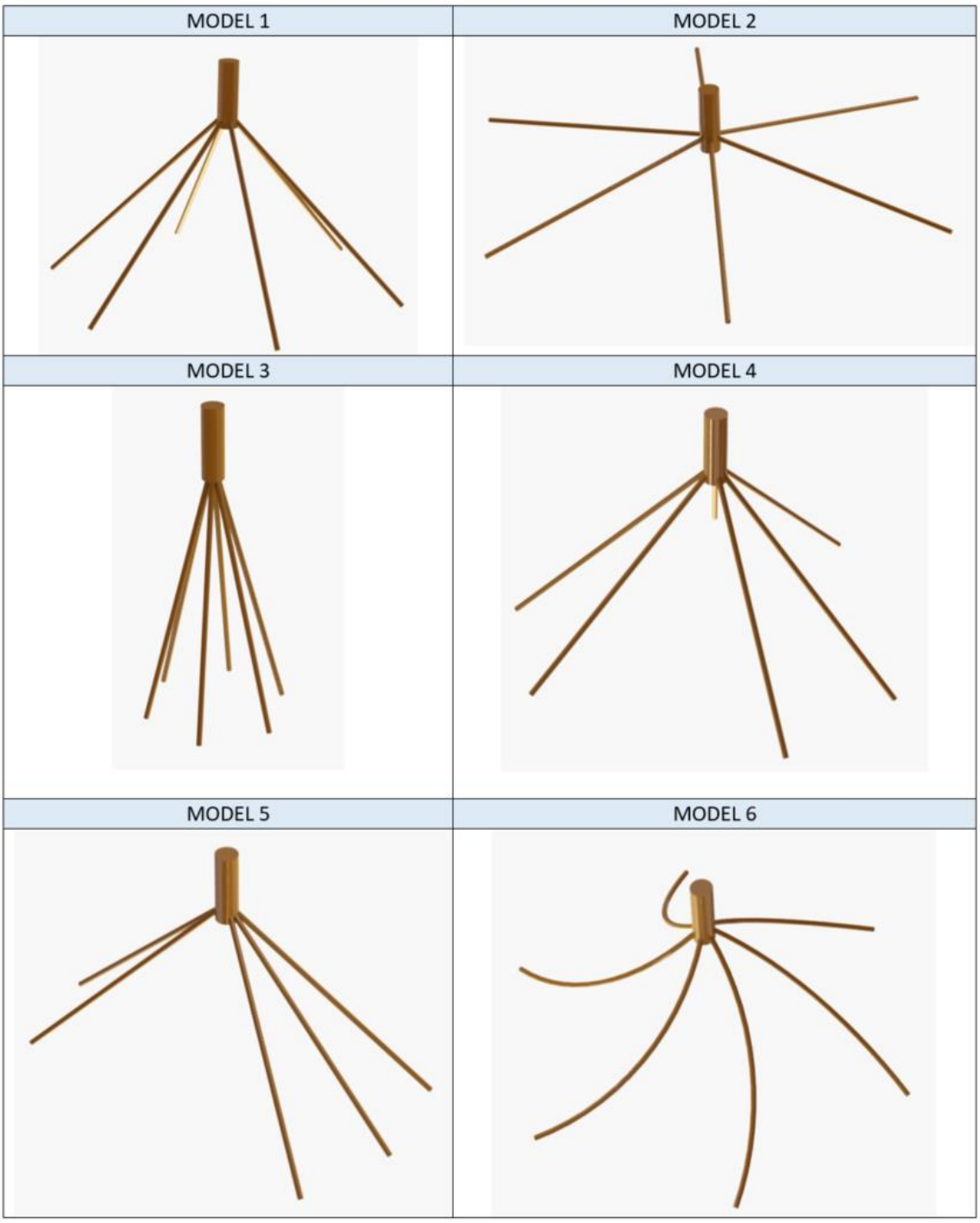

Figure 6: Rendering of 3D barley root models. All parameter variations across the barley root models, including vertical branching angles, radial branching patterns, and root tortuosity, are listed in Table 4.

Table 4 outlines the variations in parameters across the different models, focusing on vertical branching angles, radial branching patterns, and root tortuosity. In the first three models, the only difference is the vertical branching angle, with values of 15°, 45°, and 80°. These angles were chosen to represent three distinct scenarios: almost vertical (15°), diagonal (45°), and almost horizontal (80°), allowing for a comprehensive analysis of how variations in vertical branching affect pull-out force and interface strength. Model 4 and Model 5 have the same vertical branching angle as Model 1, enabling a comparison of how different root arrangements around the central axis affect interface strength. Model 1 is characterized by equidistant roots with 60° spacing, creating a balanced, symmetric configuration. This serves as a useful baseline for comparison, as Models 4 and 5 both feature unequally spaced roots, resulting in an asymmetric

root pattern. In Model 4, the angles alternate between larger (80°) and smaller (40°), creating areas where the roots are more crowded and denser. Model 5 takes this even further, with 30° gaps between some roots forming tight clusters, while the 120° spacing creates a large open area. Lastly, Model 6 can be compared to Model 1 as they have the same vertical and radial branching angles. This comparison allows for evaluating how root tortuosity influences pull-out force, as Model 6 has tortuous roots, whereas Model 1 has straight roots. Tortuosity is a dimensionless coefficient calculated by dividing the actual length of the root path by the straight-line distance between the start and end points. In Model 6, the tortuosity is 1.3, as the actual root length is 25 mm, while the straight-line distance is 24.2 mm. In the appendices, from Figure 44 to Figure 49, all the technical drawings of the models are provided, with all parameters clearly indicated on the drawings for better understanding.

Table 4: Summary of parameter variations across barley root models, including vertical branching angles, radial branching patterns, and root tortuosity.

Variation	Model 1	Model 2	Model 3	Model 4	Model 5	Model 6
Vertical branching angle	45°	80°	15°	45°	45°	45°
Radial branching angle	60°	60°	60°	80° - 40° (x3)	120° - 30° - 30° (x2)	60°
Root tortuosity	0	0	0	0	0	1.3

Mung bean root models

For the mung bean root model, the selected parameter is the number of lateral roots per branching point. Like the barley models, the mung bean models are based on exact root dimensions obtained from CT scans. The mung bean model features a primary taproot, modeled as a cylinder with a diameter of 1mm and a height of 25 mm. From this, lateral branches extend, each modeled as a cylinder with a diameter of 0.7 mm and a height of 10 mm. Figure 7 shows a sketch of the root structure with the specified dimensions, while Figure 8 presents the renderings of the different mung bean root models tested. The differences between the models are clearly illustrated in Figure 8: Model 1 has no lateral roots, Model 2 has one lateral root per branching point, and Model 3 has three lateral roots per branching point. For further details on the dimensions of the models, the technical drawings can be found in the appendices, Figure 50 and Figure 51.

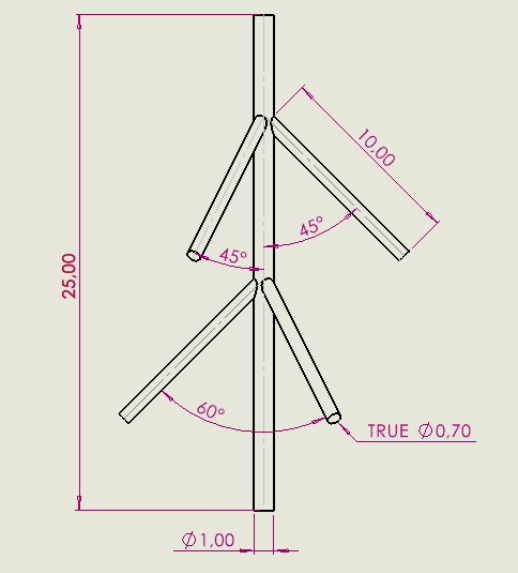

Figure 7: Sketch of the mung bean root structure with indicated construction dimensions. All measurements are provided in millimeters (mm).

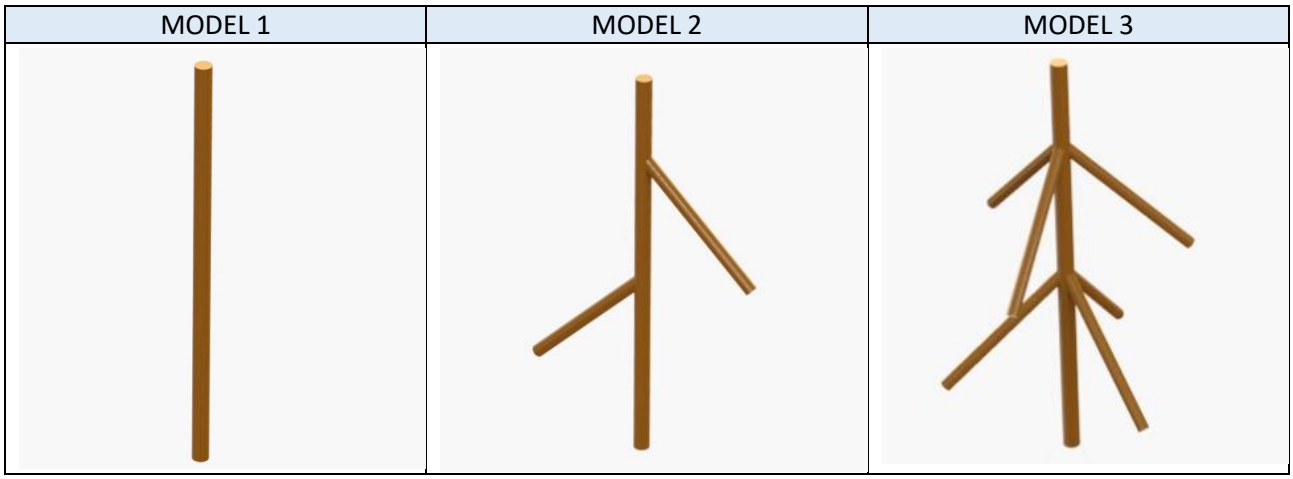

Figure 8: Rendering of 3D mung bean root models. The models differ as follows: Model 1 has no lateral roots, Model 2 includes one lateral root per branching point, and Model 3 features three lateral roots per branching point.

Substrate

The dimensions and geometry of the substrate, for both soil and hydrogel, were chosen based on real data, specifically the size of the soil used in the pullout laboratory experiments. The soil naturally conformed to the shape of the pot it was placed in. As a result, the substrate is modeled as a truncated cone with a top radius of 27 mm, a bottom radius of 24 mm, and a height of 33 mm, also shown in Figure 9 and explained in more detail in Figure 52 in the appendices. The root space within the substrate was created automatically in SolidWorks by subtracting the root geometry, generating a void to represent where the roots would be positioned.

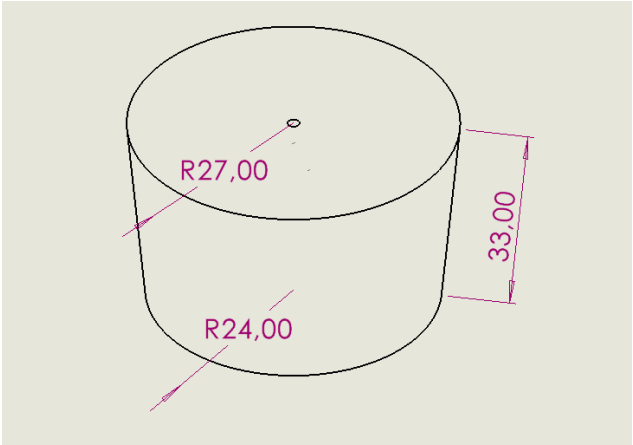

Figure 9: Sketch of the medium structure with indicated construction dimensions. All measurements are provided in millimeters (mm).

2.4.2 Simulation Parameters

Material property

The roots are modeled as an elastic linear material with a plastic threshold modeled by a von Mises yield criterion. In the early stages of deformation, before yielding, the root material can be approximated as linearly elastic, meaning that stress is proportional to strain, following Hooke's Law. Once they reach a certain level of deformation, they will start deforming plastically [15, 43, 44]. The von Mises yield criterion is used in engineering to describe the start of plastic deformation in ductile materials. It predicts when the material will yield based on the stress state. The density and mechanical characteristics of roots, listed in Table 5, were taken from literature, where they were determined by performing tensile tests on 12 root samples [43].

The soil was modeled as an elastic perfectly plastic material, with the plastic behavior of soil failure defined by the Mohr–Coulomb model. The elastic characteristics of the soil are assumed to be linear and isotropic, following Young's modulus and Poisson's ratio. Similar to the roots, the soil can deform under stress and return to its original shape once the load is removed, up to a certain limit [15, 43-45]. The Mohr-Coulomb failure criterion predicts when soil will fail along a shear plane based on three factors: effective cohesion, friction angle, and normal stress. Failure occurs when the shear stress, the force trying to cause sliding, on a specific plane within the soil becomes greater than the soil's ability to resist it. Essentially, once this stress surpasses a critical limit, the soil can no longer hold together on that plane, leading to sliding or shearing along that surface. Cohesion represents the soil's internal bonding strength, which comes from electrostatic forces and particle interlocking. The friction angle describes the soil's resistance to sliding along internal surfaces [46]. The density and mechanical characteristics of soil, listed in Table 5, were taken from literature, where they were identified by direct shear test and tri-axial test on 6 soil sample [43].

Hydrogel was modeled as a hyper elastic material using the Ogden strain energy potential [47-49]. The Ogden material model is a hyperplastic model used to describe the nonlinear stress–strain behavior of complex materials such as rubbers, polymers, and biological tissues. It expresses the strain energy as a function of the material's principal stretches and includes parameters that control the material's stiffness and nonlinearity. One parameter is the shear modulus, which represents the material's stiffness in response to shear deformations. Another is a dimensionless parameter that characterizes the material's nonlinearity, governing how the stress-strain relationship deviates from linearity [50]. Additionally, there is a compressibility parameter, but for the hydrogel, it is considered to be zero since the material is modeled as incompressible, meaning it does not significantly change volume under stress. The mechanical characteristics of hydrogel, listed in Table 5, were taken from literature [51].

Table 5: Material property used in FEM simulation to describe the behavior of roots [43], soil [43], and hydrogel [51].

Property	**Root**
Young's Modulus (E)	1500 MPa
Poisson's Ratio (υ)	0.3
Modulus of Rupture (MOR)	14 MPa
Density (ɣ)	5.4E-06 N/mm^3
Property	**Soil**
Young's Modulus (E)	24 MPa
Poisson's Ratio (υ)	0.34
Cohesion (c)	0.02
Density (ɣ)	2.03E-05 N/mm^3
Internal angle of friction (ϕ)	28°
Property	**Hydrogel**
Shear Modulus (μ)	0.045 MPa
Dimensionless parameter (α)	3.6128124
Compressibility parameter (D)	0
Number of terms (N)	1

Mesh design and element types

Linear tetrahedral elements, C3D4, are preferred for modeling complex geometries that require detailed attention around curved surfaces and intricate structures. This element type is especially suited for organic or irregular shapes, like roots, due to their ability to adapt seamlessly to complex 3D geometries. For the roots, a finer mesh size of 0.19 mm is used to improve resolution and accuracy at critical interaction points with the substrate. For the substrate itself, the mesh size begins at 0.19 mm at the contact point with the roots and incrementally increases to 2 mm towards the outer regions. This graduated mesh sizing allows for

detailed stress and deformation analysis close to the roots while reducing computational demands in less critical areas farther away from the roots. This approach is a compromise between maintaining result accuracy and managing computational resources. Figure 10a and Figure 10b show the mesh for the medium and the root, respectively. Figure 10c and Figure 10d provide zoomed-in views of the root mesh for a clearer visualization of the details.

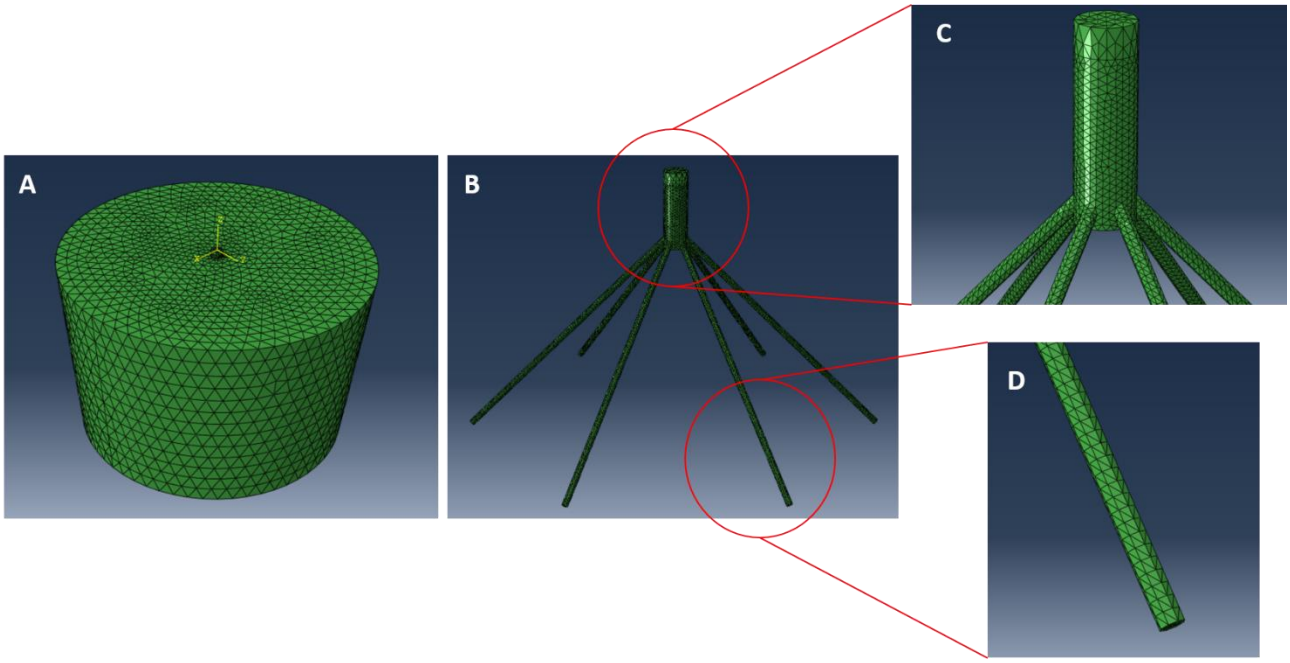

Figure 10: Mesh visualization of the medium and root models. (a) Mesh of the medium, (b) Mesh of the root, (c) and (d) Zoomed-in views of the root mesh to highlight finer details.

When meshing different models with the same initial mesh size settings, the total number of nodes and elements can still vary between models. This variation occurs because, although the mesh size is the same, the actual 3D surfaces and volumes of the models are different. Each model's unique geometry dictates how the mesh conforms to its contours, edges, and features. The final meshing parameters, including the number of nodes and elements as well as the surface area for each model, are presented in Table 6 for the barley roots model and in Table 7 for the mung bean roots model.

Table 6: Meshing parameter for barley root models

BARLEY MODEL	Model 1	Model 2	Model 3	Model 4	Model 5	Model 6	Mean	Range
Surface area (mm^2)	227.157	227.989	225.014	254.072	208.440	257.645	233.39	49.205
Number of nodes	27209	25611	25546	27460	27342	24656	26304	2804
Number of elements	121161	111380	112302	122264	121782	108250	116190	14014

Table 7: Meshing parameter for mung bean root models

MUNG BEAN MODEL	Model 1	Model 2	Model 3	Mean	Range
Surface area (mm^2)	78.400	126.299	201.784	135.49	123.384
Number of nodes	7563	9928	15749	11080	8186
Number of elements	30609	40807	65830	45749	35221

The mean calculated across all models for each meshing parameter showed approximately double the quantity in barley models compared to mung bean models. This higher number of nodes and elements in barley models is due to their larger average surface area. The range, which refers to the difference between the maximum and minimum values in the dataset for each parameter, shows that mung bean models exhibit much greater variability in terms of nodes, elements, and surface area. This indicates that mung bean models show greater variability in their geometry and mesh properties, due to more evident differences within the individual models themselves.

Interaction properties and boundary conditions

The interaction between the root and the medium was modeled by specifying both tangential and normal contact properties. A friction coefficient of 0.4, based on literature [43, 44], was used to model the tangential friction, representing the resistance to sliding between the root surface and the surrounding substrate, whether soil or hydrogel. Friction directly impacts the forces transmitted through the interface, and including it in the simulation helps to accurately represent how the root resists movement when subjected to external forces, such as in pull-out tests. The normal contact was modeled as hard contact, meaning that the root and the medium can push against each other but cannot penetrate one another. This setup simulates the real physical behavior where roots compress the soil or hydrogel as they attempt to move through it, with the substrate responding by resisting the motion. In general contact modeling, the root is assigned as the master surface and the soil as the slave. The master surface typically has a finer mesh and greater deformation, while the slave surface responds to the interaction. This setup allows to accurately represent stress transmission and deformation at the root-substrate interface.

The boundary conditions are set by pinning the edges of the external sides of the medium, so that they cannot move. This simulates the effect of real-life constraints in the laboratory, where the medium is confined by a container, such as a pot. Lastly, a reference point is set on the horizontal upper surface of the seed in the barley models, or on the primary roots in the mung bean models. By using this point, forces and displacements can be more easily applied and measured during the simulation. Figure 11 illustrates the boundary conditions applied to the substrate as well as reference point defined.

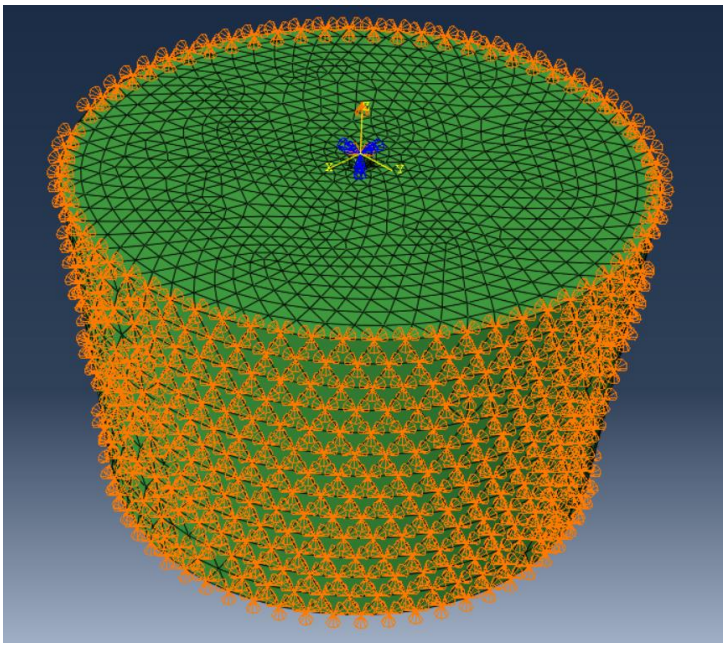

Figure 11: Boundary conditions for the FEM simulation, showing pinned edges on the external sides of the medium and the reference point defined on the horizontal upper surface of the root model.

Loading conditions

The simulations were conducted by applying a vertical displacement of up to 4 mm to the reference point, as this was sufficient to reach the maximum pullout force in most cases. If a simulation did not reach the maximum force at 4 mm, it was rerun with a displacement limit of 8 mm to ensure capture of the peak force. The root was displaced at a constant velocity of 1 mm/s, matching the conditions used in the laboratory setting.

Abaqus solver and step definition

The solver used for the simulation was chosen based on a trial-and-error approach. Initially, the analysis was attempted using the static analysis solver, but the simulation failed to run because it could not solve the equations. This failure occurred because the scenario involves time-dependent behavior and is not a static situation. Next, the dynamic solver was used, which can be implicit or explicit. Typically, the implicit solver provides accurate results when solving quasi-static problems. A quasi-static problem occurs when the process is so slow that the effects of inertia are negligible compared to the applied forces. Pulling a root out of soil at a constant, slow speed, as in this simulation, can be considered a quasi-static process. The pull is slow enough that the effects of can be ignored. However, when the simulation was run using the dynamic implicit solver, it failed. This failure was likely due to poor convergence of the contact algorithm, which struggled to handle the complex contact interactions and significant nonlinearities present in the root-soil interface. In contrast, the dynamic explicit solver successfully completed the simulation. This solver is well-suited for handling highly nonlinear problems, large deformations, and complex contact interactions, even though it requires significantly more computational time compared to the implicit solver. The primary advantage of the explicit solver is that the simulation will always converge. This is because the explicit solver relies on small time steps and does not require repeatedly checking for equilibrium to proceed [52].

2.4.3 Energy Analysis and Convergence Assessment

Energy history output

To assess the stability and realism of simulation results in explicit analyses of quasi-static problems, energy history outputs are important. Comparing various energy components helps determine whether the analysis provides an appropriate response and accurately reflects the behavior of the simulated system [53]. The energy output of interest includes the following.

Internal energy (ALLIE) evaluate the energy absorbed by the substrate and the root. A consistent increase in internal energy as displacement or time progresses can indicate realistic energy absorption in the materials, validating their deformation and interaction properties. Kinetic energy (ALLKE) measures the energy due to motion in the system. For a quasi-static process, this should be minimal. If kinetic energy exceeds 1-5% of the internal energy (ALLIE), it suggests that inertia effects are present. Artificial strain energy (ALLAE) represents unusual or unrealistic deformations, typically arising from numerical artifacts within the finite element model. This energy should remain as low as possible, ideally less than 5% of total internal energy. External work (ALLWK) represents the work done by the external forces applied during the pullout. Monitoring this component helps ensure that the force-displacement relationship aligns with the expected material behavior at the root-soil and root-hydrogel interfaces. A consistent increase in ALLWK with displacement indicates proper energy input into the system. Lastly, the total energy (ETOTAL) in the system represents the sum of all energy components and ideally should remain constant, indicating that the energy inputs and dissipations are well-balanced. However, in practice, ETOTAL is only approximately constant. This slight variation occurs because the method for calculating recoverable strain energy uses a modified trapezoidal rule. This rule is preferred over an exact calculation to improve computational speed, which results in minor variations in the energy balance [52-54].

Mesh Convergence Test

In finite element modeling, the quality of the mesh is important for achieving accurate results. A coarse mesh can lead to errors, while a finer mesh improves the convergence of the numerical solution but increases simulation time [55]. To balance accuracy and efficiency, a mesh convergence study is performed to determine whether the chosen mesh provides satisfactory results without unnecessary computational expense.

The mesh convergence test was conducted on a single model, Barley Model 1 in soil, which was randomly selected. To evaluate different mesh densities, five configurations were tested, with progressively finer meshes in the root model and at the root-substrate contact. Table 8 summarizes the configurations used for the convergence test, detailing the number of elements in the root model and the mesh sizes for both the root model and the substrate.

Table 8: Mesh configurations used for the convergence test, detailing the number of elements and mesh sizes for the root model and substrate.

Test number	Number of element (root model)	Mesh size root model [mm]	Mesh size substrate (at the contact point with roots) [mm]	Mesh size substrate (outer region) [mm]
1	49276	0.35	0.35	2
2	121161	0.19	0.19	2
3	228423	0.13	0.13	2
4	394819	0.097	0.097	2
5	601398	0.078	0.078	2

2.5 Hydrogel Protocol, Preparation and Planting

Three different protocols were tested before arriving at the final version, which is described in detail in Section 2.5.2. These trials were conducted to address an issue with persistent fungal and bacterial growth in the hydrogel samples. The main differences between protocols involved sterilization methods, which proved essential for preventing fungal contamination. The third protocol was ultimately successful in eliminating fungal and bacterial growth. While there are additional, minor differences between the protocols, these are not detailed here. A full comparison of all three protocols can be found in Table 20 in the appendices.

2.5.1 Hydrogel Materials

The hydrogel is composed of a polymer and a crosslinking agent, where sodium alginate serves as the polymer and calcium is used as the crosslinking agent. The NPK fertilizer is added to provide essential nutrients that support seed germination and growth, ensuring the hydrogel serves not only as a physical matrix but also as a nutrient-rich environment. Antifungal agent is included to prevent fungal growth. List of substances, suppliers, and product information for the hydrogel preparation can be found in the appendices in Table 19.

Polymer

Sodium alginate, a natural polymer, is commonly used in tissue engineering, 3D cell culture, and other applications due to its biocompatibility and non-toxic nature. As a linear polysaccharide with negatively charged carboxyl groups, sodium alginate provides an environment where plants can absorb water and nutrients without exposure to harmful substances that could inhibit growth [56]. When sodium alginate encounters divalent cations, like calcium, it forms a gel. The calcium ions create cross-links between the alginate chains, stabilizing them into a three-dimensional network. This gel structure is porous, hydrated, and stable, resembling natural conditions for plant roots or biological tissues [57]. The porous nature of the gel supports efficient gas and nutrient exchange as well as water retention, making it an ideal medium for plant growth [58]. Furthermore, the gel's porosity and mechanical properties can be adjusted by modifying the concentration of alginate or cross-linking agents [59].

Crosslinking agent

When forming hydrogels with sodium alginate, various divalent cations can be used as crosslinking agent. However, some, like beryllium (Be^{2+}) and barium (Ba^{2+}), have toxicity concerns, and others, like radium (Ra^{2+}), are radioactive. Among the safer options, calcium (Ca^{2+}), magnesium (Mg^{2+}), and strontium (Sr^{2+}) are viable choices. Calcium has been found to be the most effective for promoting gelation. Its ionic size is large enough to coordinate with the carboxyl and hydroxyl groups of alginate chains, forming strong and stable gels. Strontium can also form gels but creates weaker crosslinks due to its lower surface charge density. Magnesium, on the other hand, is too small to effectively crosslink the alginate. Calcium's charge density allows it to form strong physical crosslinks, resulting in mechanically robust hydrogels. Furthermore, its biocompatibility and non-toxic nature make it the ideal choice for sodium alginate hydrogels used in plant growth and tissue engineering [60].

The preparation of the hydrogel involved the testing of three calcium compounds: calcium chloride, calcium sulfate, and calcium carbonate, each influencing gelation speed differently. Calcium chloride ($CaCl_2$) resulted in rapid gelation, but this speed was too fast for larger volumes (up to 40 ml), leading to uneven cross-linking. Calcium sulfate ($CaSO_4$) provided a more moderate gelation, even though still too rapid for optimal results. In contrast, calcium carbonate ($CaCO_3$) released calcium ions slowly, producing uniform gels with strong mechanical properties due to gradual and even cross-linking [61, 62]. Glucono delta-lactone (GDL) is used with calcium carbonate ($CaCO_3$) in the preparation of sodium alginate hydrogels because it ensures a controlled release of calcium ions (Ca^{2+}). GDL gradually lowers the pH of the solution, creating an acidic environment. This acidity causes calcium carbonate, which is otherwise insoluble at neutral pH, to dissolve and slowly release calcium ions, allowing for a more controlled and gradual gelation process [63].

NPK fertilizer

NPK stands for Nitrogen (N), Phosphorus (P), and Potassium (K), which are the three primary nutrients necessary for various physiological and biochemical processes in plants. Nitrogen is important for leaf growth and chlorophyll production, phosphorus supports the development of roots, flowers, seeds, while potassium significantly helps in water absorption, enzyme activation, and photosynthesis. When plants are grown in non-soil substrate such as hydrogel, these natural nutrients, typically found in soil, are absent and must be supplied externally to ensure plant growth [64]. For this project, the NPK 20-20-20 was chosen because it is a balanced fertilizer, providing equal proportions of Nitrogen, Phosphorus, and Potassium.

Antifungal

In non-soil, nutrient-rich environments like hydrogels, fungal and bacterial growth can occur rapidly due to the availability of moisture, warmth, and nutrients. Fungi and bacteria thrive in these conditions so preventing this growth provide a healthier substrate for plant development. Sodium alginate, in particular, supports fungal growth due to its excellent water retention capabilities, creating a moist environment that promotes spore germination and metabolic activity [65]. Furthermore, airborne particles often carry microorganisms, including bacterial and fungal spores, which can easily settle on the hydrogel surface, quickly colonizing it. Without proper filtration or sterilization, air contamination becomes a significant source of unwanted microbes [66]. Additionally, warm environments create ideal conditions for microbial growth. Most fungi and bacteria thrive in temperatures between 20°C and 30°C, which overlaps with the optimal temperature range for plant growth. Warmth accelerates their metabolism and reproduction, leading to rapid colonization of the hydrogel [67]. Another major contributor to bacterial and fungal growth is the seed itself. Seeds naturally carry various microorganisms on their surface and, in some cases, internally. These microorganisms can include fungi and bacteria, and when seeds are planted in a hydrogel, they can introduce these microbes into an otherwise sterile environment [68]. Antifungal agents help prevent or contain the growth of harmful microorganisms by disrupting their cellular processes. These agents damage cell walls or interfere with metabolic activity, stopping microbial growth and germination [69]. This is particularly important in hydrogel environments to maintain sterility and ensure that plants can grow without microbial interference.

2.5.2 Hydrogel Preparation and Dosage

A 1-10% (w/v, g/mL) alginate solution is typically prepared by thoroughly mixing sodium alginate powder with distilled water. This process takes place in a fume hood using sterilized equipment to avoid contamination. Before being added, sodium alginate and NPK (nitrogen (N), phosphorus (P), and potassium (K)) powdered fertilizer are sterilized under UV light for 20 minutes to eliminate surface contaminants. UV sterilization works by disrupting the genetic material of microorganisms on the surface of the powders. After the UV treatment, the powders are stored in sealed containers in the fume hood to maintain sterility until the next use. An antifungal agent is also added to the mix. Both the antifungal agent and the NPK fertilizer are incorporated in the recommended doses provided on their packaging instructions. If a range is specified, the maximum amount is used to ensure optimal nutrient availability and effective prevention of fungal growth. To ensure complete dissolution and homogeneity, the solution is manually mixed, stirred for several hours with a magnetic stirrer, and then refrigerated overnight.

Following the formation of the viscous alginate liquid, calcium ions are introduced for crosslinking purposes. Two separate suspensions are prepared in distilled water: one with finely powdered $CaCO_3$ and the other with finely powdered GDL. Each of these components is UV-sterilized beforehand to prevent contamination, and all equipment used is also sterilized. The calcium and GDL solutions are then manually mixed into the alginate solution using a sterile spatula, within a fume hood to maintain sterility. The millimolar concentrations of the calcium component used in hydrogel preparation can range from 25 mM to 150 mM. These concentrations were determined through laboratory experiments. Concentrations below 25 mM result

in insufficient cross-linking, making the hydrogel too weak to properly support seed placement. In contrast, concentrations above 150 mM lead to excessive cross-linking, creating a hydrogel that is too rigid for roots to penetrate. This range provides the optimal balance, allowing for adequate seed placement and enabling root growth within the gel. This variance allows for the adjustment of the hydrogel's mechanical properties to meet specific requirements. For GDL, the molar ratio relative to Calcium Carbonate ($CaCO_3$) is approximately 0.5:1, which indicates that for every mole of $CaCO_3$, half a mole of GDL is used. Slowly add the calcium suspension to the alginate solution while stirring vigorously. Gradually introduce the GDL solution to control the pH and the release rate of calcium ions for crosslinking. As the pH adjusts from the GDL, calcium ions from $CaCO_3$ bind the alginate polymer chains, transforming the viscous liquid into a structured hydrogel. Maintain a sterile environment throughout the process to prevent contamination of the hydrogel. A more schematic, step-by-step representation of the procedure, including the contamination risks at each step and the corresponding solutions to mitigate these risks, can be found in the appendices in Table 21.

2.5.3 Planting Procedure and Environmental Controls

The seed planting process begins by placing the seeds in water in a sealed container to accelerate germination, with a maximum soaking time of 24 hours. After soaking, the seeds are sterilized to eliminate potential contaminants using one of two methods. The first method involves immersing the seeds in a 10% bleach solution, prepared by mixing 1 part bleach with 10 parts distilled water, for 5 to 10 minutes. After this, the seeds must be rinsed thoroughly with distilled water several times to remove any bleach residue, which could be harmful to the seeds. Bleach effectively kills bacteria, fungi, and spores by denaturing their proteins and disrupting their cell membranes [70]. The second method uses a 70% ethanol solution, in which the seeds are soaked for 30 seconds to 1 minute. In this case, the seeds must also be rinsed thoroughly with distilled water after soaking to remove ethanol residues. Ethanol works by dissolving cell membranes and denaturing proteins, effectively sterilizing the seed surface.

Once sterilized, the seeds are handled with sterilized tweezers to maintain a contamination-free environment. Each seed is then carefully placed into the prepared hydrogel sample, which should be viscous and cross-linked enough to support the seed without allowing it to sink to the bottom of the beaker. After planting, the beaker containing the hydrogel and seeds are transferred to the greenhouse. To prevent contamination, the greenhouse must be sealed, and any openings should be covered with HEPA filters. These filters ensure clean, purified air and prevent airborne contaminants from entering and settling on the hydrogel or seeds. A more schematic, step-by-step representation of the procedure can be found in the appendices in Table 22.

3. Results

3.1 Results from Growth Measurement and Root Observation

Barley and mung bean seeds were planted, and the relationship between stem height and days of growth was analyzed by recording stem height measurements at specific time points. Table 9 presents a detailed summary of all the collected measurements.

Table 9: Stem height measurements for barley plants recorded at four specific time points: 3, 5, 6, and 12 days of growth

BARLEY SEED		
Day of growth at the time of stem length measurement	Number of samples per time point	Stem height measurements [mm]
3	3	17.9, 23.1, 23.8
5	7	25.4, 27.6, 27.9, 29.1, 30.3, 30.5, 30.9
6	5	30.8, 50.1, 60.6, 59.7, 64.4
12	3	65.2, 75.2, 77.7
MUNG BEAN SEED		
Day of growth at the time of stem length measurement	Number of samples per time point	Stem height measurements [mm]
5	3	32.5, 39.7, 40.1
7	3	119.8, 121.5, 123.8
15	2	145.2, 156.1

In Figure 12, the graphs on the left show stem height versus days of growth, offering a clearer visual representation of the growth trend. The plots in the top row of the figure represent barley results, while the bottom row shows mung bean data. Different shades of the same color are used to distinguish samples measured on the same day. For barley, day 3 samples are shown in shades of yellow-orange, day 5 samples in shades of red, day 6 samples in shades of pink, and day 12 samples in shades of purple. For mung bean, day 5 samples are displayed in shades of green, day 7 in turquoise, and day 15 in dark blue.

The graphs on the right side of the Figure 12 show the post-processed data using a logistic curve-fitting technique, which is commonly applied to data with an S-shaped trend. Equation 1 defines this model, where L represents the carrying capacity (the maximum value of the curve), k is the logistic growth rate (indicating the steepness of the curve), and x_0 is the function's midpoint [71].

$$y = \frac{L}{1+e^{-k(x-xo)}} \quad (1)$$

The coefficient of determination (R^2), a statistical measure indicating how well a regression model fits the data, was also calculated. R^2 values range from 0 to 1, where an R^2 of 1 indicates a perfect fit to the data, while an R^2 of 0 means the model does not explain any of the data's variability [72]. In this analysis, the R^2 was 0.781 for barley and 0.994 for mung bean.

Table 10 summarizes the coefficients of the logistic fit model for both barley and mung bean seeds. The carrying capacity L, which represents the maximum achievable stem height according to the model, is higher for mung bean (150.74 mm) than for barley (77.62 mm), suggesting that mung beans can achieve greater stem height. The growth rate k is also higher for mung bean (1.27 1/days) compared to barley (0.64 1/days), indicating that mung beans grow more rapidly than barley. The function's midpoint x_0, which is the time at which growth reaches half of its carrying capacity, is slightly later for mung bean (5.87 days) than for barley (5.08 days), reflecting a similar but slightly slower timeline in reaching half of the maximum height. These differences highlight the distinct growth dynamics between the two plant types.

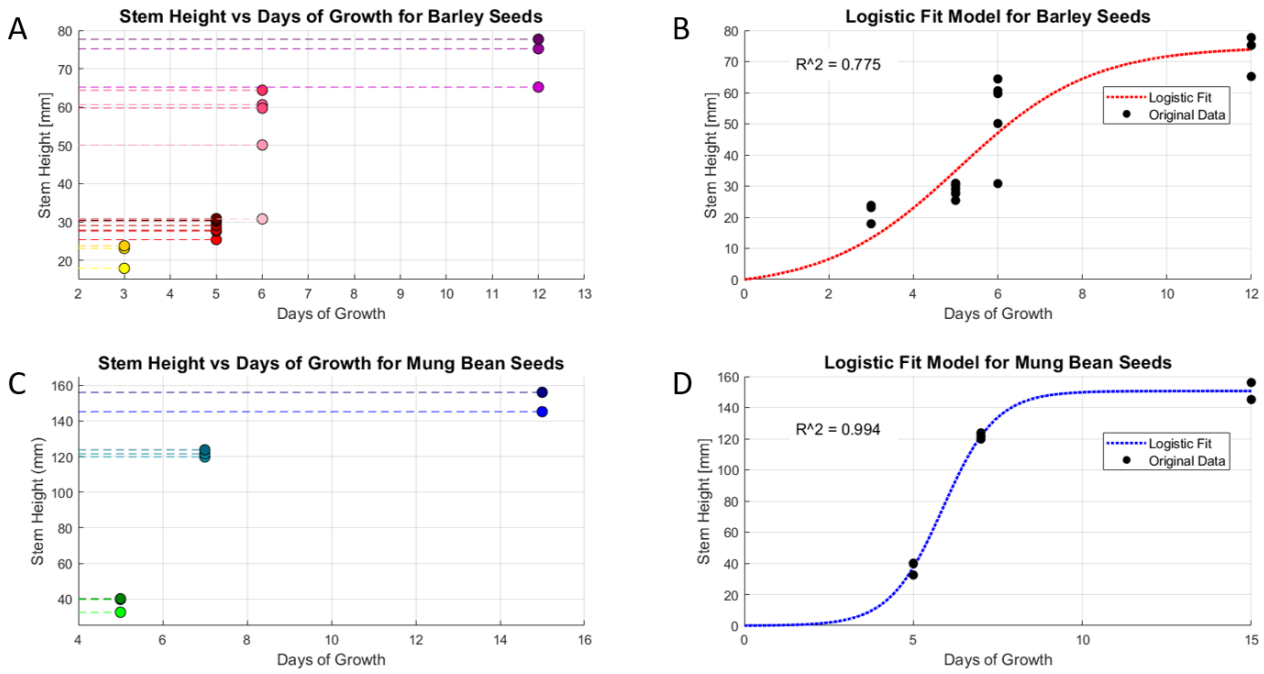

Figure 12: The left-hand graphs (a and c) display stem height versus days of growth, with sample points color-coded according to the day of measurement. The right-hand graphs (b and d) illustrate the results of the logistic curve-fitting model applied to the data. The top row (a and b) corresponds to barley seeds, while the bottom row (c and d) represents mung bean seeds.

Table 10: Logistic fit model coefficients for stem height growth in barley and mung bean, showing carrying capacity (L), growth rate (k), and midpoint (x_0).

Logistic Fit Model Coefficients	Unit of Measure	Barley	Mung Bean
Carrying capacity (L)	mm	77.62	150.74
Growth rate (k)	1/days	0.64	1.27
Function's midpoint (x_0)	days	5.08	5.87

After measuring stem height, three samples from each seed type, barley and mung bean, were carefully removed from the soil and cleaned to visually observe root development over time. In Figure 13a, images of barley plants in their pots at 3, 6, and 12 days of growth are shown. Meanwhile, Figure 13b, c, and d display the cleaned barley roots, with approximate root lengths indicated. The first noticeable observation is the relationship between stem growth and root development. While the precise extent of this relationship is not quantified, it is clear that both stem and root growth occur simultaneously. Upon closer examination of Figure 13b, it's clear that after 3 days of growth, the barley developed its seminal roots, but no adventitious roots are visible. The seminal roots have an approximate length of 80 mm, with slight variation, and maintain a constant diameter of about 0.5 mm along their length. At 6 days of growth, the seminal roots show significant elongation, with an average length of 140 mm. Adventitious roots are now visible, with a diameter of around 0.1 mm. The seminal roots show tapering, starting at 0.5 mm in diameter at the base and gradually reducing to 0.1–0.2 mm toward the tips. After 12 days, the most noticeable difference compared to the 6-day stage is that two seminal roots have elongated further, reaching lengths of 200 mm and 290 mm. All the roots exhibit a certain degree of tortuosity. For days 6 and 12, most branching points have a single adventitious root growing from them. The number of branching points along the seminal roots varies and is not distributed uniformly.

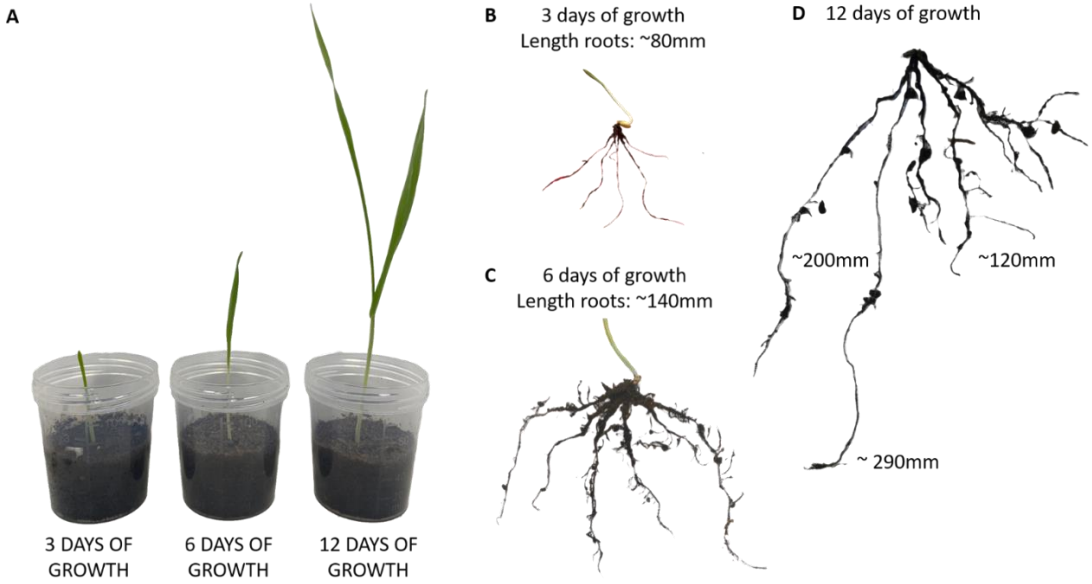

Figure 13: Picture of barley plant and extracted roots after respectively 3, 6, and 12 days of growth.

Mung bean roots, shown in Figure 14, were extracted after 5 and 15 days of growth. The most noticeable difference is that after 5 days, only the taproot had developed in the two samples extracted. In Figure 14a, the primary root measures approximately 40 mm, while in Figure 14b, it is around 42 mm. No secondary branches are present, but the taproot is tortuous and tapered, with a diameter starting at 0.7 mm at the base, narrowing to 0.1 mm at the tip. By 15 days of growth, as shown in Figure 14c, the roots exhibit significant growth. The taproot has slightly increased in length, reaching 78 mm, and its diameter has expanded to 1.2 mm. Numerous secondary branches are now present, with an average diameter of 0.2 mm. It appears that for each branching point, a lateral root has formed, although the lengths of these secondary branches vary considerably.

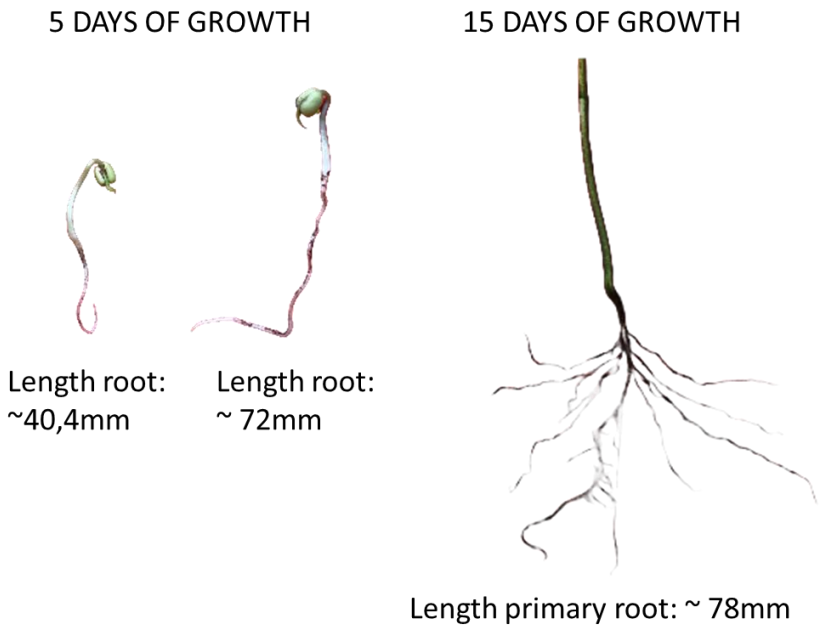

Figure 14: Picture of mung bean extracted roots after respectively 5 and 15 days of growth.

3.2 Results from Pull-out Test

The experimental results from the barley seed pull-out tests are presented in Table 11. A total of 11 tests were conducted, each on a different seed with varying stem heights, measured immediately before testing. The pullout testing machine recorded displacement and corresponding maximum force for each test. During data post-processing, the displacement at maximum force and the work done at maximum force were calculated.

Figure 15a shows the plot of maximum force versus stem height, along with a linear fitting curve and the coefficient of determination (R^2). The linear trend suggests a positive correlation, indicating that taller stems may experience greater maximum force during the pull-out tests. However, the data points show considerable variability around the trend line, as indicated by a low R^2 value of 0.185. This suggests that stem height alone is not a strong predictor of maximum force. Figure 15b presents the plot of work done until maximum force versus stem height, again with a linear fitting curve and the R^2 value. This plot shows a more defined positive trend compared to the maximum force versus height plot, with a higher R^2 value of 0.238. While the trend is more pronounced, significant variability still exists, indicating that other factors also influence the work required to reach maximum force.

Figure 16a displays force versus displacement curves for all barley tests, offering a broad view of the force-displacement relationships. Each curve corresponds to a specific test and stem height. The curves vary in peak force, initial slope (stiffness), and post-peak behavior, which likely reflect different failure or yielding mechanisms of the root-soil system. In Figure 16b, a subset of tests highlights differences in force-displacement behavior, particularly in failure mechanisms. Tests B3 and B11 demonstrate a sharp rise in force with displacement until reaching a maximum force, followed by an immediate drop to zero. This rapid decline suggests a sudden failure. On the other hand, in tests B5 and B10, the force initially increases linearly with displacement, peaks, and then drops slightly before rising again, showing multiple fluctuations throughout the test. This behavior suggests a progressive or gradual failure mechanism, with partial failures and yield points in the root structure before complete detachment. Additionally, a photograph of the intact roots remaining after the pullout test is included for sample B5, B10 and B11. For sample B1, the breakage occurred specifically at the stem-root connection. In contrast, the other two samples retained portions of the root after extraction, although the roots fractured at different lengths along their structure. These observations underline the complex nature of the root-soil interface and the variability in failure behavior based on stem height and root morphology.

Table 11: Data obtained from barley pull-out test results.

	Test denomination	Stem length [mm]	Maximum Force [N]	Displacement at the Max Force [mm]	Work until the Max Force [N*mm]
Test 1	B1	17.9	1.10	2.60	1.89
Test 2	B2	23.1	2.12	14.04	17.68
Test 3	B3	23.8	1.64	6.07	7.28
Test 4	B4	30.8	3.11	9.28	16.04
Test 5	B5	50.1	1.38	14.16	10.24
Test 6	B6	59.7	1.50	2.51	2.55
Test 7	B7	60.6	2.53	5.55	9.19
Test 8	B8	64.4	2.60	14.82	28.25
Test 9	B9	65.2	2.56	6.34	9.81
Test 10	B10	75.2	2.00	28.27	34.28
Test 11	B11	77.7	3.33	11.23	20.74

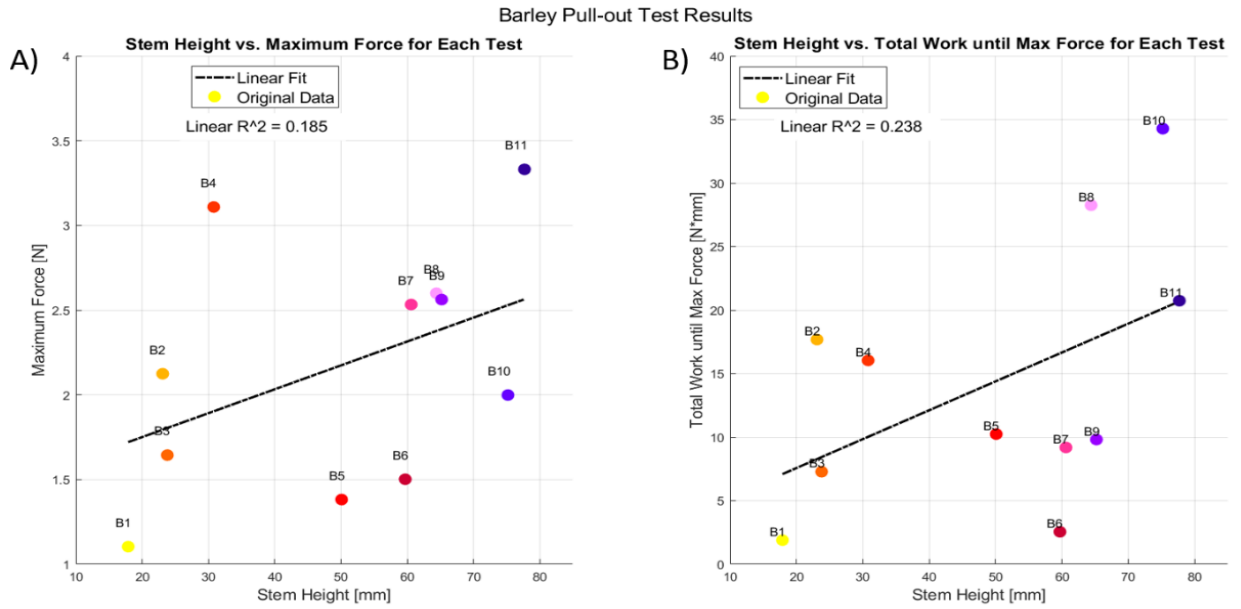

Figure 15: A) Plot of maximum force as a function of stem height, B) Plot of work at the point of maximum force as a function of stem height for barley seeds. The blue dotted line indicates the linear fit, while the dots represent the actual measured data.

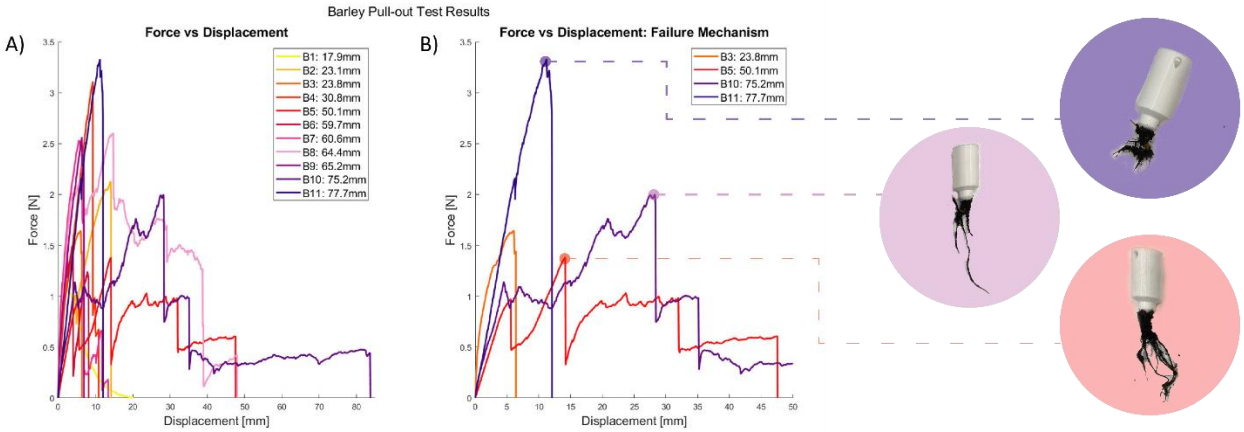

Figure 16: A) Plot of force vs displacement for all barley seeds tested, B) Selected curves with distinct patterns were chosen to highlight the variations in curve shapes. Additionally, a photograph of the intact roots remaining after the pullout test is included for sample B5, B10 and B11.

The same testing procedure was applied to mung bean seeds, although only 8 samples were tested, unlike the 11 samples for barley seeds. Table 12 presents all the data obtained from the tests and subsequent post-processing. Figure 17 illustrates the relationship between maximum force, work done until the maximum force and stem height. For the mung bean samples, there is a positive relationship between stem height and both maximum force and work until the maximum force. This relationship is notably stronger than that observed in barley, with a higher R^2 value of 0.741 for maximum force and 0.558 for work at maximum force, indicating a strong linear correlation. However, variability among individual tests is still evident, as reflected in the data points' spread around the trend line.

Figure 18a displays force versus displacement curves for all mung bean tests, providing an overview of the force-displacement behavior across various stem heights. Figure 18b highlights a subset of four tests, chosen to showcase differences in failure mechanisms. In tests M1 and M2, force increases with displacement until reaching a peak, followed by a sharp drop to zero, indicating abrupt failure. In contrast, tests M7 and M8 exhibit a more complex pattern with multiple peaks, suggesting progressive failure, where the root system may experience partial failures but continues to resist further displacement. Photographs of the intact roots remaining after the pullout test are included for samples M1 and M7. For sample M1, only the broken taproot is visible, while for sample M7, both the broken taproot and some secondary branches are present.

Table 12: Data obtained from mung bean pull-out test results.

	Test denomination	Stem length [mm]	Maximum Force [N]	Displacement at the Max Force [mm]	Work until the Max Force [N*mm]
Test 1	M1	32.5	0.49	4.75	0.79
Test 2	M2	39.7	0.60	12.29	2.85
Test 3	M3	40.1	0.95	4.55	2.65
Test 4	M4	119.8	1.29	3.43	3.13
Test 5	M5	121.5	1.06	6.02	4.54
Test 6	M6	123.8	1.40	2.96	2.86
Test 7	M7	145.2	1.12	7.82	4.64
Test 8	M8	156.1	1.76	3.31	3.67

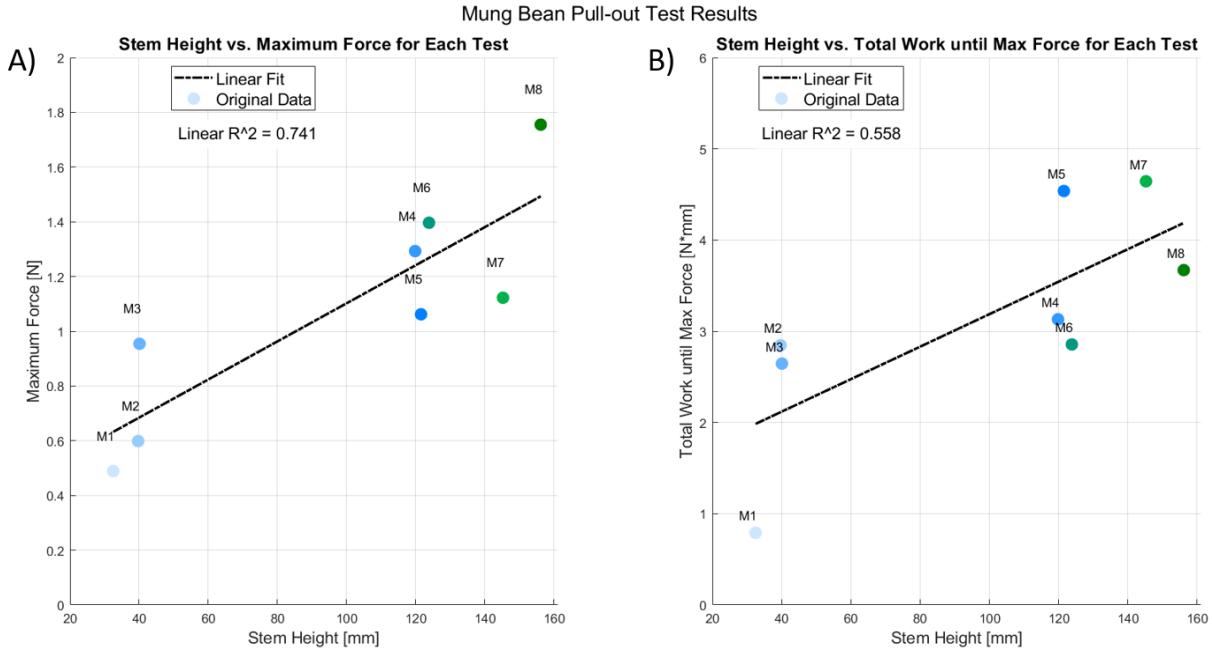

Figure 17: A) Plot of maximum force as a function of stem height, B) Plot of work at the point of maximum force as a function of stem height for mung bean seeds. The blue dotted line indicates the linear fit, while the dots represent the actual measured data.

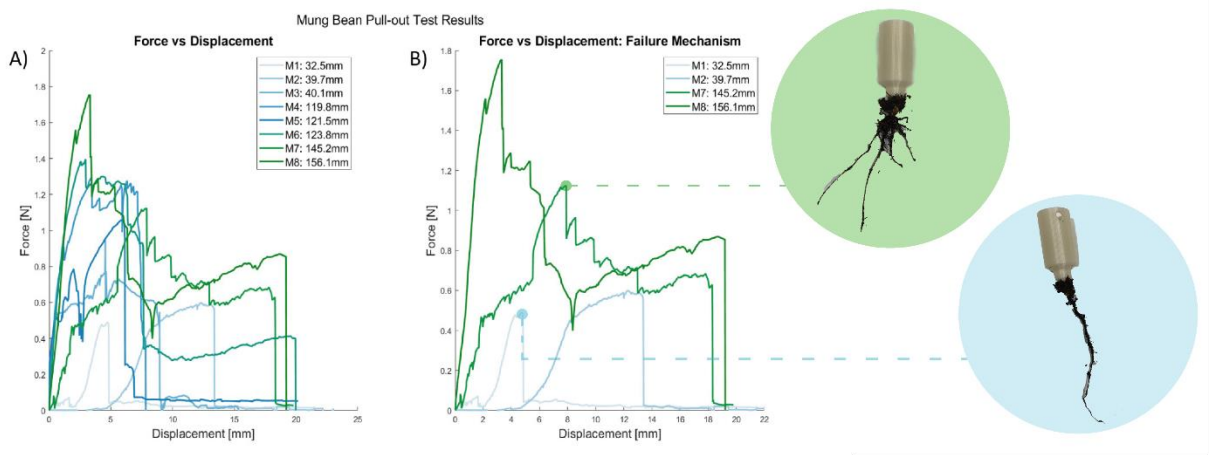

Figure 18: A) Plot of force vs displacement for all mung bean seeds tested, B) Selected curves with distinct patterns were chosen to highlight the variations in curve shapes. Additionally, a photograph of the intact roots remaining after the pullout test is included for sample M1 and M7.

Figure 19 presents a bar plot of maximum force as a function of stem height for both barley and mung bean samples, with the mung bean samples distinguished by a hatch pattern. Several key observations can be made. Barley samples generally demonstrate a higher range of maximum forces compared to mung bean samples. For instance, the highest maximum force in barley (B11) exceeds 3N, whereas the highest in mung bean (M8) reaches just above 1.7N. Furthermore, within similar stem height ranges, such as around 20mm and 40mm, barley samples (B2, B3, and B4) exhibit noticeably higher maximum forces compared to mung bean samples (M1, M2, and M3). This implies that barley roots have greater mechanical resistance than mung bean roots at comparable or lower stem heights, suggesting differences in the mechanical properties or structural strength of the two plant species.

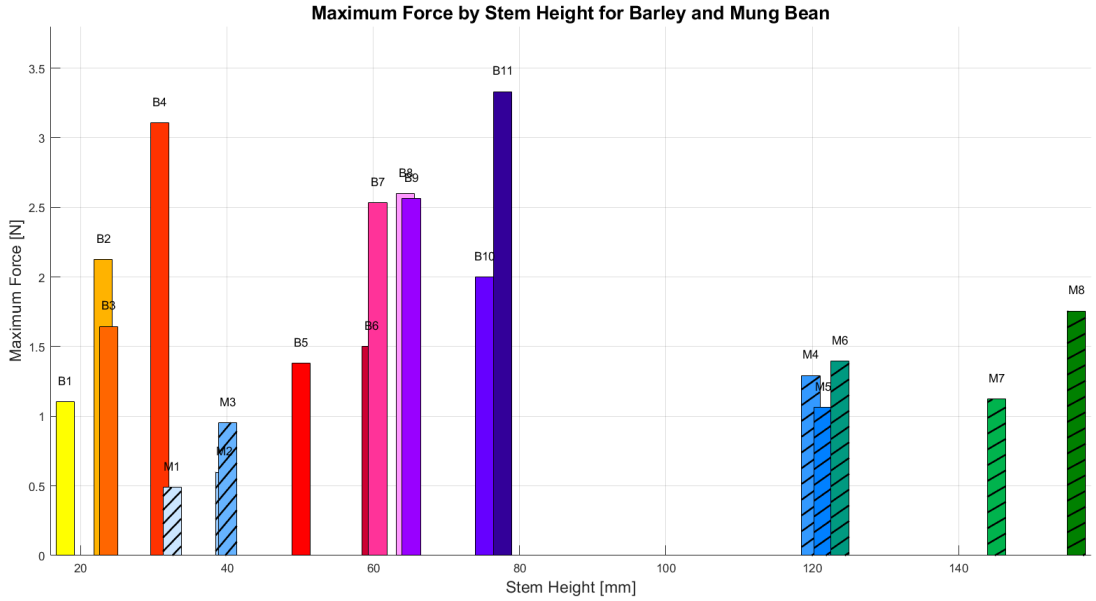

Figure 19: Comparison of maximum force by stem height for barley and mean bung seeds.

3.3 Results from CT Scanning

For each CT scan presented, the images in the left column show the top view, while the middle and right columns provide two different side views. The color scale at the bottom of each image indicates the distance from the origin, which is consistently set to the first slice of each scan at the center of the initial root structure. The scale progresses from dark purple, representing areas closest to the origin, to yellow, indicating the furthest points. In the upper left corner of each image, a scale bar shows either 1 cm or 1 mm, depending on the level of zoom, providing a visual reference for the actual size of the roots.

Four CT scans were performed on barley seeds, all taken seven days after planting in soil. Only the first 500 significant slices from each scan were processed, as shown in Figure 20. The scans are labeled A, B, C, and D to differentiate between them. Processing was limited to the first 500 slices due to the computational demands of post-processing, which requires powerful processors. These slices were sufficient to capture the overall architecture of the barley root system, offering a representative view of the root structure at this growth stage.

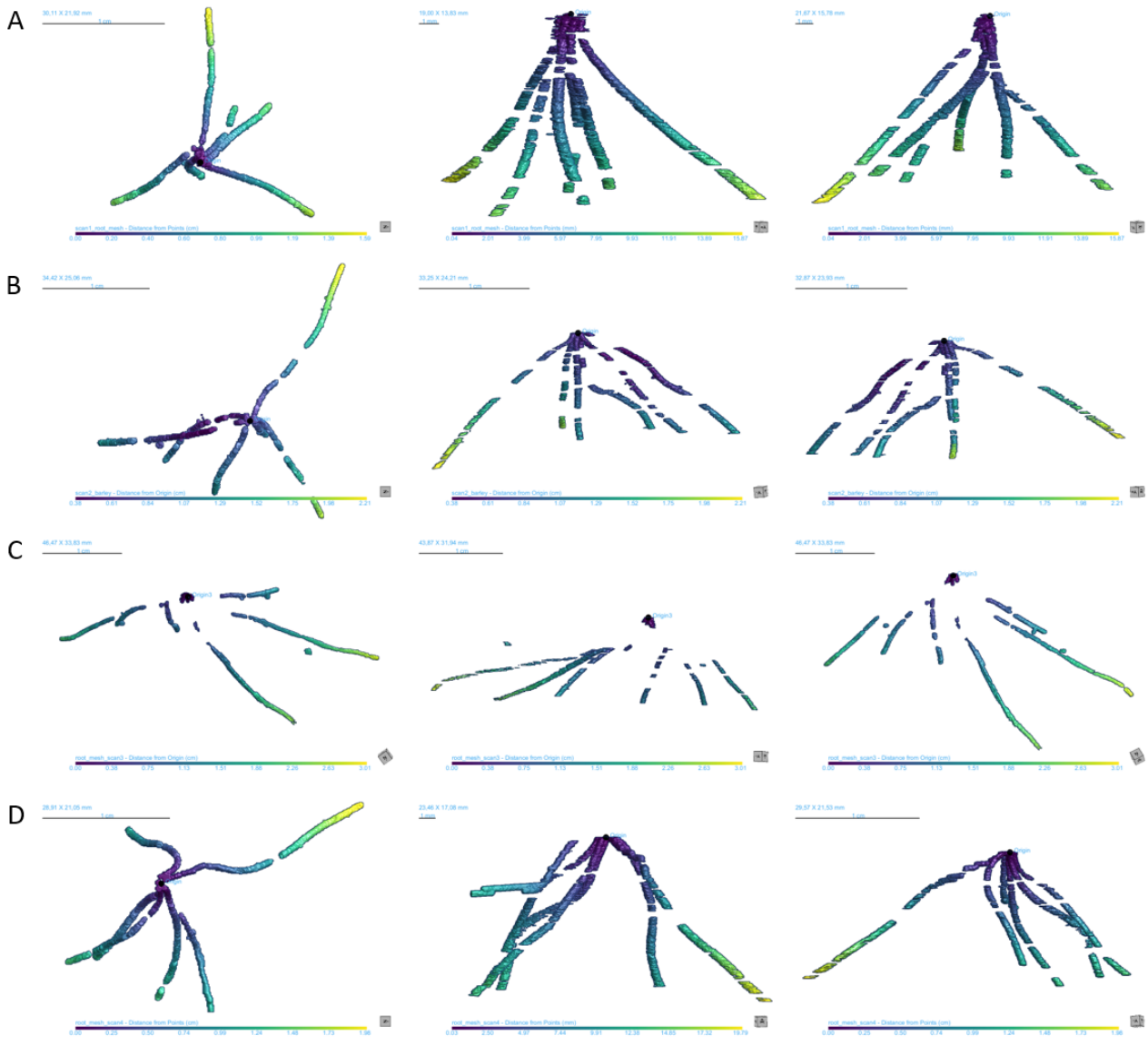

Figure 20: CT scans of barley roots seven days after planting, consisting of four scans in total, labeled A, B, C, and D. The left column shows top views, and the middle and right columns present two side views.

Each scan reveals six seminal roots per barley seedling, a typical characteristic indicating a normal initial growth phase across all samples. The roots in each scan maintain a consistent diameter of approximately 0.5 mm. However, the root lengths vary not only between scans but also within each scan due to differences in individual root orientation. For instance, the longest roots measure 15.87 mm in scan A, 22.1 mm in scan B, 30.1 mm in scan C, and 19.8 mm in scan D. Since each post-processed scan includes only the first 500 slices, the roots are expected to be longer than what is captured here. Variations in branching angles are also evident. The vertical branching angle varies, with the smallest angle observed at 10° in scan A and the largest at 80° in scan B. Radial branching angles differ significantly within each scan. In scan A, for example, the roots are organized into two groups of three with narrow angles within each group but separated by angles of approximately 80° and 120° between groups. By contrast, in scan D, the roots are arranged in three groups of two, with each group closely spaced together, while distances between groups range from 60° to 90°. For the initial 500 slices, no adventitious or secondary branches are present. However, each root displays a degree of tortuosity, contributing to the variation in orientation and positioning observed across the scans.

Scan B was randomly selected from the four scans and processed further with an additional 500 slices to explore potential insights at greater depths. In this extended scan, the seminal roots are observed to elongate up to 31 mm, with adventitious roots becoming visible from approximately 20 mm onward. Each adventitious root emerges as a single branch from distinct points along the seminal roots. The adventitious roots have a diameter similar to the seminal roots, being only slightly narrower by about 0.1 mm to 0.2 mm. The overall root structure appears to lack organization, with roots displaying a completely random orientation rather than a specific pattern. In Figure 21 , the left side shows a top view (top row) and a diagonal view (bottom row), while the right side displays two side views. The additional slices provide a more detailed view of the branching dynamics and the onset of adventitious root development as the roots extend further.

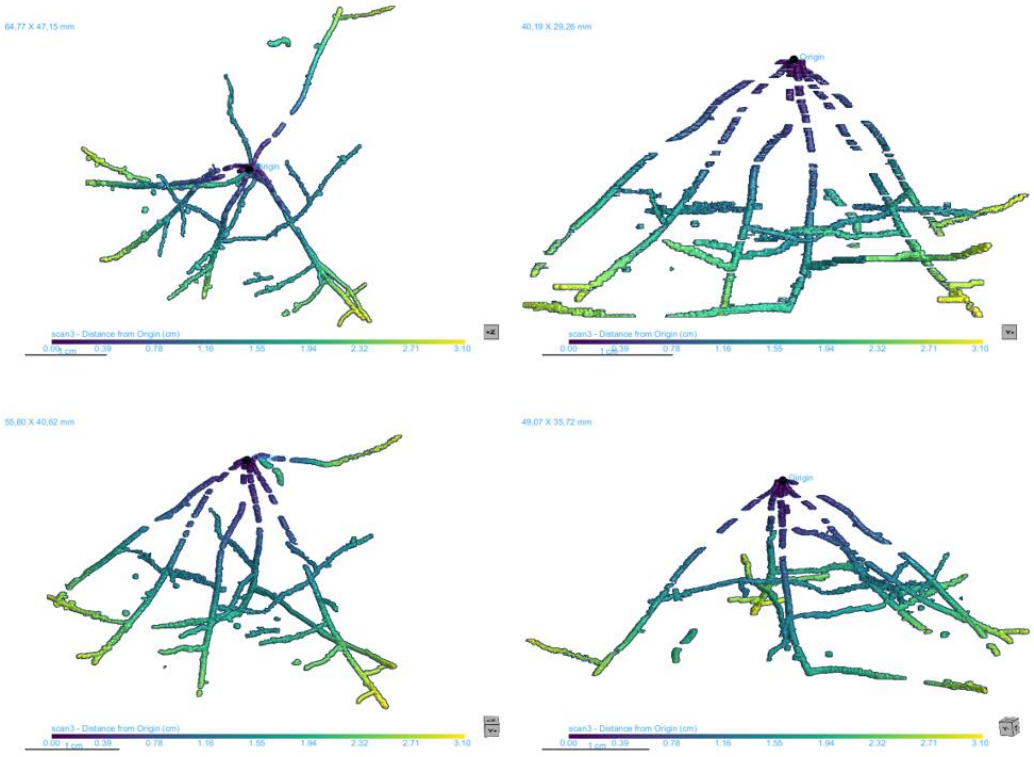

Figure 21: CT scan results for scan B with a total of 1000 slices processed.

For the mung bean, only two scans were conducted: one after 7 days of growth and the other after 13 days. Given the simplicity of the root structure, the first 1000 slices were post-processed since it required less computational demand in respect to the barley scan. In Figure 22, scan A captures the 7-day growth stage while scan B represents the 13-day stage. Both scans reveal a primary taproot with a length of 20 mm, a consistent diameter of 1 mm throughout, and a degree of tortuosity. In scan A, only the taproot is present, with no secondary branching observed. In contrast, scan B shows the development of secondary roots, each emerging from distinct branching points along the taproot. These roots measure approximately 10 mm in length, have a diameter of about 0.7 mm, and display a slight curvature. Their vertical branching angle is approximately 45°.

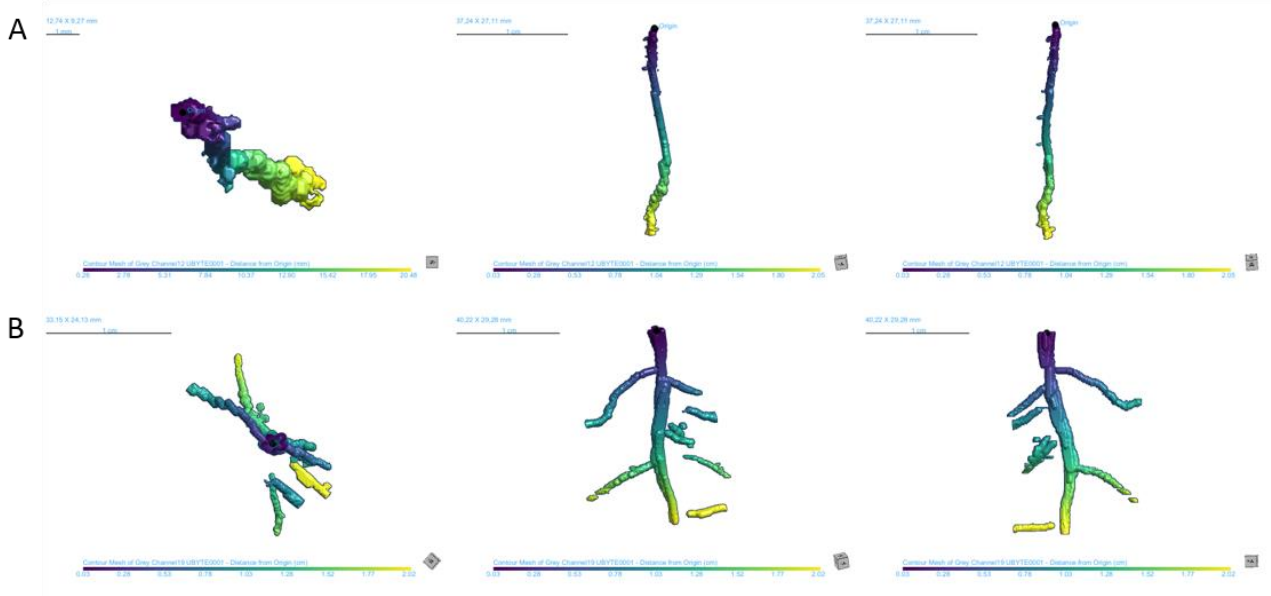

Figure 22: CT scans of mung bean roots: scan A taken 7 days after planting, and scan B taken 13 days after planting. The left column displays top views, while the middle and right columns show two side views.

3.4 Results from FEM Analysis

This chapter presents the results of the FEM simulations, focusing on the analysis of barley and mung bean root behavior in different test configurations.

3.4.1 Barley Root Configuration Results

Plots and numerical results

Figure 23 illustrates the simulation outcomes for barley roots, with plots organized as follows: the first row displays force versus displacement curves, the second row provides histograms of maximum force for each configuration, and the third row shows histograms of the work done up to the maximum force for each configuration. Additionally, these final results are presented numerically in Table 13, which includes the simulation number, the specific barley root model used in each simulation, the substrate type, the label assigned to that specific results in Figure 23, and the displacement corresponding to the maximum force.

The columns are arranged by configuration to enable easy comparisons, with soil represented by solid bars and hydrogel by hatched bars. In the first column, results are provided for three configurations tested in soil and three in hydrogel, each exploring the influence of vertical branching angle on pullout force. For soil, the 45° branching angle produced the highest maximum force, reaching 5.09 N, followed closely by the 80° angle with a maximum force of 4.37 N. The 15° angle demonstrated significantly less strength, reaching only 2.84 N, approximately 56% of the force produced by the 45° angle. In hydrogel, the 80° angle produced the highest maximum force at 4.98 N, followed by the 45° angle at around 3.20 N (60% of the 80° result). The 15° angle showed the lowest force, at 1.04 N. The work done up to the maximum force follows a similar pattern to the force results, the only notable difference is the displacement at which maximum force is achieved in each medium. For instance, in hydrogel, the 80° angle reached maximum force at a displacement of 4.04 mm, nearly twice the displacement observed in soil, where the same configuration reached the maximum force at 1.99 mm displacement. This indicates that in hydrogel, higher displacement is required to achieve maximum pullout force.

The second column displays the configurations used to assess the effect of the radial branching angle on pullout force. In soil, the maximum force across all configurations remains relatively consistent, ranging from 5.09 N to 5.38 N, a difference of only 8%. Similarly, in hydrogel, the maximum forces are closely matched, ranging from 3.06 N to 3.30 N, showing a variation of approximately 10%. Overall, soil consistently exhibits higher maximum forces than hydrogel for all radial branching configurations. However, as observed with the vertical branching angle, hydrogel requires a greater displacement to reach maximum force. In soil, maximum force is achieved at displacements ranging from 1.03 mm to 1.67 mm, whereas in hydrogel, the displacement needed is nearly double, ranging from 3.01 mm to 3.47 mm.

The last column of Figure 23 compares the effects of root straightness versus tortuosity in both soil and hydrogel mediums. In soil, the tortuous root demonstrates nearly double the maximum force of the straight root, with the tortuous configuration reaching about 9.80 N, while the straight root achieves only 5.09 N. In contrast, tortuosity has a much smaller impact in hydrogel, where the maximum force for the straight root is 3.20 N, compared to 3.61 N for the tortuous root, a difference of just under 10%. Displacement at maximum force also varies notably between configurations and substrate. For the straight root, hydrogel requires around 3.01 mm of displacement to reach maximum force, whereas in soil, this displacement is approximately 1.03 mm. Interestingly, for the tortuous root, maximum force in soil is reached at nearly 5.84 mm of displacement, significantly higher than the 3.54 mm needed in hydrogel.

Initially, all simulations were set to run until 4 seconds, corresponding to a displacement of 4 mm, as most configurations had already reached maximum force by this point. However, after reviewing the processed results, it was observed that in the 80° configuration for hydrogel and the tortuous configuration in soil, the force was still increasing at 4 mm. Consequently, these two simulations were extended to 8 seconds,

corresponding to 8 mm displacement, to capture the full force profile. Additionally, although the tortuous configuration in hydrogel reached maximum force at a displacement of 3.22 mm, it was also re-run up to 8 mm to ensure no critical data was missed. This approach provided a comprehensive view of force behavior across all configurations.

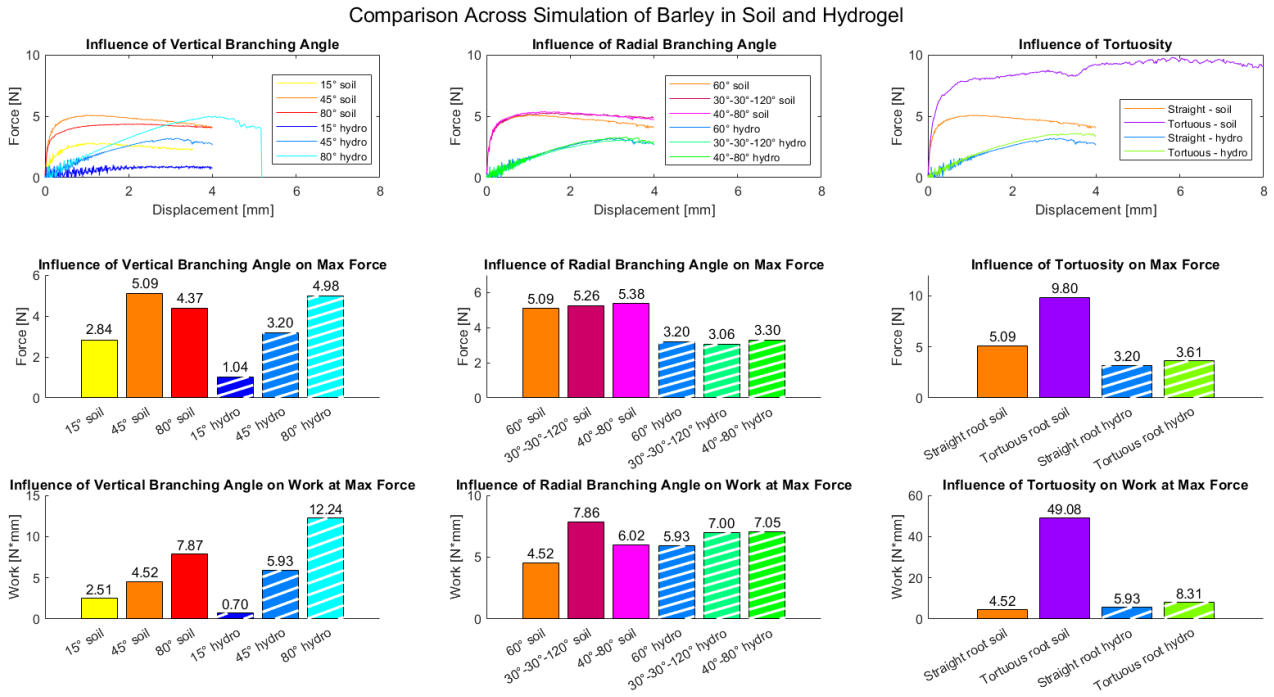

Figure 23: Plots of FEM simulation results for barley root models in soil and hydrogel mediums.

Table 13: Numerical results from FEM simulations for barley roots in soil and hydrogel mediums.

Simulation number	Barley Root Model tested	Substrate	Test Label in Figure 23	Maximum force [N]	Displacement at the max force [mm]	Work until max force [N*mm]
1	1	Soil	45° soil / 60° soil / straight - soil	5.09	1.03	4.52
2	2	Soil	80° soil	4.37	1.99	7.87
3	3	Soil	15° soil	2.84	1.14	2.51
4	4	Soil	40°-80° soil	5.38	1.29	6.02
5	5	Soil	30°-30°-120° soil	5.26	1.67	7.86
6	6	Soil	Tortuous - soil	9.80	5.84	49.08
7	1	Hydrogel	45° hydro / 60° hydro / straight - hydro	3.20	3.01	5.93
8	2	Hydrogel	80° hydro	4.98	4.04	12.24
9	3	Hydrogel	15° hydro	1.04	1.63	0.70
10	4	Hydrogel	40°-80° hydro	3.30	3.33	7.05
11	5	Hydrogel	30°-30°-120° hydro	3.06	3.47	7.00
12	6	Hydrogel	Tortuous - hydro	3.61	3.54	8.31

Contour plots

The following section presents contour plots for vertical displacement, stress distribution, and strain distribution within the root-substrate system across all barley model configurations. The vertical displacement measures how much the root-substrate system moves vertically along the z-axis. By assessing vertical displacement, we can observe how the substrate (soil or hydrogel) displace in response to pullout forces exerted by the root. This analysis provides insights into the medium's behavior in response to the root's movement.

To evaluate the stress distribution in the root model, the Von Mises equivalent stress criterion was selected. Since the root experiences a multiaxial stress condition under pullout forces, Von Mises stress is ideal for analyzing the combined stress state within the root, which has been modeled as an elastic material with certain plasticity. The Von Mises stress distribution within the root helps to reveal critical areas that may reach yield under maximum pullout forces, capturing where material failure may begin.

For the strain distribution within the soil, Plastic Equivalent Strain (PEEQ) was used, as the soil is modeled as an elastic-perfectly plastic material following the Mohr-Coulomb failure criterion. PEEQ effectively captures permanent deformation, showing areas where the soil has exceeded its elastic limit and undergone plastic (irreversible) strain due to the interaction with the root. This measure condenses the multiaxial strain state into a single value, simplifying the analysis of plastic deformation within the soil and providing insight into where yielding occurs. Logarithmic Strain (LE) was chosen to evaluate strain distribution in hydrogel, as it is modeled as a hyperelastic material capable of withstanding large, recoverable deformations. LE is suitable for hyperelastic materials like hydrogel because it measures large elastic deformations without indicating permanent (plastic) changes, effectively capturing the degree of elastic stretch under load.

The vertical displacement and strain distribution, both LE and PEEQ, were measured at a standardized time step of 4 seconds, corresponding to a displacement of 4mm, to enable direct comparison across all configurations, as the shortest simulation concluded at this time. On the other hand the Von Mises stress was measured at the time step corresponding to the maximum pullout force for each configuration, representing the point of highest load experienced by the material. Because stress is taken at peak force, which varies by configuration, direct comparisons between configurations are less meaningful, as each configuration reaches its peak force at different times.

Figure 25 through Figure 29 each correspond to a different model tested. In each figure, there are 3 rows and 2 columns: the rows display stress distribution, strain distribution and vertical displacement, respectively. The left column shows results for the root models tested in soil, while the right column displays results for those tested in hydrogel. Each image includes a bounding box in the top left corner, indicating the minimum and maximum values of the measured variable. The images are color-coded to represent the range of values, with red indicating the maximum and blue the minimum. This color scheme provides a clear visual reference for assessing the variation in values. The units for the values shown in the legend are as follows: von Mises stress is measured in MPa, PEEQ and Le are dimensionless, and vertical displacement is measured in mm.

MODEL 1, test labels: 45° / 60° / straight

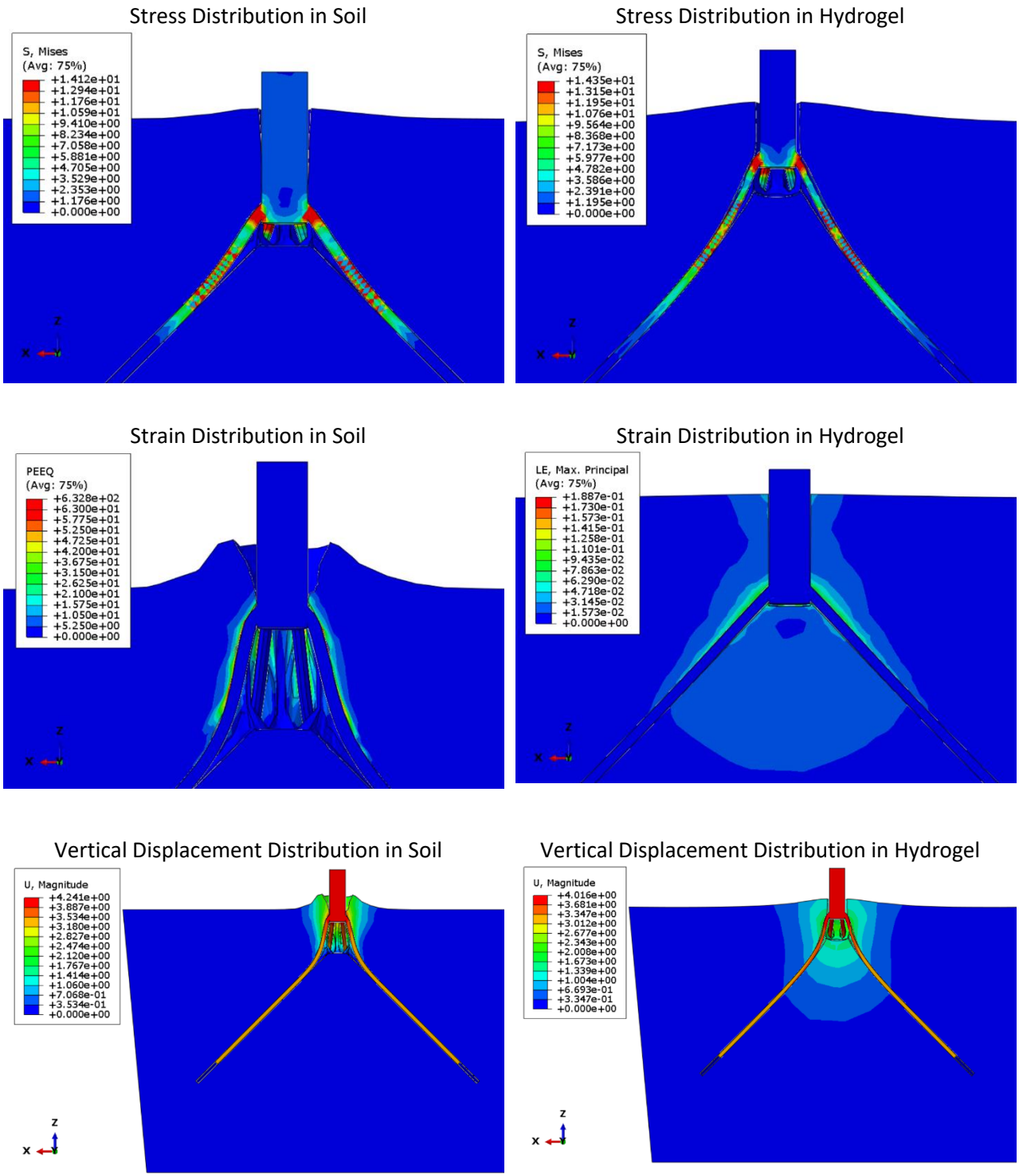

Figure 24: Snapshot of stress distribution, strain distribution and vertical displacement in soil and hydrogel for barley model 1.

MODEL 2, test label: 80°

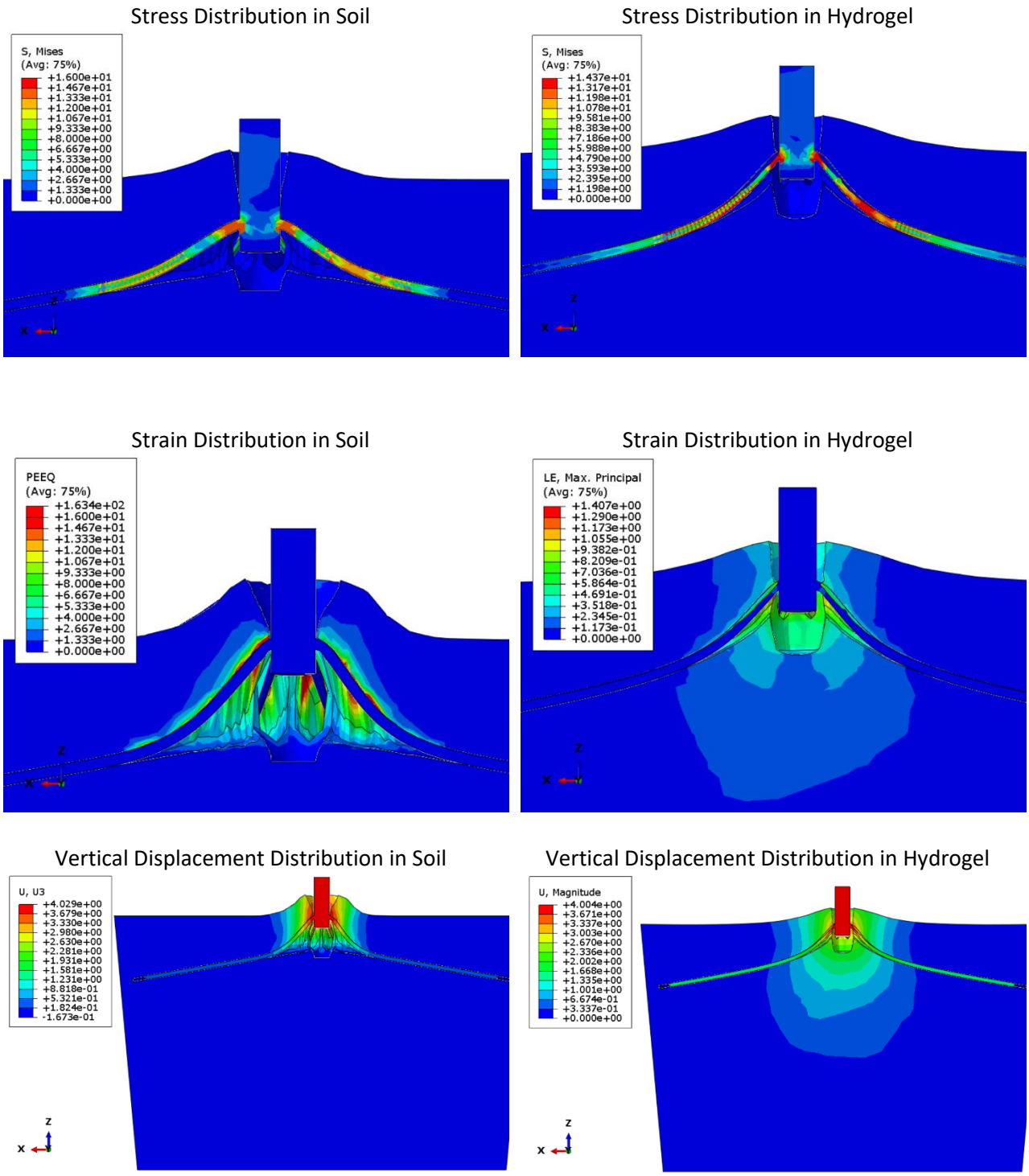

Figure 25: Snapshot of stress distribution, strain distribution and vertical displacement in soil and hydrogel for barley model 2.

MODEL 3, test label: 15°

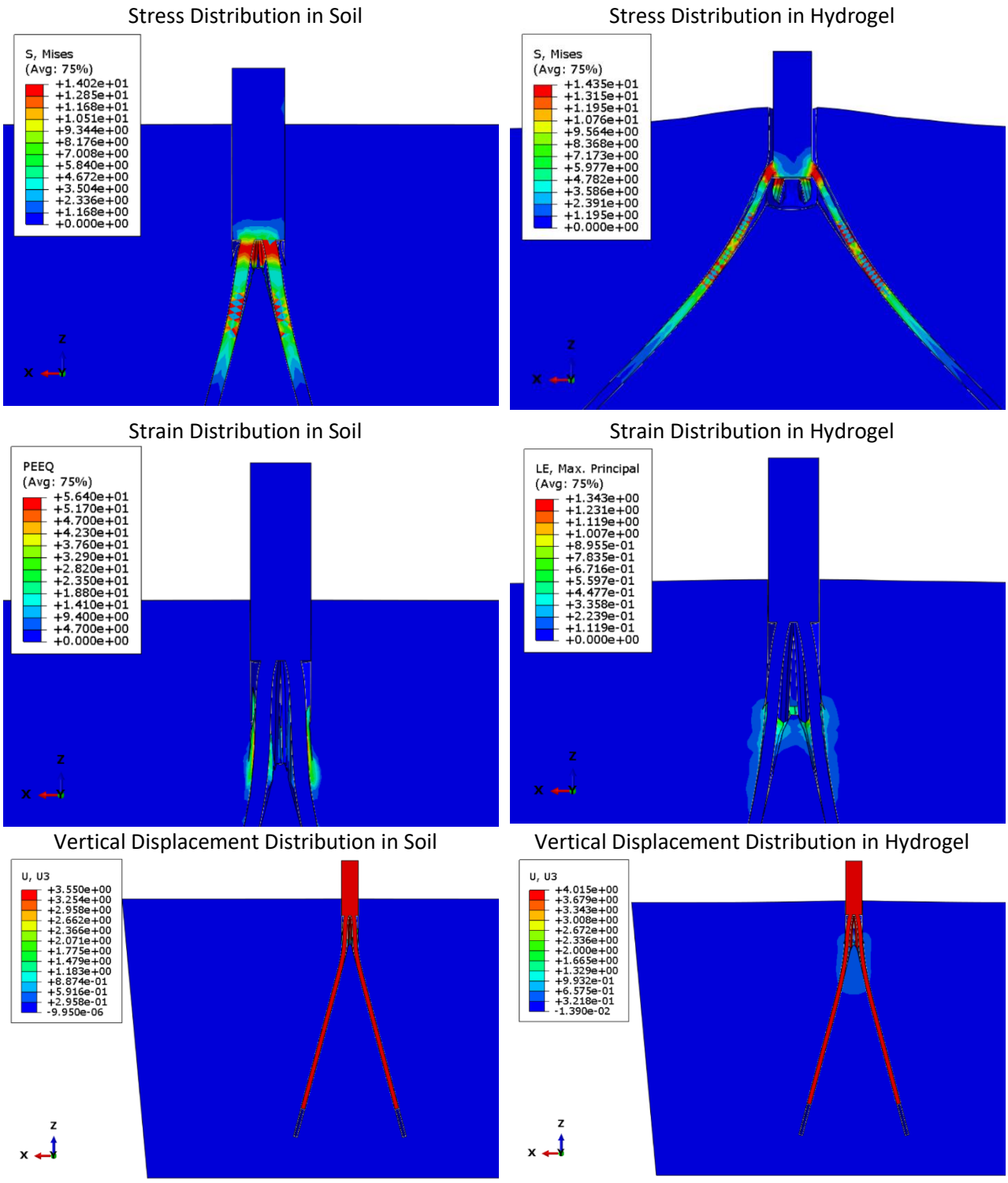

Figure 26: Snapshot of stress distribution, strain distribution and vertical displacement in soil and hydrogel for barley model 3.

MODEL 4, test label: 40° - 80°

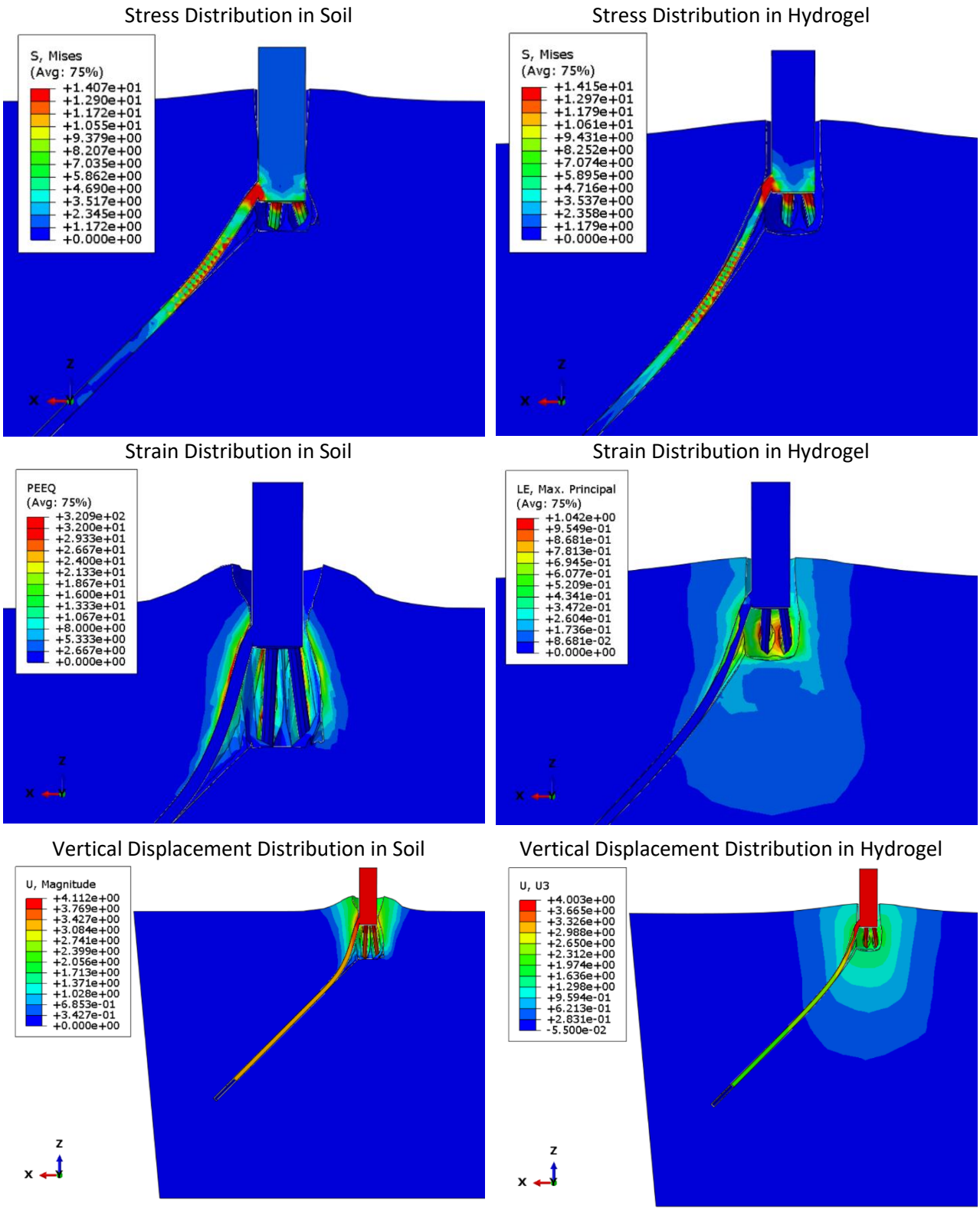

Figure 27: Snapshot of stress distribution, strain distribution and vertical displacement in soil and hydrogel for barley model 4.

MODEL 5, test label: 30°-30°-120°

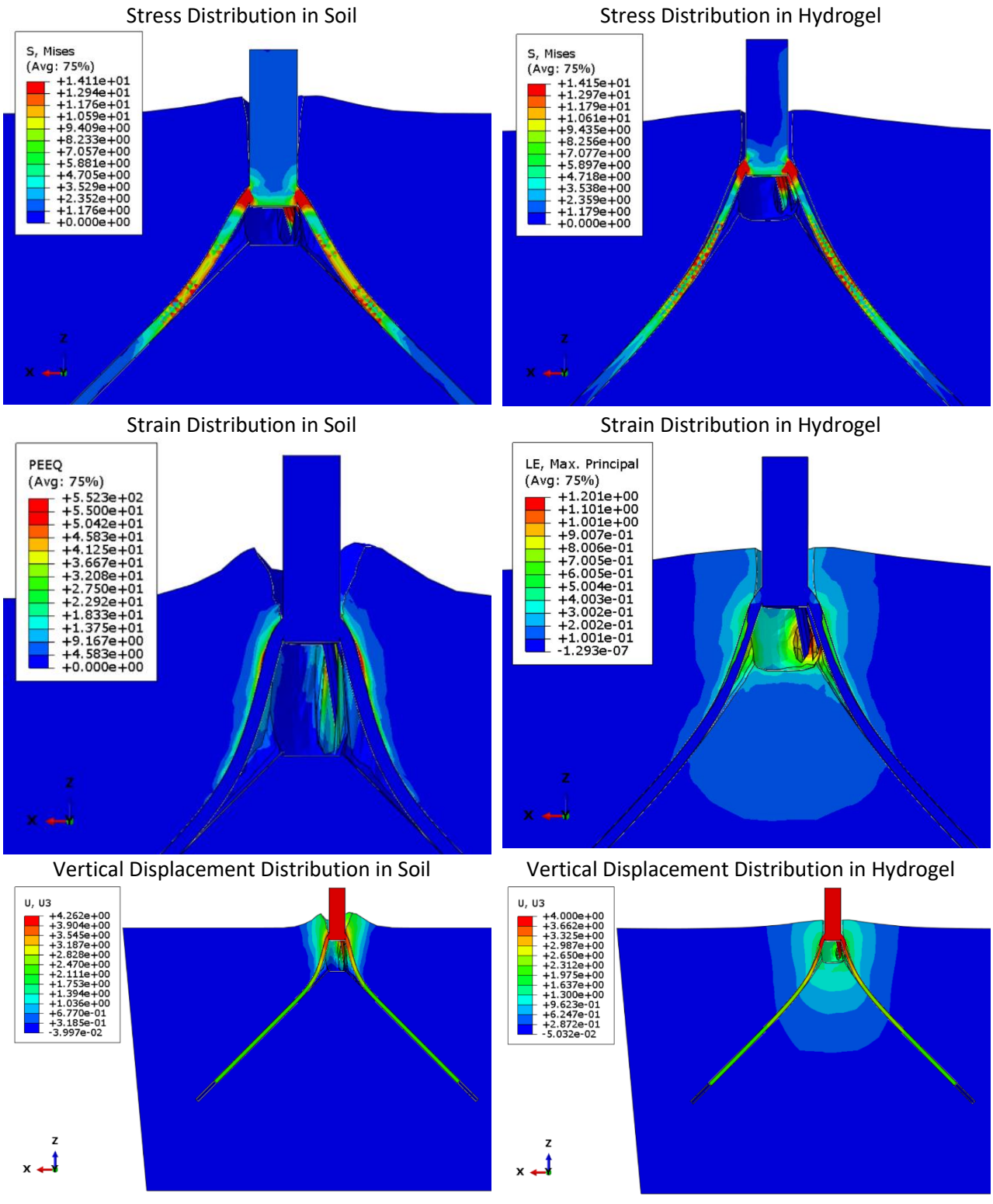

Figure 28: Snapshot of stress distribution, strain distribution and vertical displacement in soil and hydrogel for barley model 5.

MODEL 6, test label: tortuous

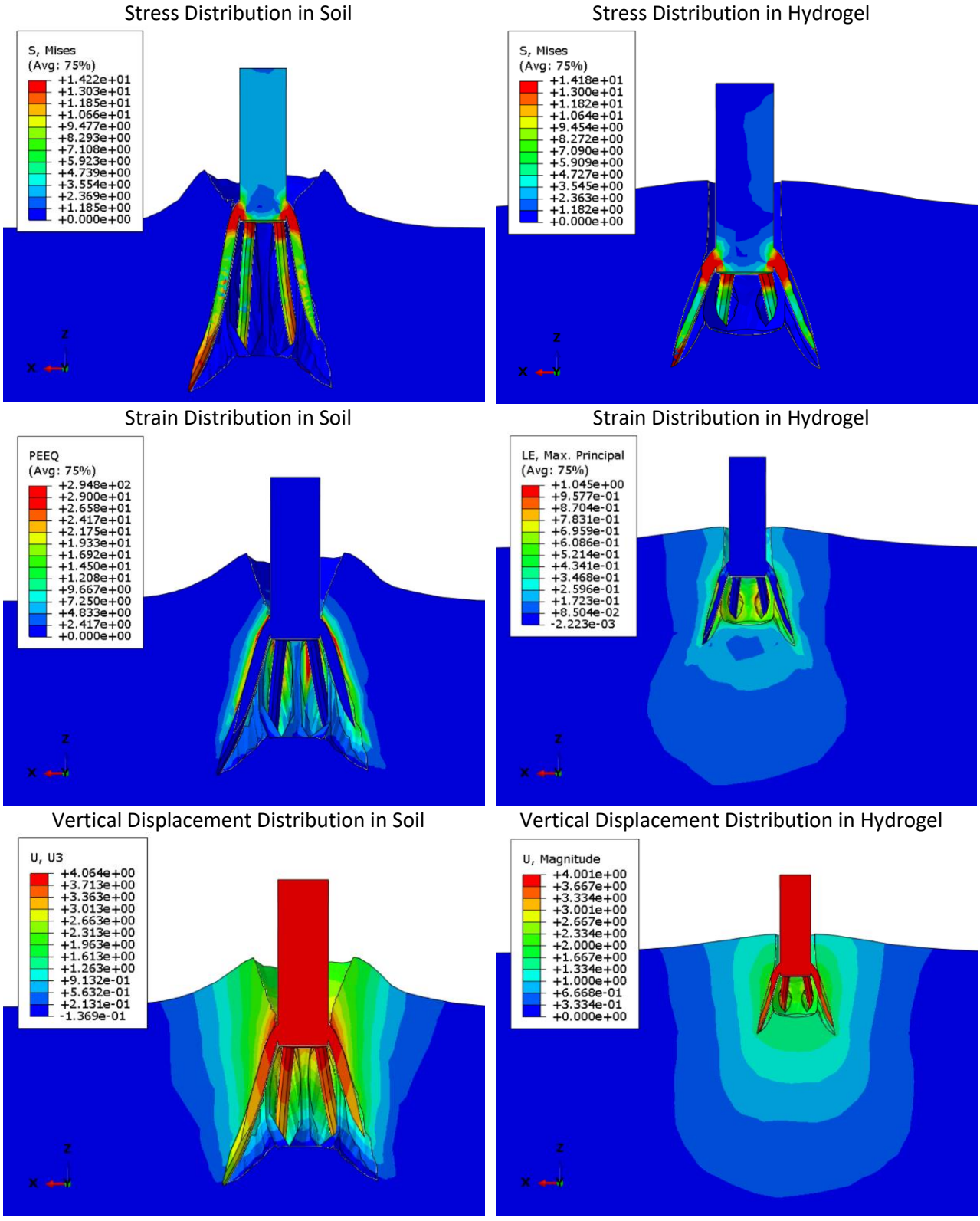

Figure 29: Snapshot of stress distribution, strain distribution and vertical displacement in soil and hydrogel for barley model 6.

In examining stress distribution across all models and mediums, it is evident that stress is primarily concentrated in two main regions: where the root connects to the seed, and where the root interfaces with the substrate as it pushes against it during pullout tests. Essentially, depending on the root model, varying sections of the root are in active contact with the substrate, exerting force and generating stress concentrations along its length. A clear example of this behavior is illustrated in the first three models, shown Figure 24, Figure 25 and Figure 26, which vary only in their vertical branching angles. As the vertical branching angle increases, the portion of the root experiencing concentrated stress extends further along its length. This occurs due to the increased perpendicular contact between the root and the medium, leading to a larger section of the root actively engaging with the substrate during pullout.

In both soil and hydrogel substrates, the strain distribution is concentrated in areas where the root applies pressure during pullout. For the plastic equivalent strain in soil, this pattern is observed across all models: strain is highest at points where the root actively pushes against the soil, creating concentrated areas of deformation that gradually diminish outward. In contrast, near the root's end, where it remains in contact but isn't actively pushing against the soil, strain remains zero, as no deformation occurs without active force. In hydrogel, a similar pattern appears with logarithmic strain, where strain is highest near the initial root sections pressing against the substrate. However, unlike in soil, hydrogel deformation extends across a broader surrounding area due to its elastic properties.

In both substrate, the strain distribution is focused in areas where the root applies pressure during pullout. This effect is especially noticeable in Models 4 and 5, which have different radial branching angles. In the 30°-30°-120° configuration (Model 5, Figure 29), strain is concentrated on the side of the substrate where three roots are closely clustered, causing significant deformation in that region. Conversely, parts of the substrate without root contact show no deformation due to the lack of applied pressure. A similar pattern appears in the 48°-80° configuration (Model 4, Figure 28). This distribution shows how root clustering increases strain in certain areas, while regions without direct root contact remain unaffected. This effect is particularly pronounced in Models 4 and 5, where roots are unevenly spaced. In the 30°-30°-120° configuration (Model 5, Figure 28), strain is concentrated on the side of the substrate where three roots are closely clustered, causing significant deformation in that region. Similarly, the 48°-80° configuration (Model 4, Figure 27) shows how root clustering amplifies strain in specific areas, while regions without direct root contact remain unaffected.

Just as with strain, vertical displacement increases in areas where the root pushes outward during pullout, displacing the surrounding medium. This effect is noticeable in Models 1, 2, and 3. As the vertical branching angle increases, so does the displacement in both soil and hydrogel, with the 45° configuration (Model 1, Figure 24) and 80° configuration (Model 2, Figure 25) showing greater displacement than the 15° configuration (Model 3, Figure 26). While the radial branching angle does not impact displacement magnitude, it affects the distribution pattern. In the 60° equidistant configuration (Model 1, Figure 24), displacement is symmetrically distributed around the z-axis in both mediums. However, this symmetry is lost in the 30°-30°-120° (Model 5, Figure 28) and 48°-80° configurations (Model 4, Figure 27), where displacement is concentrated on the side with clustered roots. This clustering effect shows how root arrangement can influence the spatial pattern of displacement in the medium.

A final key observation is the distinct behavior of soil and hydrogel in terms of deformation and displacement, consistently seen across all simulations. In each test, soil exhibits localized deformation and displacement around the root during upward pullout, creating a concentrated zone that often causes the soil to 'break' and separate around the root. In contrast, hydrogel responds more uniformly, with strain and displacement distributed evenly throughout the medium rather than concentrated near the root. This even distribution allows hydrogel to stretch without breaking or separating around the root in any of the simulations.

Energy History Output

Next, the energy history output, as shown in Figure 30, is analyzed for a single model: barley model 6 in soil. This model was selected because it exhibited the highest maximum pullout force among all barley models analyzed across both substrates, making it the most critical case for evaluation. The internal energy steadily increases with displacement and time, alongside the external work done. Both the kinetic energy and artificial strain energy remain at 0 throughout the simulation. The total energy of the system varies between 0 and 0.13 N*mm.

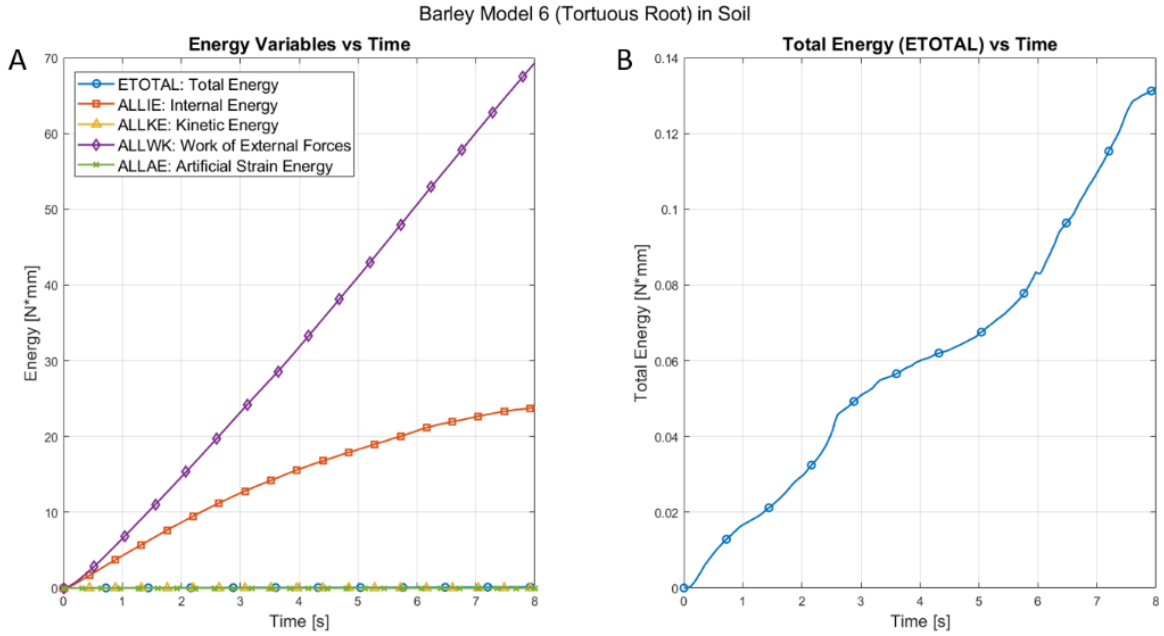

Figure 30: A) Plot showing various energy outputs obtained through ABAQUS over the simulation time step, including total energy, internal energy, kinetic energy, artificial strain energy, and the work of external forces. B) Displays only the total energy plot versus time. Both plots are based on simulations of barley model 6 in soil.

3.4.2 Mung Bean Root Configuration Results

Plots and numerical results

Figure 31 illustrates the simulation outcomes for mung bean roots, while Table 14 presents the corresponding numerical results. It also includes the simulation number, the specific mung bean root model used in each simulation, the substrate type, the label assigned to these results in Figure 31, and the displacement corresponding to the maximum force. Three configurations were studied for mung bean roots: a simple root without branching, a configuration with one secondary branch at each branching point, and a multiple-branch configuration with three branches per point. Soil is represented by solid bars, while hydrogel is illustrated with hatched bars. Overall, the pullout force was higher in soil than in hydrogel, while displacement at maximum force was consistently higher in hydrogel. In the configuration without branches, maximum pullout forces were nearly identical, with 0.34 N in soil and 0.36 N in hydrogel, a difference of just under 6%. For the single-branch configuration, soil showed a significantly higher force, reaching 9.17 N compared to 3.22 N in hydrogel. The multiple-branch configuration also showed higher pullout forces in soil, with 12.78 N compared to 8.66 N in hydrogel, representing a 47.6% increase. In terms of displacement, the configuration without branches exhibited similar values, with 0.40 mm in soil and 0.85 mm in hydrogel. For the single-branch configuration, displacements were 2.55 mm in soil and 5.28 mm in hydrogel, more than doubling in hydrogel. Finally, for the multiple-branch configuration, soil had a displacement of 3.08 mm, while hydrogel reached 6.35 mm.

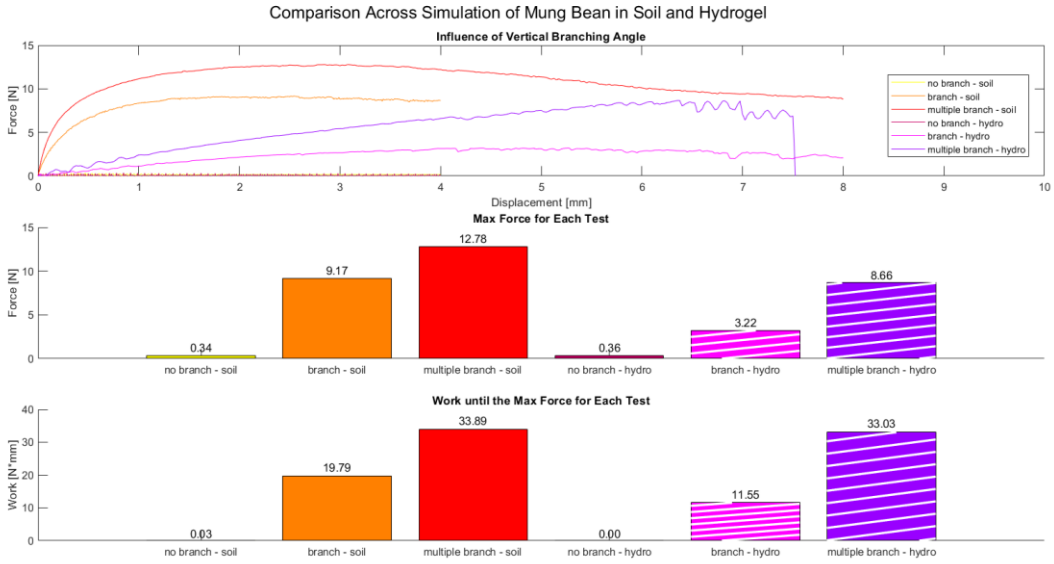

Figure 31: Plots of FEM simulation results for mung bean root models in soil and hydrogel mediums.

Table 14: Numerical results from FEM simulations for mean bean roots in soil and hydrogel mediums.

Simulation number	Mung Bean Root Model Tested	Substrate	Test Label in Figure 31	Maximum force [N]	Displacement at the max force [mm]	Work until max force [N*mm]
13	1	Soil	No branch - soil	0.34	0.40	0.03
14	2	Soil	Branch - soil	9.17	2.55	19.79
15	3	Soil	Multiple branch - soil	12.78	3.08	33.89
16	1	Hydrogel	No branch - hydro	0.36	0.85	0.00
17	2	Hydrogel	Branch - hydro	3.22	5.28	11.55
18	3	Hydrogel	Multiple branch - hydro	8.66	6.35	33.04

Furthermore, FEM simulation allows to analyze the variation in maximum pullout force relative to the surface area of the root structure. This analysis was not feasible for the barley models, as their surface areas were too similar across different models to provide meaningful insights into the relationship. In contrast, the mung bean models, as detailed in Table 7 in Section 2.4.2, exhibit significant differences in surface area, with a range of 123.384 mm², making such an analysis possible. Figure 32 shows the plot of maximum pullout force versus surface area for the mung bean models in both soil and hydrogel, along with the linear fitting curves and coefficients of determination for each substrate. A positive linear correlation is observed in both substrates, indicating that an increase in surface area corresponds to a higher maximum pullout force. The coefficient of determination (R^2) is 0.7311 for soil and 0.7279 for hydrogel, indicating a moderately strong linear relationship between surface area and maximum pullout force in both substrates. Moreover, the two equations representing the linear relationships between surface area and the corresponding maximum force for soil and hydrogel are displayed in Figure 32. The slope of each linear equation indicates the rate of change of maximum force with respect to surface area. The decision to constrain the linear equations to pass through the origin (0, 0) is based on the idea that if there is no root structure (surface area is 0), there is no contact between the roots and the substrate (soil or hydrogel), and therefore no force can be generated. The higher slope for soil (0.0599) compared to hydrogel (0.0347) indicates that an increase in surface area has a greater impact on the pullout force in soil than in hydrogel.

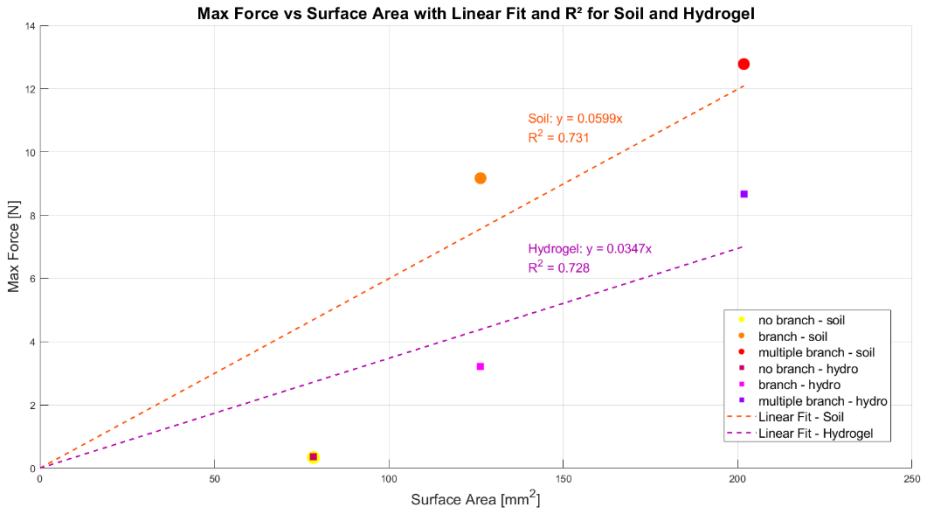

Figure 32: Plot of maximum pullout force versus surface area for the mung bean models in both soil and hydrogel, including the linear fitting curves and coefficients of determination for each substrate.

Contour plots

Figure 33 presents contour plots for stress, strain, and vertical deformation within the root-substrate system for the branch configuration at the 4s time step. The no-branch configuration was excluded due to a lack of significant stress, strain, or vertical displacement in the surrounding medium, making further analysis unnecessary. The multiple-branch configuration was also omitted, as its sectional view appeared almost identical to the branch configuration; the additional branches were obscured by the substrate, adding no further visual insight. The behavior observed in the branch configuration closely mirrors that of the barley configurations. In the mung bean models, stress is concentrated at the junctions between the secondary branches and the taproot, as well as in areas where the branches exert pressure on the soil while displacing. Strain is similarly concentrated in regions where the root system pushes against the substrate during pullout. As for vertical displacement, the soil shows localized movement and breakage around the root structure as it is pulled upward, whereas in hydrogel, deformation is more uniform, with displacement distributed evenly throughout the medium rather than concentrated near the roots.

MODEL 2, test label: branch

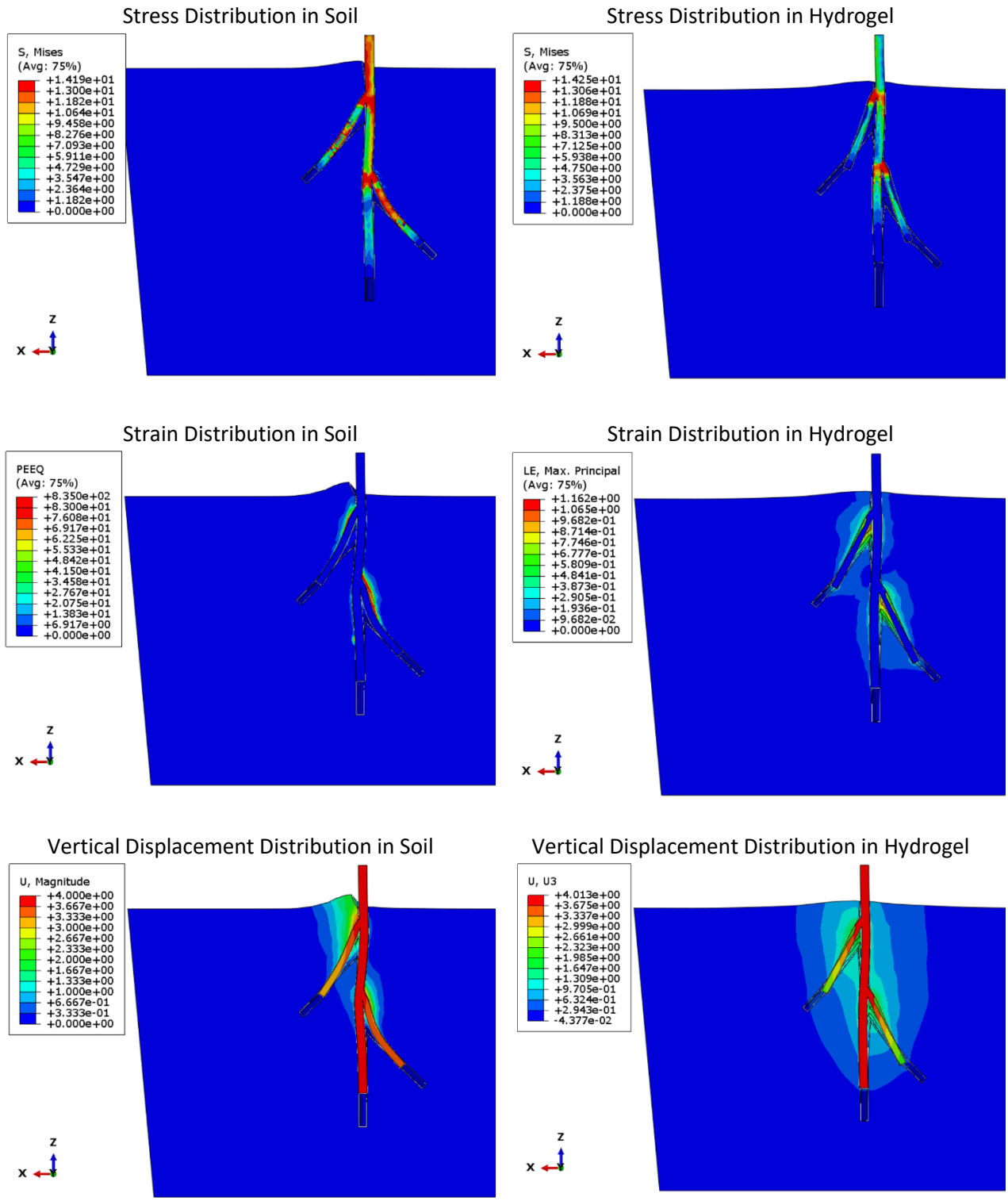

Figure 33: Snapshot of stress distribution, strain distribution and vertical displacement in soil and hydrogel for mung bean model 2.

Energy History Output

In Figure 34, the energy history output is analyzed for a specific model: mung bean model 3 in soil. This model was chosen as it achieved the highest maximum pullout force compared to all other mung bean models tested across both substrates, making it the most significant case for analysis. During the simulation, internal energy and external work shows a consistent increase with time while kinetic energy and artificial strain energy remain at zero all throughout. The system's total energy fluctuates between 0 and 0.3 N*mm.

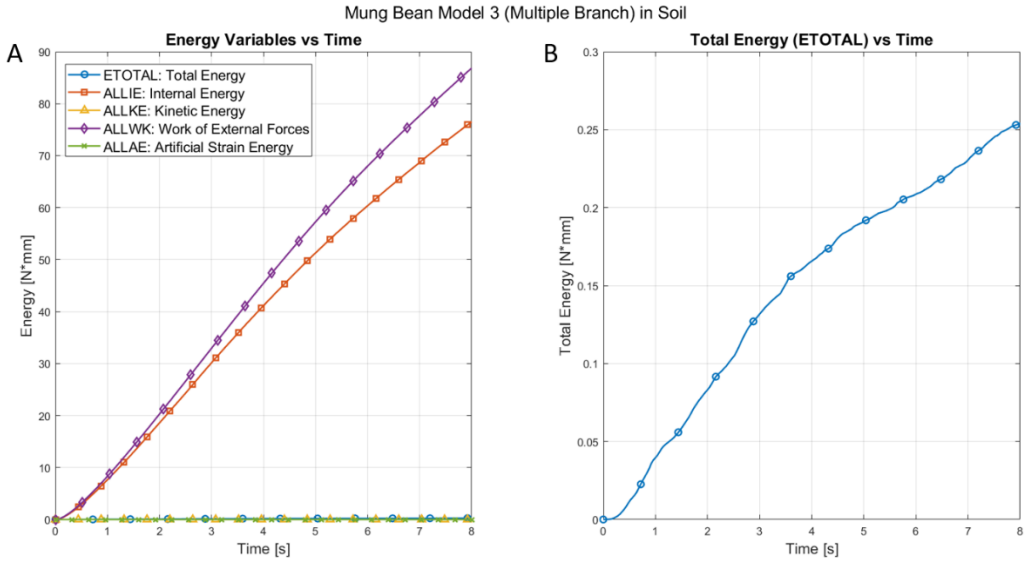

Figure 34: A) Plot showing various energy outputs obtained through ABAQUS over the simulation time step, including total energy, internal energy, kinetic energy, artificial strain energy, and the work of external forces. B) Displays only the total energy plot versus time. Both plots are based on simulations of mung bean model 3 in soil.

3.4.3 Mesh Convergence Test Results

The results from the mesh convergence test are presented in Figure 36. Part A shows the force-displacement curves from the simulation of barley model 1 in soil, illustrating the effect of different mesh densities (number of elements in the root model) on the simulation results. Part B displays the maximum force obtained from each simulation plotted against the corresponding number of elements. The maximum force varies from 4.77 N for the finest mesh to 5.15 N for the coarsest mesh, resulting in a difference of 0.38 N, which represents approximately an 8% variation relative to the maximum value. The number of elements ranges from 601,398 for the finest mesh to 49,276 for the coarsest mesh, a difference of 552,122 elements.

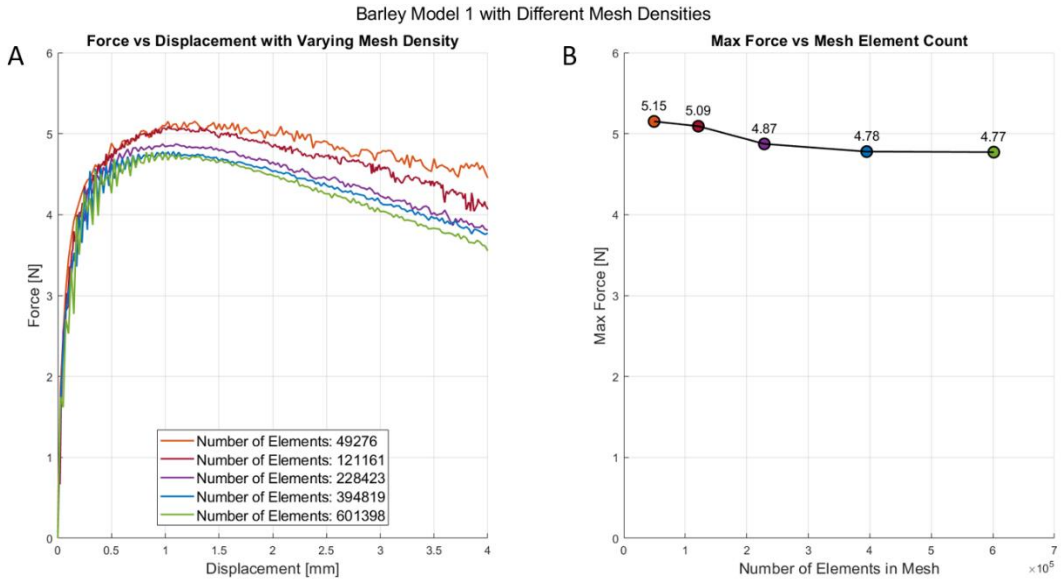

Figure 35: A) Force-displacement curves from the simulation of barley model 1 in soil, showing the effect of different mesh densities (number of elements in the root model) on the simulation results. B) Maximum force obtained for each simulation plotted against the corresponding number of elements.

3.5 Results on Root Growth in Hydrogel

This section presents the outcomes of testing three protocol versions for cultivating root growth in a hydrogel substrate. Table 15 summarizes the results obtained from each protocol version, which included varying concentrations of $CaCO_3$ and GDL to assess their effect on root growth. In version 1, both mung bean and barley seeds were planted, with 25 seeds of each species embedded in hydrogel batches at different $CaCO_3$ and GDL concentrations (50 mM, 80 mM, 100 mM, and 150 mM). Out of the 50 samples, only 2 mung bean seeds showed root growth, corresponding to a success rate of 4%. These two successful samples were planted at concentrations of 50 mM and 80 mM and are shown in Figure 36a. Version 2 had 6 barley seeds planted in hydrogel at a consistent $CaCO_3$ and GDL concentration of 50 mM. In this version, 2 seeds successfully grew, achieving a higher success rate of around 33%, with one shown in Figure 36b. In the last version, 23 seeds of each type was planted in hydrogel at concentrations of 50 mM, 80 mM, and 100 mM. However, this protocol resulted in a 0% growth rate, as none of the seeds developed roots. Table 23 and Figure 55 in the appendices provide detailed results on fungal contamination across the different protocol versions, along with corresponding images. These findings will not be discussed further, as they fall outside the scope of the primary research question.

Table 15: Summary of results for different protocol versions on root growth in hydrogel.

Parameter	Protocol Version 1	Protocol Version 2	Protocol Version 3
Seed planted	25 Mung bean + 25 Barley	6 Barley	23 Mung bean 23 Barley
Type of seed that grew	Mung	Barley	None
Amount of seed that grew	2 out of 50	2 out of 6	0 out of 46
Sodium alginate concentration	2.5%	2.5%	2.5%
NPK dosage	Max dosage: 2.00 g/L	Max dosage: 2.00 g/L	Max dosage: 2.00 g/L
$CaCO_3$ + GDL Concentrations tested	50 mM (10 samples) 80 mM (10 samples) 100 mM (10 samples) 150 mM (10 samples)	50 mM (6 samples)	50 mM (18 samples) 80 mM (18 samples) 100 mM (10 samples)
$CaCO_3$ + GDL Successful concentration	50 mM + 80 mM	50 mM	None
Growth success rate	4%	~33%	0%

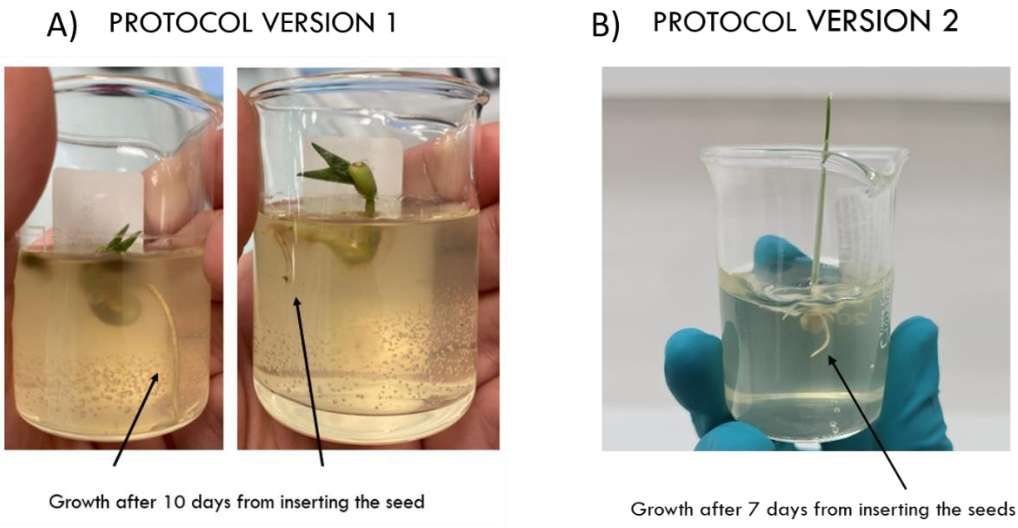

Figure 36: Images of successful growth in hydrogel: A) mung bean seed, B) barley seed.

4. Discussion

4.1 Discussion regarding Plant Growth Measurement and Root Observation

4.1.1 Plant Growth Measurement

The relationship between stem height and days of growth across both species, show in Figure 12, highlights a consistent trend of increasing height with time, offering valuable insights into plant growth behavior. The logistic model captures this trend effectively, modeling an initial phase of rapid growth that gradually slows as the plant matures and eventually reaches a saturation point. This is aligns with existing literature, where biological growth, whether in plants or animals, is described using a sigmoidal growth model [73]. This model reflects how biological growth is influenced by multiple factors, such as hormones, mineral nutrients, and ecological processes, which result in an asymmetric growth rate curve [74, 75].

4.1.2 Root Observation

Although the roots may have been damaged during extraction and cleaning, and smaller secondary branches or terminal branches of primary roots might have detached in the process, this procedure still provided valuable insights into root development over time. Furthermore, the observations made in Section 3.1 align with findings from the literature. Mung beans are characterized by a primary root with a single dominant axis, capable of developing numerous lateral roots as the plant matures, also shown in Figure 14 [32]. In contrast, barley exhibits a fibrous root system, which lacks a dominant primary root. Barley seedlings develop seminal roots early, immediately following germination, as seen in Figure 13, with adventitious roots forming later during plant growth [33].

Another key observation is the relationship between stem growth and root development. As the stem grows taller, the root system expands as well. Although the exact extent of this relationship is not fully quantified, Figure 13 and Figure 14 clearly show that both stem and root growth occur simultaneously, with each influencing the other. This aligns with literature findings, which show that growth rates and biomass distribution between roots and shoot (including stems and leaves) are closely linked in a complex and dynamic relationship [74]. While shoot and roots have distinct forms and functions, they work together to maintain balance through resource exchange and growth regulation. Carbohydrates are translocated from shoot to roots, while water and nutrients move from roots to shoot, ensuring each organ receives the resources needed for optimal growth. This coordination is regulated by phytohormones like cytokinins and auxins, which act as messengers between the two parts, influencing their reciprocal development and activity [76]. Overall, as one part of the plant grows, the other tends to grow as well, due to their interdependent relationship [77].

4.2 Discussion regarding Pullout Results

The results of the pull-out tests, shown in Figure 15 and Figure 17, are presented with respect to stem height rather than days of growth. This approach was chosen to provide a broader distribution of data points across the x-axis, offering a wider range of values for analysis. Stem height allows for a more continuous scale, enabling a clearer visualization of how maximum force and work vary with plant growth, as opposed to having clustered data points at only a few distinct days of growth. However, this choice also presents certain limitations. The lack of multiple data points per each height point limits the ability to calculate reliable averages or standard deviations, thereby constraining the development of a statistically robust trend line that accurately represents the overall data pattern.

The results in Figure 15 and Figure 17 show greater variability in barley compared to mung bean, both in terms of the coefficient of determination and the visual spread of data points around the linear fit. Barley exhibits a lower R^2 and more scattered points, likely due to its complex root system, which includes both seminal and adventitious roots. These roots grow at varying rates and in unpredictable patterns, contributing to significant variability, as seen in the CT scans in Figure 20. The timing of adventitious root formation and their distribution within the substrate can lead to uneven anchorage strength. In contrast, mung beans have a simpler root structure, consisting of a main taproot with secondary branches, which may lead to a more consistent and predictable root system. This could explain the more consistent pullout forces observed in their tests.

Despite variability in the data, the maximum force and work done up to that force showed an overall positive trend with increasing stem height, Figure 15 and Figure 17. This suggests that as stem height, and thus root development, increases, the force and work needed to extract the plant from the soil also rises. The maximum pullout force is a direct measure of the peak resistance encountered by the root system before it detaches from the soil, making it an indicator of the root-soil bond strength. A higher maximum force implies that the roots are more strongly anchored, requiring greater effort to overcome the root-soil adhesion and cohesion forces. Total work done up to the maximum force represents the cumulative energy required to reach this peak resistance. Unlike maximum force, which captures only the highest resistance point, work accounts for the entire displacement process leading up to this point. This measure reflects the ability of the root system to absorb energy. High work values suggest that the root-soil interface can endure greater displacement under load.

Based on the results from the root extraction in Section 3.1, as shown in Figure 13 and Figure 14, it was observed that as stem height increased, the roots showed corresponding development. For both barley and mung bean, this growth was characterized by increased root length and diameter. Additionally, the roots displayed greater tortuosity and the development of secondary branches, with the number of branches increasing over time and as stem height grew. These observations are important because factors such as root length, diameter, tortuosity, and branching are known to impact pull-out force. While quantifying each parameter's exact contribution to pull-out force is challenging, it is generally established that they have a positive influence. Collectively, these factors contribute to a greater resistance against extraction.

Literature shows that root anchorage capability increases with root length, but only up to a critical length. Beyond this point, further length does not enhance anchorage, as the top of the root may break before stress is transferred to the lower regions [78]. Additionally, longer roots have a greater potential to generate friction along the root-soil interface due to the increased points of contact with the soil [79, 80]. Root diameter plays a significant role in root pull-out resistance. Studies have shown that both maximum pull-out force and displacement at maximum force increase non-linearly with root diameter [36, 81]. This effect is attributed to the structural rigidity and higher bending stiffness of thicker roots compared to finer roots. Tortuous roots, by nature, become more adaptable and resilient to various stresses without fracturing [80, 82]. The irregular, winding path of tortuous roots also increase frictional resistance with the soil, thereby increasing normal

stress at the root-soil interface due to the larger surface area in contact with the soil [36, 37]. Essentially, the more the root weaves and bends, the greater the force required to pull it out. Branching further enhances pull-out resistance by increasing both the bearing and surface area of the root in contact with the soil. Branches expand the root system's overall exposure to the soil, increasing surface contact and frictional resistance at the root-soil interface [37]. Additionally, branches contribute to the root's axial resistance and engage more root material with the soil, significantly boosting the root's resistance to extraction [31, 36, 80]. Overall, the results presented in Figure 15 and Figure 17 align with existing literature, as both maximum force and work increased with greater root development, including increases in root length, diameter, tortuosity, and branching.

The different failure mechanisms observed in Section 3.2, for both barley and mung bean can also be explained by individual root geometry parameters or characteristics. As shown in Figure 16b, for barley sample B3 and Figure 18b for mung bean samples M1 and M2, some seeds exhibited a sharp rise in force with displacement until reaching maximum force, followed by an immediate drop to zero. This behavior likely reflects the early developmental stage of these seeds, which, based on the root extraction analysis in Section 3.1, suggests a lack of secondary branches. This observation is further supported by the photograph of sample M1 in Figure 18b, where the intact taproot remaining after the pullout test shows no signs of secondary branches, with only the broken taproot visible. Literature supports that branching impacts root failure mechanisms, as roots without branches tend to fail rapidly in tension, pulling out of the soil with minimal resistance once they reach maximum pull-out resistance [31].

In contrast, tests shown in Figure 16b, samples B5 and B10 for barley, and Figure 18b, samples M7 and M8 for mung bean, displayed a different failure pattern. Here, the force initially increased linearly with displacement, peaked, then dropped slightly before rising again, resulting in multiple fluctuations throughout the test. These seeds likely had developed branches, as indicated by their increased stem length. This is further validated by the photograph of sample M7 in Figure 18b for mung bean and samples B5 and B10 in Figure 16b for barley. In the mung bean sample, parts of the intact taproot and secondary branches are visible after the pullout test, while in the barley samples, the intact seminal roots are visible, showing that the roots fractured at varying root lengths. This behavior aligns with literature findings, where roots with multiple branches typically fail in stages, as each branch gradually breaks under increasing applied force. This gradual failure produces step-like peaks, reflecting the progressive breaking of roots with partial failures and yield points in the root structure until final failure occurs [31, 83].

In Figure 16b, test B11 is also included, representing the barley root with the highest stem length. This suggests that it was fully developed, likely with more lateral branches than any other barley sample tested. Based on previous explanations, one would expect a progressive failure mechanism with step-like fluctuations, as lateral branches and increased root development typically result in gradual, multi-stage pull-out failure. However, in this case, the root displays a rapid increase in force until it reaches a peak, followed by an immediate drop to zero. A plausible explanation for this behavior is that when a root is highly developed and firmly anchored in the soil, the force required to overcome soil resistance may exceed the structural integrity of the stem-root connection itself. Instead of a gradual release from the soil, the root may break at the base of the stem, resulting in an abrupt drop in force and leaving the root system still embedded in the soil. This is validated by the photograph of sample B11 in Figure 16b, taken after the pullout test, which shows breakage at the stem-root connection.

The final observations relate to Figure 19, which illustrates the maximum force as a function of stem height for both barley and mung bean samples. Barley roots demonstrate greater mechanical resistance than mung bean roots, as evidenced by their higher range of maximum forces even at comparable or lower stem heights. These differences can be attributed to the distinct root architectures characteristic of each species. As shown in the literature, pull-out force is most effectively resisted by a multitude of thin, fibrous roots, a typical

structure of barley, which provides a large surface area for rapidly transferring tension to the soil, unlike a single, wide taproot, which is the typical structure of mung bean [41, 84]. In fibrous root systems, numerous small roots increase the soil's cohesive strength by binding soil particles together, resulting in a stronger structure that is more resistant to breakage [14]. In contrast, taprooted systems rely mainly on a single large, deep root to anchor the plant. Stress is primarily distributed along this main vertical root, potentially providing less resistance to lateral forces compared to fibrous systems [14]. Consequently, for a single thick root to provide the same anchorage as numerous thin roots, it would need to be exceptionally long. However, beyond a certain critical length, this root may break and fail to resist pull-out [84].

4.3 Discussion regarding CT Scan Results

One significant challenge in accurately post-processing CT scans of root systems within soil is the similar density between soil particles and root tissue, which often leads to overlapping grayscale values in the images and complicates segmentation [85]. This problem is further complicated by the composition of universal potting soil, which typically contains aged bark. These bark fragments resemble root structures in grayscale imaging, creating additional difficulties as segmentation algorithms may mistakenly classify bark particles as root segments [86]. The lack of natural contrast at the boundaries between roots and soil often causes these structures to blend together, making it challenging to isolate and accurately identify root morphology. While high-resolution imaging can improve the distinction of finer root structures from soil particles, it also introduces noise and significantly increases computational demands, requiring a trade-off between image clarity and processing efficiency [87]. Current segmentation algorithms often struggle to achieve the fine resolution needed to isolate smaller roots within dense soil matrices, a particular challenge given the small size of the roots in these CT scans. This limitation makes it difficult to produce highly detailed and visually accurate post-processed images. Techniques such as contrast enhancement or the selective use of contrast agents can improve visibility and help mitigate these challenges. However, they require careful application to avoid altering the natural root structure [88].

Another characteristic aspect of CT scan analysis is the high degree of variability across scans, as seen in Figure 20 and Figure 22. Each scan captures a unique snapshot of a complex natural system, where both soil structure and root architecture vary greatly. Variations in soil particle size, compaction, moisture, and nutrient levels shape root growth, causing roots to adapt, navigate obstacles, and respond to environmental conditions [89]. This adaptability leads to distinct and often unpredictable growth patterns, resulting in significant differences even between scans of similar-aged samples. This variability reflects the dynamic nature of root-soil interactions and highlights the challenge of identifying a "standard" growth pattern within such a system.

Despite the variability of the scans, several common parameters within the root systems were identified. For barley roots, these parameters included the number of seminal branches, their diameter, and length. For mung bean roots, data was gathered on the taproot's diameter and length, as well as the diameter and length of secondary branches. This information facilitated the creation of realistic 3D models of both root systems for FEM simulations, shown in Figure 6 and Figure 8. Furthermore, the parameters chosen for the FEM simulation focused on characteristics with the most variation across scans. For barley roots, vertical and radial branching angles, along with tortuosity, were identified as key variables. The vertical branching angle was set to three values: 15°, inspired by scan A (Figure 20) and representing the lower end of the observed range; 45°, an average angle seen across scans; and 80°, also inspired by scan A (Figure 20) and representing the upper end of the observed range. For the radial branching angle, three different arrangements were created. In the first, based on scan A (Figure 20), roots were grouped into two clusters of three, with an angle of 120° between the clusters. The second arrangement, inspired by scan D (Figure 20), organized roots into three pairs, each closely spaced, with gaps of 80° between pairs. The final arrangement used a uniform spacing of 60° between roots. Tortuosity was also included to mimic the natural root curvature observed in the scans (Figure 20). For mung bean roots, the number of branches at each branching point was selected based on CT scan findings in Figure 22, as this parameter showed the most variability.

4.4 Discussion regarding FEM Simulation Results

In this section, the results of the FEM simulations are analyzed to examine how variations in model architecture and substrate affect pullout resistance and substrate response. The discussion begins with the numerical results for the barley FEM models, also presented in Figure 23 and Table 13.

In soil, the highest maximum force was achieved with a branching angle of 45°, closely followed by the 80° angle, while the 15° angle demonstrated significantly lower pullout strength compared to both, reaching approximately 56% of the force produced by the 45° angle. The difference in pullout strength from the 15° to the 45° angle can be explained by the following mechanism. With a small vertical branching angle, such as 15°, the force applied behaves almost like an axial pull. Because the root is nearly vertical, it can slide out of the soil along the same path it originally created, with minimal lateral resistance. This lack of sufficient lateral friction or resistance allows the root to be pulled out with relative ease. This mechanism is further supported by the snapshot of vertical soil displacement in Figure 26, which shows nearly zero displacement, indicating minimal soil engagement during the pullout of the roots. As the branching angle increases to 45°, the root encounters a larger volume of soil above it, preventing it from sliding out vertically with ease. To be pulled upward, the root must first bend and adjust its position, gradually aligning into a more vertical orientation. This repositioning requires the root to mobilize more soil in the process, as shown in Figure 24. The larger volume of mobilized soil increases the contact area between the root and the surrounding soil, creating greater interaction and resistance. This amplified soil-root engagement ultimately requires more force to overcome, resulting in increased pullout resistance.

Once the vertical branching angle exceeds 45°, reaching values such as 80°, this mechanism no longer applies, meaning that the pullout force does not continue to increase with the branching angle. Instead, the pullout process becomes governed by the shearing and fracturing of the soil, which can be directly attributed to and influenced by its material properties. In all simulations done with soil as a medium, the vertical displacement and strain distribution are localized around the root as it is pulled upward, as shown in Figure 24 though Figure 29. The soil was modeled as an elastic-perfectly plastic material, which means it deforms elastically up to a certain limit before permanently yielding. As the root begins to pull out, it creates a localized stress distribution at the points of contact with the soil. This causes soil deformation to concentrate near the root, where resistance builds until the soil reaches its yield point. At this point, the soil begins to deform permanently around the root, “breaking” or shearing along stress lines. This reduction in resistance allows the root to move upward more easily as the soil begins to displace around it. This behavior explains why, in soil, the 80° angle configuration achieves a lower pullout force. At this angle, the root must bend significantly more than the 45° configuration to begin sliding out, putting extra localized stress on the soil. This increased stress causes the soil to reach its yield point more quickly, leading it to “break” sooner. Once the soil has fracture, the root, with its more horizontal orientation and smaller volume of soil above, can more easily move upward.

In hydrogel, similar results were observed for the 15° and 45° angle models, with the 45° angle achieving a higher pullout force. However, in the simulation, the 80° angle in hydrogel showed an even greater pullout force than the 45°. This difference in pullout behavior between soil and hydrogel can be attributed to their distinct material properties. Unlike soil, hydrogel was modeled as a hyperelastic, incompressible material. This means that, instead of breaking or yielding under stress, the hydrogel stretches uniformly around the root, as shown in Figure 24 though Figure 29. As a result, stress is distributed more evenly, without forming concentrated zones of deformation. This allows hydrogel to resist pullout forces without fracturing, creating a consistent and uniform deformation around the root. Because hydrogel does not yield or fracture, the only way to extract the root is through steady pullout force. As the vertical branching angle increases so does the pullout force is required to displace the root. The nearly horizontal root orientation at 80° must overcome

more bending and stretching in the surrounding hydrogel to begin moving, which increases the pullout force needed to achieve displacement.

Beyond this specific case, a broader comparison across all models reveals a consistent trend: maximum pullout forces are generally higher in soil than in hydrogel, a pattern that holds for all tested models, including those for mung bean (Figure 23 and Figure 31). Conversely, the displacement at maximum force is always greater in hydrogel than in soil. This difference in pullout behavior can be attributed to the distinct mechanical properties of soil and hydrogel. Soil's rigidity concentrates resistance locally around the root, causing the pullout force to increase rapidly until the yield point is reached and the material fractures. In contrast, hydrogel's elasticity allows it to stretch under load without yielding, providing more sustained resistance as the root pulls through and resulting in a higher displacement at maximum force. Hydrogel's uniform, gradual resistance highlights its contrasting behavior to soil, where force concentrates and yields more quickly, leading to lower displacement and higher peak force.

Unlike the vertical branching angle, the radial branching angle had a negligible impact on maximum pullout force in both soil and hydrogel across all barley configurations. In contrast, root tortuosity nearly doubled the pullout force compared to the straight root model in soil. This increase occurs because tortuosity adds flexibility to the root through its twisted growth path, increasing its elasticity and allowing it to withstand various stresses without breaking [80, 82]. Additionally, the irregular path of a tortuous root increases frictional resistance with the soil, raising normal stress at the root-soil interface due to the larger contact area with the soil [36, 37]. In hydrogel, tortuosity also led to a slight increase in pullout force, approximately 12.5%, though this effect was far less pronounced than in soil. This difference arises because the flexible nature of hydrogel allows it to conform around tortuous roots without generating significant localized friction or resistance.

Following the barley models, the mung bean models were examined to understand how an increase in branches per branching point would influence the root-medium system in both soil and hydrogel. In both substrates, an increase in the number of branches per branching point led to a corresponding increase in the root's surface area in contact with the substrate. This, in turn, resulted in a higher maximum pullout force, as shown in Figure 31. By increasing the surface area, the root engages more of the substrate during pullout, increasing frictional resistance [90], distributing force across multiple points, and ultimately reducing stress concentrations [91]. Furthermore, the added branches increase structural complexity of the root system, creating a more stable root network that resists deformation and straight-line movement [12]. Together, these factors lead to greater pullout resistance as the number of branches and the surface area increase. The behavior of the substrate remains consistent despite the differences in root architecture between mung bean and barley. From Figure 32, which plots the maximum pullout force against the surface area, it can be seen that soil has a higher slope (0.0599) compared to hydrogel (0.0347). This suggests that an increase in surface area has a greater impact on pullout force in soil than in hydrogel, likely due to soil's higher rigidity and friction. This is further supported by the contour plot in Figure 33, where hydrogel shows more uniform stretching, while soil, due to its rigidity, concentrates deformation locally around the root structure.

Shifting focus from the analysis of maximum pullout forces, the next section examines stress distribution within the root systems. Stress concentrations are important as they weaken areas and often become the initial points of material failure under load. Contour plots in Section 3.4 (Figure 24 though Figure 29 and Figure 33) reveal stress concentrations at critical points for both root systems tested, barley and mung bean. These include the junctions between the seminal root and seed (in barley), between secondary branches and the taproot (in mung bean), and areas where the root actively presses against the substrate during pullout (in both). The stress concentration at these junctions arises from the change in cross-sectional geometry and load transfer between the seed or taproot, modeled as a larger cylinder, and the seminal or secondary root,

modeled as a smaller cylinder. This difference in size creates a geometrical discontinuity that leads to stress buildup and reduced load-bearing area, resulting in the highest stress concentrations at these points.

On the other hand, stress concentration at the root-medium interface arises as the root exerts force to overcome the resistance of the surrounding substrate (soil or hydrogel) during pullout. The areas where the root is in direct contact with the substrate become focal points for applied force, as the root "pushes" against the soil or hydrogel to displace it. This interaction creates localized zones of higher stress which induce a corresponding strain concentration within the medium, as it deforms in response to the root's applied pressure. In soil, which is modeled as an elastic-perfectly plastic material, plastic deformation is concentrated around the areas where the root is in contact with the soil. Beyond these contact points, soil deformation quickly decreases as the distance from the root increases, keeping strain largely confined to the immediate contact zones. In contrast, hydrogel, modeled as a hyperelastic material, deforms elastically and distributes strain more evenly throughout the substrate. Due to its elastic properties, strain in hydrogel extends over a larger area, reaching regions farther from the initial contact points. This results in a more uniform deformation pattern around the root.

These findings provide design strategies that can be applied to strengthen engineered hard-soft interfaces. However, before moving forward, an initial observation is necessary to clarify some important consideration. Since not all characteristics that increase interface strength in soil have the same effect in hydrogel, it becomes evident that substrates with varying stiffness and material properties will react differently to identical root configurations. This highlights that features strengthening an interface in one material, like soil, may not achieve the same result in another, such as hydrogel. Therefore, when designing bioinspired interfaces for diverse substrate, it is essential to consider the unique properties of each substrate, as certain characteristics may not directly translate across materials.

Before exploring the optimal root model for maximizing pullout force in both substrates, it's important to address a discrepancy observed between the experimental pullout tests and the FEM simulation results. In the pullout tests, barley seeds consistently demonstrated greater pullout force than mung bean seeds, as shown in Figure 19 in Section 3.4. This finding aligns with existing literature, which suggests that fibrous root systems, like those of barley, generally withstand pullout forces better than taproot systems, such as those in mung beans. However, the FEM simulations present a different outcome. As shown in the plots in Figure 23 and Figure 31, the mung bean configuration with multiple branching achieved the highest pullout force in both substrates, which contrasts with the findings from the experimental results. One possible reason for this difference could be the structural variations in the simulation models. In the pullout tests, most barley roots developed adventitious (secondary) branches, while the FEM model for barley included only seminal (primary) roots. As seen in the mung bean simulation, adding secondary branches increased the pullout force by 30 times or more. This suggests that if adventitious branches were also incorporated into the barley FEM models, its simulated pullout force would likely surpass that of the mung bean models.

With these considerations in mind, and based on insights from pullout tests and FEM simulations, we can propose an optimal root structure for maximizing interface strength in different substrates. These structures could inspire and inform the design of engineered hard-soft interfaces, guiding the integration of features like branching patterns or structural flexibility to improve strength in both rigid and elastic substrates. Based on the results, a fibrous root structure incorporating both seminal and adventitious branches could achieve the highest interface strength in materials like soil, which have high rigidity and provide localized resistance. In contrast, in materials like hydrogel, which are highly elastic and tend to distribute strain gradually, a taproot structure with multiple secondary branches would likely achieve the strongest interface. Both optimal root structures can be further refined by selectively incorporating features that have been shown to increase pullout force and interface strength within each specific substrate. This approach tailors root structure to improve interface strength based on the substrate material's properties.

For the fibrous root system, the length and diameter of both adventitious and seminal branches should be maximized within an effective range to enhance anchoring capabilities and resistance to axial forces. The vertical branching angle between the seminal roots and the vertical axis should be 45°, with the seminal branches evenly spaced along the main root and a consistent radial branching angle to distribute stresses effectively across the structure. Closely spaced or clustered roots can create strain concentrations in the substrate during pullout, leading to excessive localized deformation. This strain concentration increases the risk of material failure or structural breakdown in the substrate surrounding the roots, thereby weakening interface strength. The seminal branches should also incorporate a degree of tortuosity, as this feature significantly increase interface strength. For the adventitious roots, however, these characteristics have not been explored in this study and could be considered for future implementation. Lastly, a critical stress concentration point in the system is likely to occur at the junction between the seminal and adventitious roots, which may be the initial point of failure in the root structure. To mitigate this stress concentration, a simple and effective solution is to introduce a fillet (curved transition) or a gradual taper at this junction. This approach facilitates load transfer between the seminal and adventitious roots, reducing abrupt geometry changes and distributing forces more evenly across a larger area.

For the taproot system, the length and diameter of the taproot and secondary branches should similarly be maximized within an effective range. Secondary branches should be evenly spaced along the main root with a consistent radial branching angle, and a fillet or gradual taper should be introduced at the junction between the taproot and secondary branches, as in the fibrous root system. All these characteristics should be implemented for the same reasons outlined for the fibrous root system. Finally, for optimal interface strength, the vertical branching angle between the taproot and secondary branches should be nearly horizontal, as this orientation requires greater pullout force to displace the root due to increased bending and stretching in the surrounding hydrogel.

Figure 37 shows a rendering of the optimized root structures designed for embedding in soil or soil-like materials (A) and hydrogel or hydrogel-like materials (B), including a zoomed-in view of the junction between seminal and adventitious roots, as well as the junction between the taproot and secondary roots. This visual provides a general idea of the structure's appearance but does not represent exact dimensions.

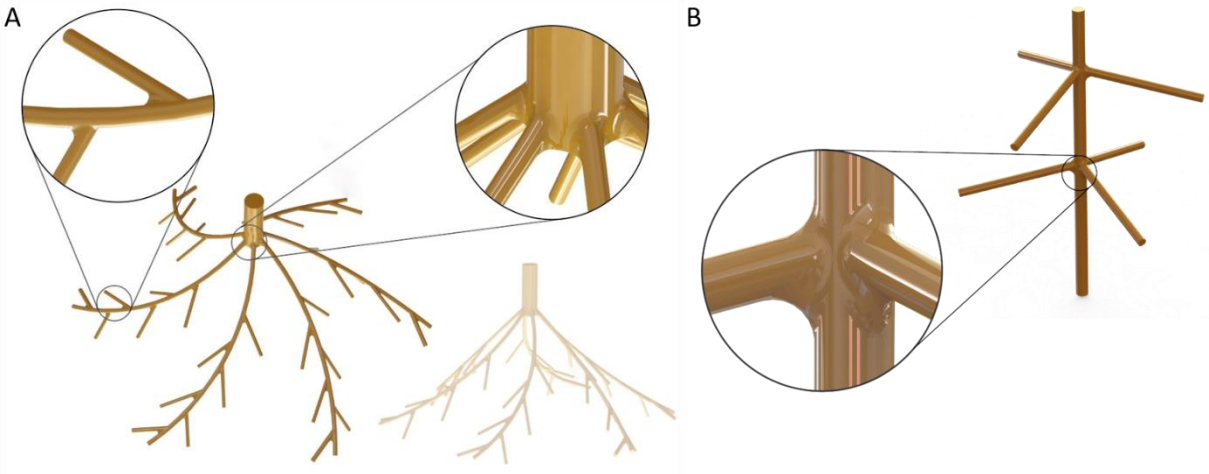

Figure 37: Rendering of the optimized fibrous root system for soil or soil-like materials (A) and the optimized taproot system for hydrogel or hydrogel-like materials (B).

The FEM model was further validated through energy history output results and mesh convergence analysis. The energy history output results confirm that the model's physical behavior, such as energy conservation and distribution, aligns with expected real-world behavior. Meanwhile, mesh convergence analysis ensures that the FEM model's results are not influenced by mesh size and determines whether the chosen mesh provides satisfactory results without excessive computational expense.

The results presented in Figure 30 and Figure 34 provide valuable insights into the energy dynamics during the pullout simulation, in soil, for barley model 6 and mung bean model 3, respectively. The internal energy (ALLIE) steadily increases for both models, suggesting realistic energy absorption by the substrate and root, thus validating the materials' deformation. The kinetic energy (ALLKE) remains at zero throughout both simulations, which aligns with the expectations for a quasi-static process, where motion-induced energy is minimal. The artificial strain energy (ALLAE) also stays at zero, indicating no significant numerical artifacts and confirming that the model behaves without unrealistic deformations. External work (ALLWK) increases consistently with time for both cases, confirming that the work done by external forces aligns with the expected force-displacement behavior at the root-soil interface. The total energy (ETOTAL) of the system varies between 0 and 0.13 N*mm for the barley model and from 0 to 0.3 N*mm for the mung bean model, both indicating a stable energy balance throughout the simulation. These minor variations suggest that the simulation accurately accounts for energy inputs and dissipations. Overall, the energy output analysis confirms that the model behaves realistically, with energy components balanced within expected limits, providing confidence in the simulation's results.

The mesh convergence test shown in Figure 35 highlights the impact of mesh density on the simulation outcomes for barley model 1 in soil. The force-displacement curves for different mesh densities exhibit similar trends, indicating that the general behavior of the system is captured consistently across the simulations. This consistency suggests that even the coarser meshes approximate the system's behavior with reasonable accuracy. In terms of maximum force, values vary between 5.15 N, for the coarsest mesh with 49,276 elements, and 4.77 N, for the finest mesh with 601,398 elements, corresponding to a variation of 0.38 N, or about 8% of the maximum force. This difference can be attributed to insufficient resolution at the root-substrate interface with the coarser mesh. However, the overall variation is small, and the results are not significantly impacted by mesh density. Based on this analysis, the mesh with 121,161 elements, used in all simulations, was validated. The variation in maximum force between this mesh and the finest one was 0.31 N, approximately 6% of the maximum force, indicating sufficient accuracy. Additionally, this mesh resolution offered a significant reduction in computational load compared to the finest mesh. Therefore, it was confirmed to be the optimal balance between computational efficiency and result accuracy, making it the most practical choice for the simulations.

4.5 Discussion and Observations on Root Growth in Hydrogel

Before proceeding, a brief comment on the results is necessary. The results analyzed arise from different protocols, yet they remain comparable since the primary protocol differences relate to sterilization methods rather than any factor that would significantly impact root growth. Complete sterilization and the elimination of fungal contamination were achieved through careful sterilization of seeds, hydrogel components, and equipment, along with the incorporation of antifungal agents into the hydrogel and maintenance of a clean, controlled environment.

In addition to maintaining sterility, the preparation of the hydrogel medium itself plays a crucial role in supporting root growth. Calcium carbonate ($CaCO_3$) and glucono delta-lactone (GDL) are essential in hydrogel formulation, as they regulate pH and crosslinking density, both of which are critical for creating an environment favorable to seed germination and root growth. $CaCO_3$ supplies calcium ions, while GDL gradually reduces pH; together, they control the hydrogel's crosslinking density, shaping its mechanical strength and ability to retain nutrients [20].

The results in section 3.5 highlight that mung bean and barley seeds achieved the most successful growth at $CaCO_3$ and GDL concentrations of 50 and 80 mM. These concentrations likely created an optimal balance of hydrogel porosity, nutrient retention, and pH levels. At these levels, the hydrogel provided sufficient porosity to support root penetration and air exchange, while also retaining adequate moisture and nutrients to promote seed growth. In contrast, higher concentrations of $CaCO_3$ and GDL were less effective, likely resulting in an overly dense hydrogel structure that inhibited root growth and nutrient uptake. This initial study aimed to see if barley and mung seeds could grow directly in hydrogel, exploring whether hydrogel could be used as a substitute for soil in some controlled settings. Early results show that while hydrogel can support initial stages of plant growth, this is just a first step, and more work is needed before it can be used as a reliable growing substrate on its own.

Conclusion

This research provides significant insights into the mechanical resilience of natural hard-soft interfaces, particularly the root-soil interface, and explores the potential for bioinspired engineered interfaces. While artificial systems face challenges when joining materials with different mechanical properties, natural hard-soft interfaces seamlessly integrate without these issues [1, 4]. The goal of this study was to identify the driving mechanisms, such as root geometric parameters, 3D root architecture, and variations in substrate stiffness and material properties, within the root-soil interface that influence interface strength and can inspire the design of bioinspired engineered hard-soft interfaces. The study examined root geometry and architecture characteristics, including length, diameter, tortuosity, branching patterns, and both vertical and radial branching angles, across two substrates: soil and hydrogel. Two types of seeds, barley and mung bean, were selected for their distinct root structures. Barley displayed a fibrous root system with six seminal branches and additional adventitious branches growing from them, while mung bean featured a main taproot with secondary branches extending from it. The root systems were analyzed over a growth period of up to 15 days.

Plant growth measurements revealed a consistent increase in stem height over time, which is effectively captured by the logistic growth model. This model demonstrates an initial phase of rapid growth that gradually slows as the plant matures, eventually reaching a saturation point. This growth pattern aligns with biological growth, which typically follows a sigmoidal curve influenced by factors such as hormones, nutrients, and ecological processes.

Laboratory pullout tests and root extraction procedures for barley and mung bean seeds in soil suggested that increased root length, diameter, and number of branches, though not quantified, contributed to a higher pullout force. The FEM simulation results, for barley models, further demonstrated that for the vertical branching angle, the 45° configuration produced the highest pullout force at 5.09 N, approximately double that of the 15° angle (2.84 N). The 80° angle showed a slightly lower force of 4.37 N, a difference of about 14% compared to the 45° configuration. The radial branching angle had a minimal effect on pullout force, with values ranging from 5.09 N to 5.38 N, representing an 8% increase. Lastly, the tortuous root configuration achieved a pullout force of 9.80 N, nearly double the force of the straight root (5.09 N).

In hydrogel, the FEM simulation results for the barley models indicated that the 80° vertical branching angle yielded the highest pullout force at 4.98 N, approximately 60% greater than the 45° angle configuration (3.20 N). The 15° angle displayed the lowest pullout force at 1.04N, demonstrating a significant decrease compared to the 80° configuration. The radial branching angle had a minimal effect on pullout force in hydrogel as well, with values ranging from 3.06 N to 3.30 N, showing a variation of around 10%. Lastly, the tortuous root configuration achieved a pullout force of 3.61 N, just under 10% higher than the straight root configuration (3.20 N).

The results for the mung bean models in soil show that increasing the number of branches per branching point significantly boosts pullout force. The multiple-branch configuration achieved a 14% higher pullout force compared to the single-branch setup (12.78 N vs. 9.17 N) and demonstrated a pullout force approximately 30 times greater than the no-branch configuration (12.78 N vs. 0.34 N). In hydrogel, the multiple-branch configuration also improved interface strength, with a 21% increase in pullout force over the single-branch model (8.66 N vs. 3.22 N) and nearly 24 times the force of the no-branch model (8.66 N vs. 0.36 N). This behavior is attributed to the greater surface area provided by additional branches, which increase the root's interaction with the substrate. The relationship between surface area and maximum pullout force is positive, with increased surface area leading to higher pullout resistance. This effect is more pronounced in soil, where its higher rigidity amplify the impact of surface area, whereas hydrogel's more uniform deformation results in a less significant increase in pullout force.

In addition, the FEM simulations revealed a consistent trend: maximum pullout forces are generally higher in soil than in hydrogel, while displacement at maximum force is consistently greater in hydrogel than in soil. The differences in pullout behavior observed between soil and hydrogel are closely related to their different mechanical properties. Soil, with its rigidity, focuses resistance around the root, quickly increasing pullout force until it reaches a yield point and fractures. Hydrogel, on the other hand, exhibits elasticity, stretching under load without fracturing and providing a more gradual, uniform resistance to deformation.

Overall, the results indicate that root traits beneficial in soil do not necessarily have the same effect in hydrogel. For example, certain traits that increase interface strength in soil, such as root tortuosity or an increased vertical branching angle, were respectively less effective or even counterproductive in hydrogel. This finding underscores the importance of adapting natural design principles to specific material contexts, as direct imitation may not always produce the desired outcomes in engineered settings.

Based on insights from pullout tests and FEM simulations, an optimal root structure is proposed to potentially maximize interface strength across different substrates, offering ideas for bioinspired hard-soft interface designs. For rigid, soil-like materials with high rigidity and localized resistance, a fibrous structure with seminal and adventitious branches is expected to show higher interface strength. In contrast, for hydrogel-like materials with high elasticity and gradual strain distribution, a taproot structure with secondary branches may be more effective. These structures can be optimized by adjusting specific features that perform best with the unique properties of each substrate.

For fibrous systems, maximizing the length and diameter of both adventitious and seminal branches, using a 45° vertical branching angle, spacing branches evenly along the main root, and adding tortuosity in seminal branches are expected to strengthen the interface. Furthermore, stress concentration at the junction between seminal and adventitious roots, a potential failure point, can be reduced by adding a fillet or taper to facilitate smoother load transfer. Similarly, in the taproot system, maximizing branch length and diameter, spacing branches evenly, and introducing a fillet or taper at junctions are anticipated to improve interface strength and minimize stress concentration. In hydrogel, a vertical branching angle closer to 90° strengthens interface strength by increasing resistance to pullout forces through greater bending and stretching in the elastic medium.

This approach has valuable applications in biomedical fields, particularly in tissue engineering, where these interfaces are used to replicate natural transitions between tissues, such as those found between bone and cartilage. Validating these bioinspired designs for practical use led to growing barley and mung bean roots in hydrogel under controlled conditions. Initial results indicate that hydrogel can support initial phases of root growth, highlighting the potential of hydrogel as a substitute for soil. However, these findings represent only a preliminary step, as further studies are needed to understand its limitations and optimize its properties for plant growth.

Investigating how these roots adapt and function in hydrogel opens up endless possibilities for research and application. One possible next step would be to allow the roots to grow further in hydrogel and then perform pullout tests. This would enable a direct comparison between the strength of a fully natural root-soil interface and a “hybrid” interface, where roots grown in hydrogel connect naturally to an engineered substrate. Performing these tests would reveal how effectively these interfaces withstand real pullout forces, offering deeper insight into the interaction between natural and engineered materials and validating the simulations conducted. Moreover, CT scans of the root structure used to create the models for the FEM simulation could be used to create 3D-printed root replicas in materials that mimic the properties of natural roots. These artificial roots could then be embedded in hydrogel, allowing pullout tests on a fully artificial root-hydrogel interface. This approach allows assessment of a fully artificial system, providing a way to measure and compare interface strength across natural, hybrid, and fully engineered setups. Conducting this work would

allow assessment, both theoretically and experimentally, of how interface strength translates across substrates with different stiffness and material properties for various root structures.

The current FEM model was validated through energy history output results and mesh convergence analysis. The energy history output demonstrated that the model accurately captures the physical behavior of the system, including energy conservation and distribution, without significant numerical artifacts. Mesh convergence analysis showed that even coarser meshes provided reasonable accuracy, with minimal variation in maximum force (about 6% between the chosen mesh and the finest mesh). The mesh with 121,161 elements was found to offer the optimal balance between computational efficiency and accuracy, making it the most practical choice for simulations.

Moving forward, further implementation of the FEM model and simulations can also be pursued. First, additional parameters not considered in the current study could be incorporated, including more variables related to root and substrate properties. Furthermore, combinations of these parameters could be tested to identify which factors most significantly influence the maximum pullout force. This approach would provide a deeper understanding of the root-substrate interaction and how different conditions affect root anchorage. Moreover, regarding failure mechanisms, the current model is limited because it only evaluates the maximum pullout force without considering the different failure behavior of the root system. To address this, the model should incorporate subroutines to simulate real damage to the root-substrate interface. Implementing this would enable the model to realistically predict failure and simulate the breakage mechanisms within the root structure, closely replicating the behavior observed in laboratory tests. To improve the accuracy and realism of the simulations, the model could be run with longer time steps and a finer mesh, although this would significantly increase computational demands. Extending the simulation duration would provide more comprehensive insights into how root systems interact with substrates over time. Meanwhile, using a finer mesh would improve the resolution of the simulation, capturing smaller-scale details in root-substrate interactions. Lastly, to improve the accuracy of the root model, it would be beneficial to use all available slices from the CT scan rather than just a subset. The current models are based on a limited number of slices, leading to simplifications. Using the complete 3D structure from the CT scan would result in a more detailed and realistic representation of root morphology.

Overall, this study provides valuable insights into root-soil and root-hydrogel interactions, laying the foundation for future advancements in modeling engineered hard-soft interfaces. It bridges the gap between nature and engineering by demonstrating that directly replicating characteristics that increase interface strength in nature is insufficient as a design strategy for improving hard-soft interface materials. While nature offers valuable inspiration, engineers must carefully adapt these features to specific materials to ensure optimal performance in real-world applications.

References

1. Saldívar, M., et al., *Bioinspired rational design of bi-material 3D printed soft-hard interfaces.* Nature Communications, 2023. **14**(1): p. 7919.
2. Vesvoranan, O., A. Anup, and K.R. Hixon, *Current concepts and methods in tissue interface scaffold fabrication.* Biomimetics, 2022. **7**(4): p. 151.
3. Miserez, A., et al., *The transition from stiff to compliant materials in squid beaks.* Science, 2008. **319**(5871): p. 1816-1819.
4. Zhang, H., et al., *Rational Design of Soft–Hard Interfaces through Bioinspired Engineering.* Small, 2023. **19**(1): p. 2204498.
5. Meyers, M.A., et al., *Biological materials: Structure and mechanical properties.* Progress in materials science, 2008. **53**(1): p. 1-206.
6. Miserez, A., et al., *Jumbo squid beaks: inspiration for design of robust organic composites.* Acta biomaterialia, 2007. **3**(1): p. 139-149.
7. Tan, Y., et al., *Infiltration of chitin by protein coacervates defines the squid beak mechanical gradient.* Nature chemical biology, 2015. **11**(7): p. 488-495.
8. Raabe, D., C. Sachs, and P. Romano, *The crustacean exoskeleton as an example of a structurally and mechanically graded biological nanocomposite material.* Acta Materialia, 2005. **53**(15): p. 4281-4292.
9. Boldrin, D., A.K. Leung, and A. Bengough, *Root biomechanical properties during establishment of woody perennials.* Ecological Engineering, 2017. **109**: p. 196-206.
10. Suralta, R.R., et al., *Root plasticity for maintenance of productivity under abiotic stressed soil environments in rice: Progress and prospects.* Field Crops Research, 2018. **220**: p. 57-66.
11. Stachew, E., T. Houette, and P. Gruber, *Root Systems Research for bioinspired resilient design: a concept framework for foundation and Coastal engineering.* Frontiers in Robotics and AI, 2021. **8**: p. 548444.
12. Houette, T., et al., *Pullout resistance of biomimetic root-inspired foundation systems.* Acta Geotechnica, 2023: p. 1-20.
13. Dupuy, L., T. Fourcaud, and A. Stokes, *A numerical investigation into the influence of soil type and root architecture on tree anchorage.* Plant and soil, 2005. **278**: p. 119-134.
14. Veylon, G., et al., *Quantification of mechanical and hydric components of soil reinforcement by plant roots.* Canadian Geotechnical Journal, 2015. **52**(11): p. 1839-1849.
15. Dupuy, L.X., et al., *A generic 3D finite element model of tree anchorage integrating soil mechanics and real root system architecture.* American Journal of Botany, 2007. **94**(9): p. 1506-1514.
16. Zhang, Y.S. and A. Khademhosseini, *Advances in engineering hydrogels.* Science, 2017. **356**(6337): p. eaaf3627.
17. Baier Leach, J., et al., *Photocrosslinked hyaluronic acid hydrogels: natural, biodegradable tissue engineering scaffolds.* Biotechnology and bioengineering, 2003. **82**(5): p. 578-589.
18. Ma, L., et al., *Hydrogel-based transparent soils for root phenotyping in vivo.* Proceedings of the National Academy of Sciences, 2019. **116**(22): p. 11063-11068.
19. Ma, L., et al., *Hydrogels as the plant culture substrates: A review.* Carbohydrate Polymers, 2023. **305**: p. 120544.
20. Wang, N., et al., *Alginate-based composites as novel soil conditioners for sustainable applications in agriculture: A critical review.* Journal of Environmental Management, 2023. **348**: p. 119133.
21. Yangirova, R.R., G.A. Mazhatovich, and H.I. Fanilevich, *The Effect of Hydrogel on Plant Growth.* International Journal of Oil, Gas and Coal Engineering, 2021. **7**(1): p. 59-62.
22. Patra, S.K., et al., *Prospects of hydrogels in agriculture for enhancing crop and water productivity under water deficit condition.* International Journal of Polymer Science, 2022. **2022**(1): p. 4914836.
23. Park, J., et al., *Self-irrigation and slow-release fertilizer hydrogels for sustainable agriculture.* ACS Materials Letters, 2024. **6**(8): p. 3471-3477.
24. Hou, S., H. Sun, and Y. Zhou, *Influence of super absorbent polymer on root characteristics and anchorage of amorpha fruticosa on rocky slope.* Applied Sciences, 2022. **12**(5): p. 2640.

25. Staley, J., *A Study of Shear Strength of a Sustainable Structural Biomaterial via a Pullout Test*. 2022, University of Colorado at Boulder.
26. Illeperuma, W.R.K., *Mechanical behavior of tough hydrogels for structural applications*. 2015.
27. Mickovski, S., et al., *Resistance of simple plant root systems to uplift loads.* Canadian Geotechnical Journal, 2010. **47**(1): p. 78-95.
28. Gorzolka, K., et al., *Spatio-temporal metabolite profiling of the barley germination process by MALDI MS imaging.* PLoS One, 2016. **11**(3): p. e0150208.
29. Fong, E., et al., *The Effects of Salinity on Mung Bean (Vigna radiata) Seed Germination.* The Expedition, 2021. **12**.
30. Esau, K., *Plant anatomy.* 1965.
31. Kamil, S.S.S.M., *Model Test on the Effects of Some Root Properties on Pullout Capacity*. 2013, University of Malaya (Malaysia).
32. Sadhana, N.H., et al., *Navigating towards dry root rot resistance in mungbean: impacts, mechanisms, and management strategies.* Plant Physiology Reports, 2024. **29**(3): p. 439-460.
33. Knipfer, T. and W. Fricke, *Root aquaporins*, in *Root Engineering: Basic and Applied Concepts*. 2014, Springer. p. 269-296.
34. Michaelis, J. and M. Diekmann, *Effects of soil types and bacteria inoculum on the cultivation and reintroduction success of rare plant species.* Plant ecology, 2018. **219**(4): p. 441-453.
35. Zhu, H., et al., *Enhancing saltgrass germination and growth in a saline soil contaminated with petroleum hydrocarbons.* Plant and Soil, 2017. **412**: p. 189-199.
36. Schwarz, M., D. Cohen, and D. Or, *Pullout tests of root analogs and natural root bundles in soil: Experiments and modeling.* Journal of Geophysical Research-Earth Surface, 2011. **116**.
37. Giadrossich, F., et al., *Mechanical interactions between neighbouring roots during pullout tests.* Plant and soil, 2013. **367**: p. 391-406.
38. Giadrossich, F., et al., *Methods to measure the mechanical behaviour of tree roots: A review.* Ecological engineering, 2017. **109**: p. 256-271.
39. Zápražný, Z., et al., *Experience with imaging by using of microfocus x-ray source.* Journal of Electrical Engineering, 2010. **61**(5): p. 287-290.
40. Hong, Z., et al. *Multi-attentional u-net for medical image segmentation*. in *2022 2nd International Symposium on Artificial Intelligence and its Application on Media (ISAIAM)*. 2022. IEEE.
41. Stokes, A., et al., *An experimental investigation of the resistance of model root systems to uprooting.* Annals of Botany, 1996. **78**(4): p. 415-421.
42. Schwarz, M., P. Lehmann, and D. Or, *Quantifying lateral root reinforcement in steep slopes–from a bundle of roots to tree stands.* Earth Surface Processes and Landforms: The Journal of the British Geomorphological Research Group, 2010. **35**(3): p. 354-367.
43. Khalilnejad, A., et al., *Finite element simulation for the impact of Root Morphology on pulling-out process.* 2012.
44. Khalilnejad, A., *Numerical simulation and experimental study of root anchorage*. 2013: University of Malaya (Malaysia).
45. Fourcaud, T., et al., *Understanding the Impact of Root Morphology on Overturning Mechanisms: A Modelling Approach.* Annals of Botany, 2007. **101**(8): p. 1267-1280.
46. Giwangkara, G.G., et al., *Analysis of internal friction angle and cohesion value for road base materials in a specified gradation.* JACEE (Journal of Advanced Civil and Environmental Engineering), 2020. **3**(2): p. 58-65.
47. Qamar, S.Z., M. Akhtar, and T. Pervez, *Swelling Elastomers: Comparison of Material Models*, in *Swelling Elastomers in Petroleum Drilling and Development-Applications, Performance Analysis, and Material Modeling*. 2021, IntechOpen.
48. Kolel, A., et al., *Strain gradient programming in 3D fibrous hydrogels to direct graded cell alignment.* Small Methods, 2023. **7**(1): p. 2201070.
49. Yildirim, E.D., et al., *Fabrication, characterization, and biocompatibility of single-walled carbon nanotube-reinforced alginate composite scaffolds manufactured using freeform fabrication technique.* Journal of Biomedical Materials Research Part B: Applied Biomaterials: An Official Journal

of The Society for Biomaterials, The Japanese Society for Biomaterials, and The Australian Society for Biomaterials and the Korean Society for Biomaterials, 2008. **87**(2): p. 406-414.
50. Ogden, R.W., *Large deformation isotropic elasticity–on the correlation of theory and experiment for incompressible rubberlike solids.* Proceedings of the Royal Society of London. A. Mathematical and Physical Sciences, 1972. **326**(1567): p. 565-584.
51. Kunkels, L.B., T.U. Delft, Editor. 2024.
52. Idkaidek, A. and I. Jasiuk, *Toward high-speed 3D nonlinear soft tissue deformation simulations using Abaqus software.* Journal of robotic surgery, 2015. **9**: p. 299-310.
53. Demirci, H.E., et al. *Finite element model of buried pipelines crossing strike-slip faults by ABAQUS/EXPLICIT*. in *16th European Conference on Earthquake Engineering: Thessaloniki-2018*. 2018. Springer, Cham.
54. Inc, A., *ABAQUS Analysis User's Manual: Version 6.6*. 2006: ABAQUS, Incorporated.
55. Okereke, M., et al., *Finite element mesh generation.* Finite Element Applications: A Practical Guide to the FEM Process, 2018: p. 165-186.
56. Sharma, R., et al., *A critical review on classified excipient sodium-alginate-based hydrogels: modification, characterization, and application in soft tissue engineering.* Gels, 2023. **9**(5): p. 430.
57. CAHYONO, J., F.E. SOETAREJO, and S. ISMADJI, *UTILIZATION OF SODIUM ALGINATE HYDROGEL AS A SUSTAINABLE PLANTING MEDIUM.* AgroLife Scientific Journal, 2023. **12**(2): p. 46-53.
58. Song, B., et al., *Hydrogel synthesis based on lignin/sodium alginate and application in agriculture.* International Journal of Biological Macromolecules, 2020. **144**: p. 219-230.
59. Bociaga, D., et al., *Sodium alginate/gelatine hydrogels for direct bioprinting—The effect of composition selection and applied solvents on the bioink properties.* Materials, 2019. **12**(17): p. 2669.
60. Kaklamani, G., et al., *Mechanical properties of alginate hydrogels manufactured using external gelation.* Journal of the mechanical behavior of biomedical materials, 2014. **36**: p. 135-142.
61. Kuo, C.K. and P.X. Ma, *Ionically crosslinked alginate hydrogels as scaffolds for tissue engineering: Part 1. Structure, gelation rate and mechanical properties.* Biomaterials, 2001. **22**(6): p. 511-521.
62. Yi, Y., et al., *Effects of calcium salts on experimental characterizations of sodium alginate hydrogels and the drug release of electrospun naringin-loaded microspheres hybrid hydrogel scaffolds.* Materials Letters, 2023. **333**: p. 133663.
63. Zhao, C., et al., *Gelation of Na-alginate aqueous solution: A study of sodium ion dynamics via NMR relaxometry.* Carbohydrate polymers, 2017. **169**: p. 206-212.
64. Winarti, C., K. Sasmitaloka, and A. Arif. *Effect of NPK fertilizer incorporation on the characteristics of nanocellulose-based hydrogel*. in *IOP conference series: earth and environmental science*. 2021. IOP Publishing.
65. Leštan, D., M. Leštan, and R. Lamar, *Growth and viability of mycelial fragments of white-rot fungi on some hydrogels.* Journal of Industrial Microbiology and Biotechnology, 1998. **20**(3-4): p. 244-250.
66. Noble, W., O. Lidwell, and D. Kingston, *The size distribution of airborne particles carrying micro-organisms.* Epidemiology & Infection, 1963. **61**(4): p. 385-391.
67. Pietikäinen, J., M. Pettersson, and E. Bååth, *Comparison of temperature effects on soil respiration and bacterial and fungal growth rates.* FEMS microbiology ecology, 2005. **52**(1): p. 49-58.
68. Zou, Y., et al., *Advances in plant seed-associated microbial ecology.* Shengtai Xuebao/Acta Ecologica Sinica, 2011. **31**(10): p. 2906-2914.
69. MacCallum, D.M., *Antifungal agents*, in *Oxford Textbook of Medical Mycology*, C.C. Kibbler, et al., Editors. 2018, Oxford University Press. p. 0.
70. Misra, A.N. and M. Misra, *Sterilisation techniques in plant tissue culture.* Fakir Mohan University, Balasore, 2012.
71. Levie, R.d., *Curve fitting with least squares.* Critical Reviews in Analytical Chemistry, 2000. **30**(1): p. 59-74.
72. Carpenter, R., *Principles and procedures of statistics, with special reference to the biological sciences.* The Eugenics Review, 1960. **52**(3): p. 172.
73. Cao, L., et al., *A new flexible sigmoidal growth model.* Symmetry, 2019. **11**(2): p. 204.
74. Robinson, D., *Rethinking root-shoot growth dynamics.* bioRxiv, 2020: p. 2020.06. 29.177824.

75. Liu, J.-H., et al., *Simulation of crop growth, time to maturity and yield by an improved sigmoidal model.* Scientific Reports, 2018. **8**(1): p. 7030.
76. Bloom, A., *Coordination between shoots and roots*, in *Vascular transport in plants*. 2005, Elsevier. p. 241-256.
77. Lynch, J., *Root architecture and plant productivity.* Plant physiology, 1995. **109**(1): p. 7.
78. Dias, A.S., M. Pirone, and G. Urciuoli. *Review on types of root failures in shallow landslides*. in *Advancing Culture of Living with Landslides: Volume 2 Advances in Landslide Science*. 2017. Springer.
79. Hamza, O., et al., *Mechanics of root-pullout from soil: A novel image and stress analysis procedure.* Eco- and Ground Bio-Engineering: The Use of Vegetation to Improve Slope Stability, 2007. **103**: p. 213-+.
80. Schwarz, M., D. Cohen, and D. Or, *Root-soil mechanical interactions during pullout and failure of root bundles.* Journal of Geophysical Research-Earth Surface, 2010. **115**.
81. Fan, C.-C., J.Z. Lu, and H.H. Chen, *The pullout resistance of plant roots in the field at different soil water conditions and root geometries.* Catena, 2021. **207**: p. 105593.
82. Cislaghi, A., *Exploring the variability in elastic properties of roots in Alpine tree species.* Journal of Forest Science, 2021. **67**(7): p. 338-356.
83. Norris, J.E., *Root reinforcement by hawthorn and oak roots on a highway cut-slope in Southern England.* Plant and Soil, 2005. **278**: p. 43-53.
84. ENNOS, A.R., *The anchorage of leek seedlings: the effect of root length and soil strength.* Annals of Botany, 1990. **65**(4): p. 409-416.
85. Lontoc-Roy, M., et al., *Advances in the acquisition and analysis of CT scan data to isolate a crop root system from the soil medium and quantify root system complexity in 3-D space.* Geoderma, 2006. **137**(1-2): p. 231-241.
86. Davey, E., et al., *Use of computed tomography imaging for quantifying coarse roots, rhizomes, peat, and particle densities in marsh soils.* Ecological Applications, 2011. **21**(6): p. 2156-2171.
87. Phalempin, M., et al., *An improved method for the segmentation of roots from X-ray computed tomography 3D images: Rootine v. 2.* Plant Methods, 2021. **17**: p. 1-19.
88. Soltaninejad, M., et al., *Three dimensional root CT segmentation using multi-resolution encoder-decoder networks.* IEEE Transactions on Image Processing, 2020. **29**: p. 6667-6679.
89. Garbout, A., et al., *The use of PET/CT scanning technique for 3D visualization and quantification of real-time soil/plant interactions.* Plant and soil, 2012. **352**: p. 113-127.
90. Vergani, C., et al., *Effects of root tensile force and diameter distribution variability on root reinforcement in the Swiss and Italian Alps.* Canadian Journal of Forest Research, 2014. **44**(11): p. 1426-1440.
91. Dupuy, L., et al., *A density-based approach for the modelling of root architecture: application to Maritime pine (Pinus pinaster Ait.) root systems.* Journal of Theoretical Biology, 2005. **236**(3): p. 323-334.
92. Young, I., *Biophysical interactions at the root–soil interface: a review.* The Journal of Agricultural Science, 1998. **130**(1): p. 1-7.
93. Roose, T. and A. Schnepf, *Mathematical models of plant–soil interaction.* Philosophical Transactions of the Royal Society A: Mathematical, Physical and Engineering Sciences, 2008. **366**(1885): p. 4597-4611.

Appendices

Appendices related to Section 2.1: Methodology for Seed Planting.

Table 16: Product information of universal potting ground used in laboratory experiment.

Product Information	**Details**
Name	Ranzijn Potgrond Universeel 40L
SKU	334350
Brand (Merk)	Eigen merk
EAN	2600009991972
Composition	Potting soil based on garden peat, peat litter, green compost, lime, and fertilizers
pH (Water) Zone	5.0 - 6.5
Fertilizer NPK (14-16-18)	1.2 kg/m³
Net Weight	14 kg
Net Volume	40 L (EN 12580)

Appendices related to Section 2.2: Pullout Test Methodology.

Table 17: Technical specifications of tensile testing machine used in laboratory experiment.

Category	**Details**
Tensile Test Machine	Lloyd LR5K
Electrical Power	1 x 240 VAC, 16A (3.5 kW)
Load Range	5.0 kN load capacity
Force Measuring Accuracy	< +/- 0.5% of load cell used (maximum)
Crosshead Speed Range	0.2 - 1000 mm/min
Speed Accuracy	< +/- 0.5%
Clearance Between Columns	400 mm
Maximum Crosshead Displacement	1100 mm (excluding grips)
Extension Resolution	< 5 microns
Frame Stiffness (without load cell)	> 25 kN/mm
Supply Voltage	230V or 110V (switchable)
Main Frame Dimensions	h1550 mm x d500 mm x w600 mm
Mass	105 kg

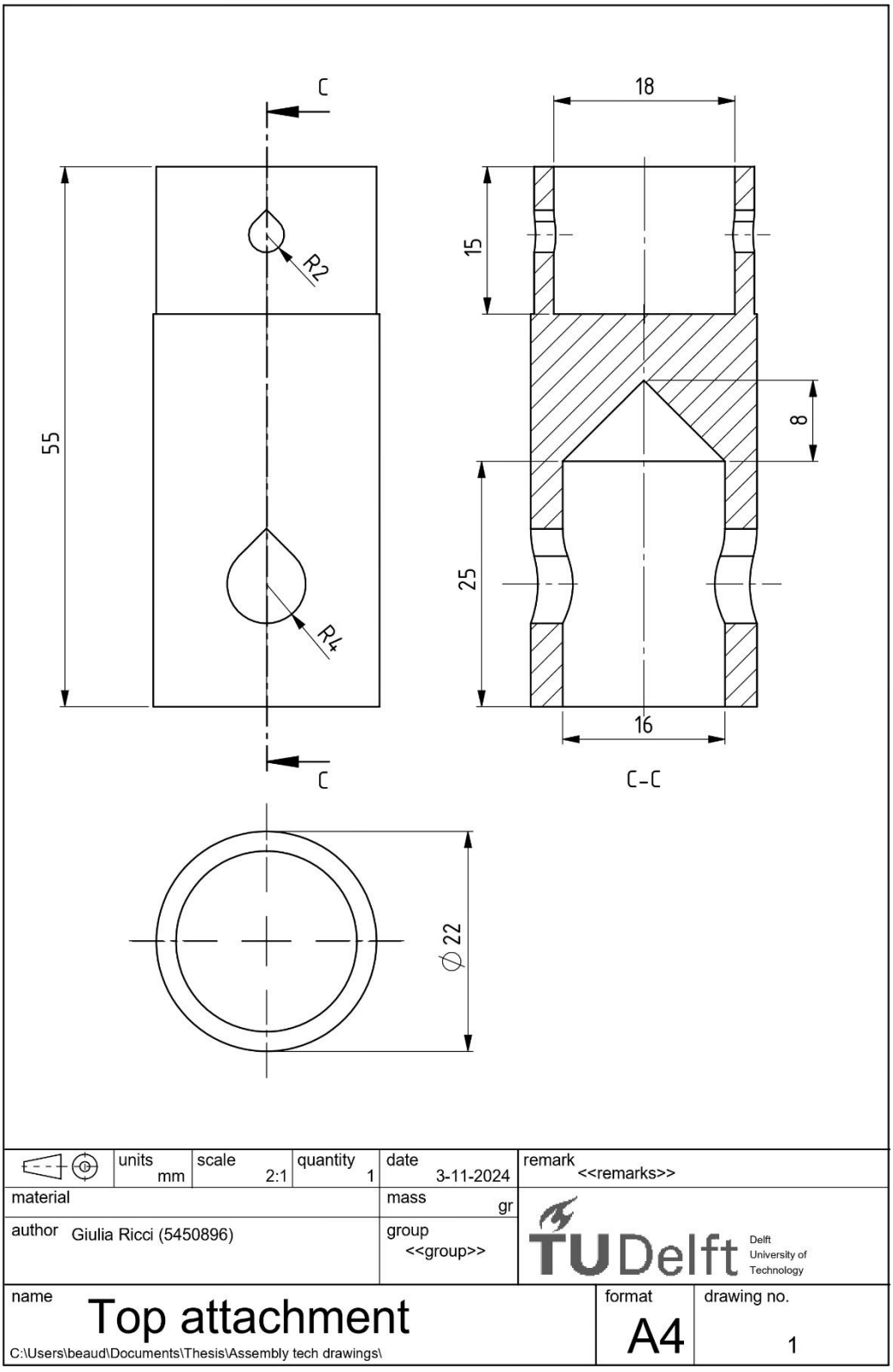

Figure 38: Technical drawing of the top attachment (part 1) of the tensile test setup designed for the experiment.

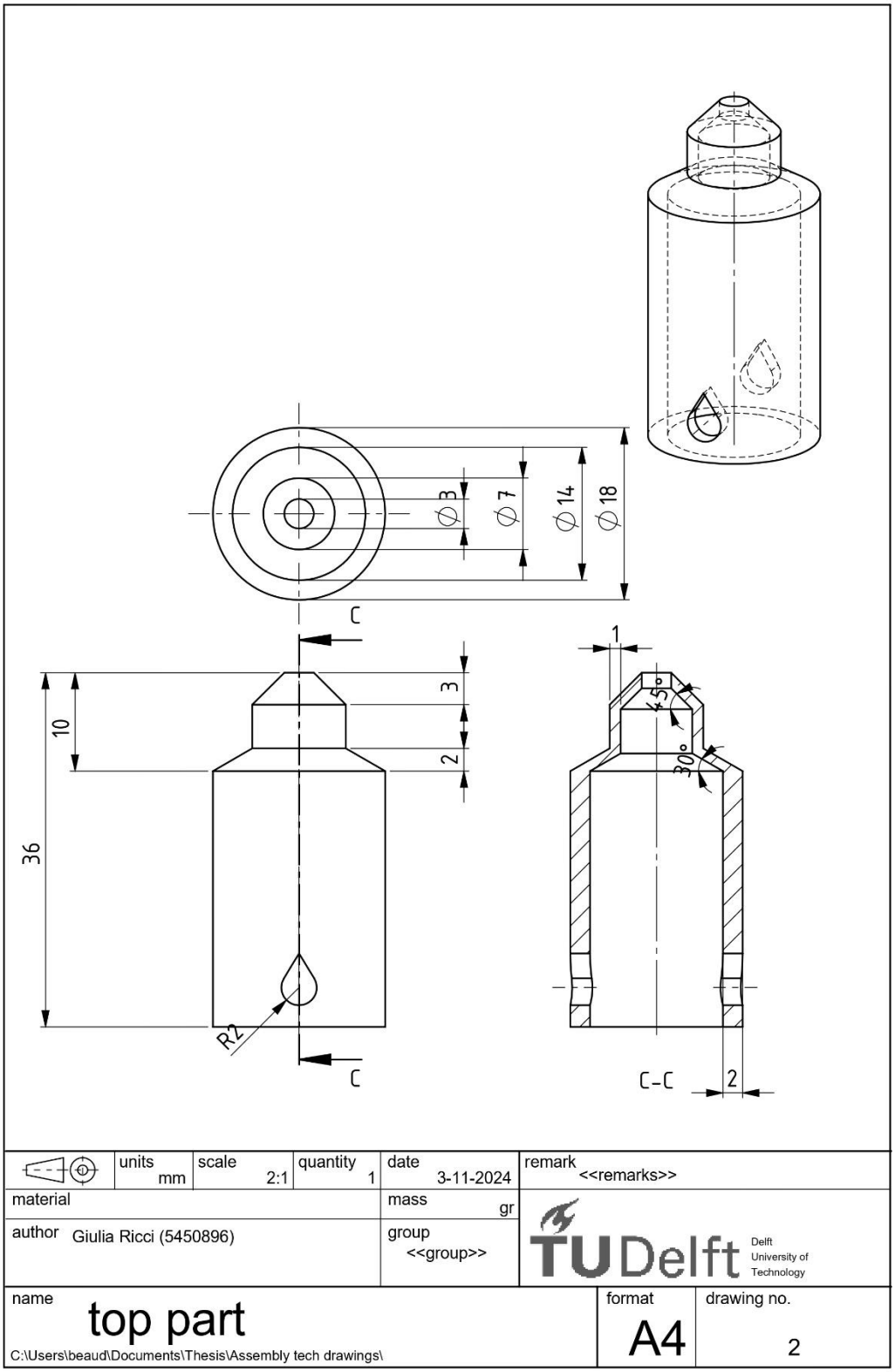

Figure 39: Technical drawing of the top part (part 2) of the tensile test setup designed for the experiment.

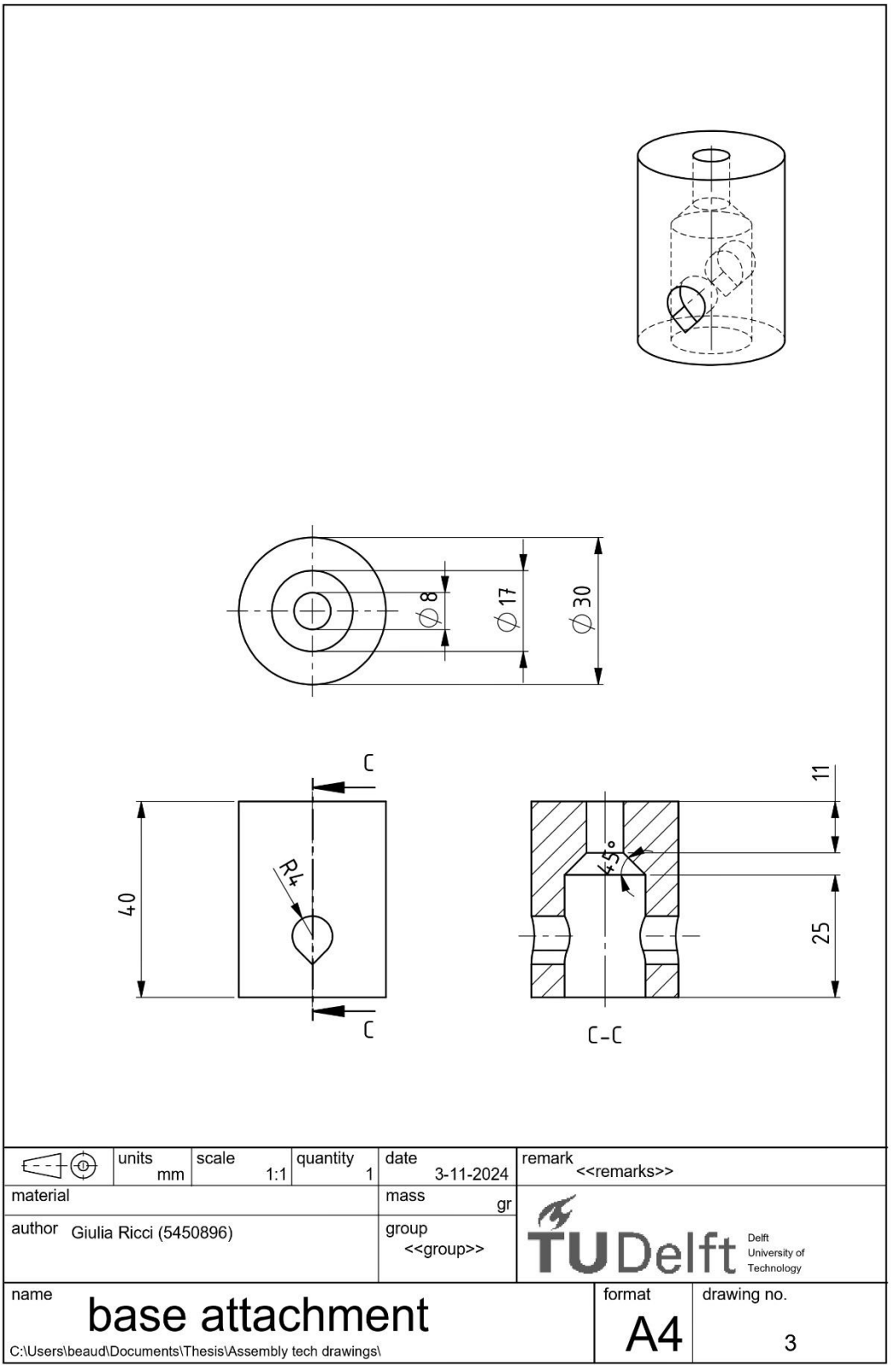

Figure 40: Technical drawing of the base attachment (part 3) of the tensile test setup designed for the experiment.

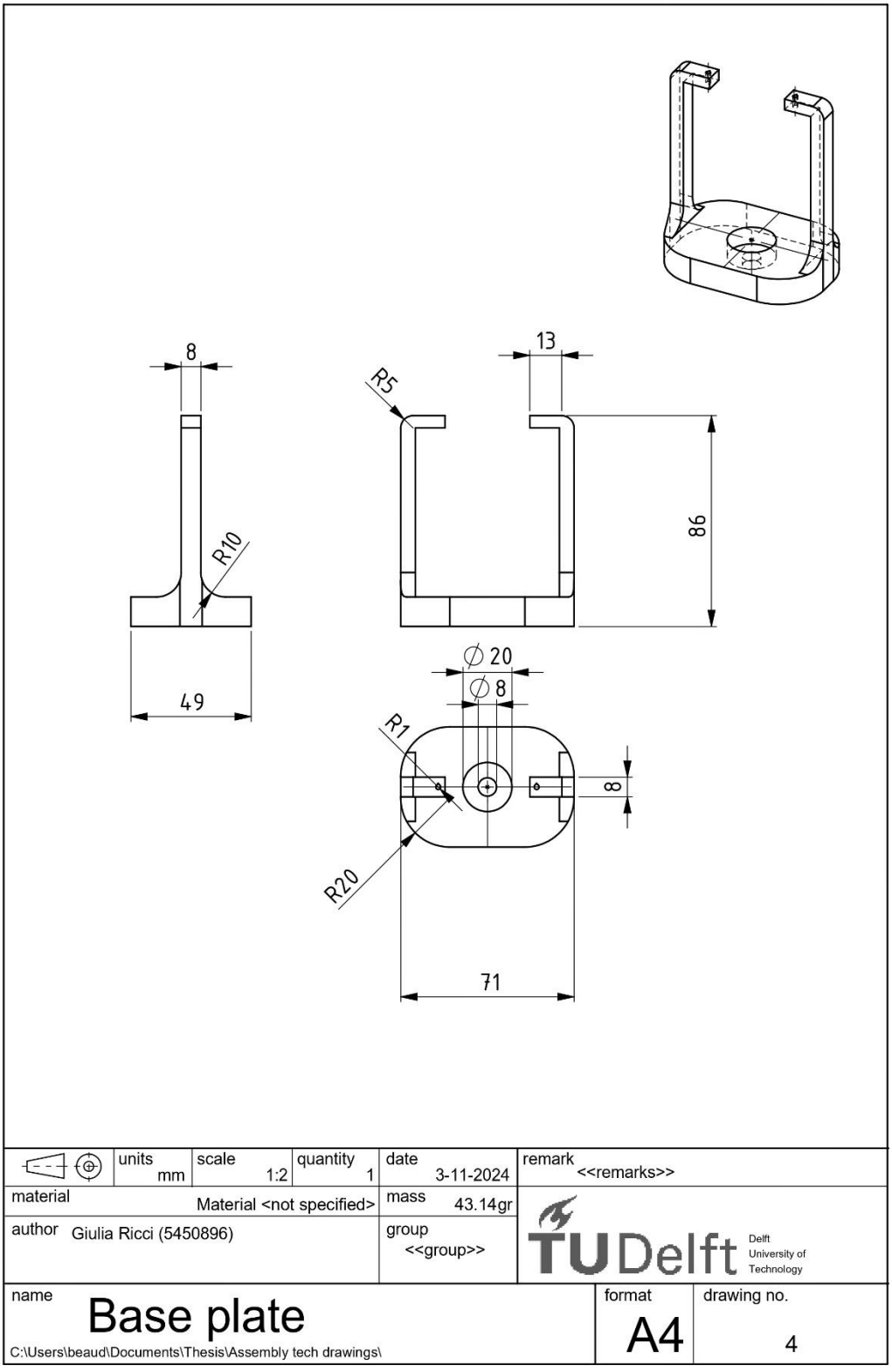

Figure 41: Technical drawing of the base plate (part 4) of the tensile test setup designed for the experiment.

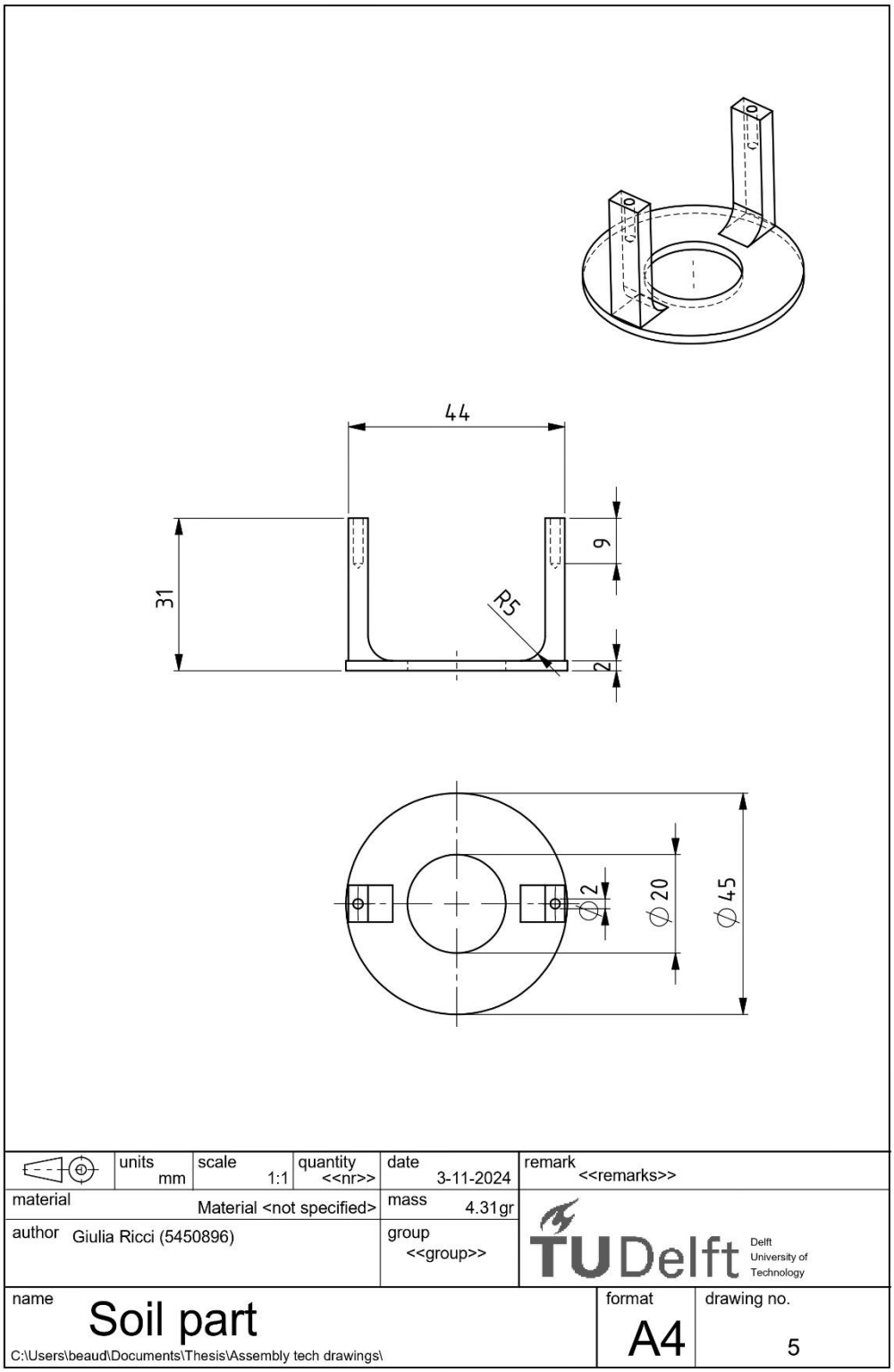

Figure 42: Technical drawing of the soil holder (part 5) of the tensile test setup designed for the experiment.

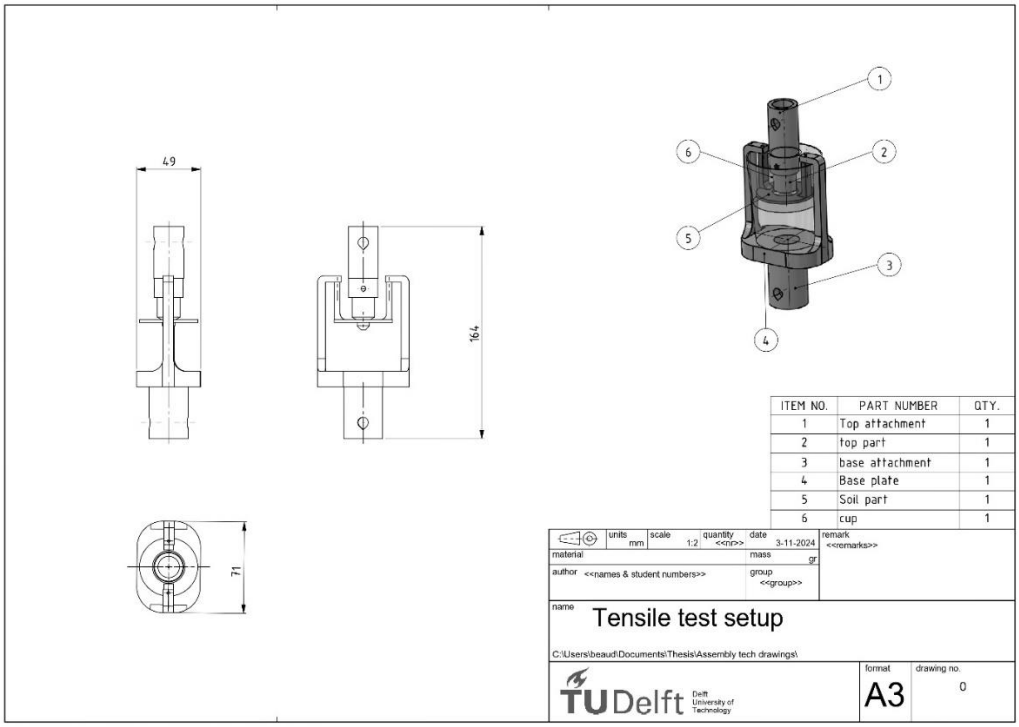

Figure 43: Technical drawing of the assembly of the tensile test setup designed for the experiment.

Appendices related to Section 2.3: CT Scanning Methodology.

Table 18: Technical specifications of Micro-CT system machine used for CT scans.

Category	**Details**
Micro-CT system	TESCAN CoreTOM
Aquila Version	4146
Max. temporal resolution	< 10 seconds
Max. spatial resolution	3 µm
X-ray source	30 – 180 kV or 30 – 230 kV 300 W Type: Open / Reflection
Focus Mode of X-ray source	Microfocus
Vacuum Level	1.142353E-6
X-ray detector	Large amorphous Si flat panel detector 2856 × 2856 pixels
Max. sample size (Ø × h)	600 mm ×1150 mm
Max. CT FOV (Ø × h)	300 mm × 1000 mm
Max. sample weight	45 kg
Motorization	9 stages mounted on a high precision granite base
Source-Detector Distance	970 mm
System dimensions	1.5 × 2.5 × 2.1 m (W × L × H)
System weight3	4900 kg

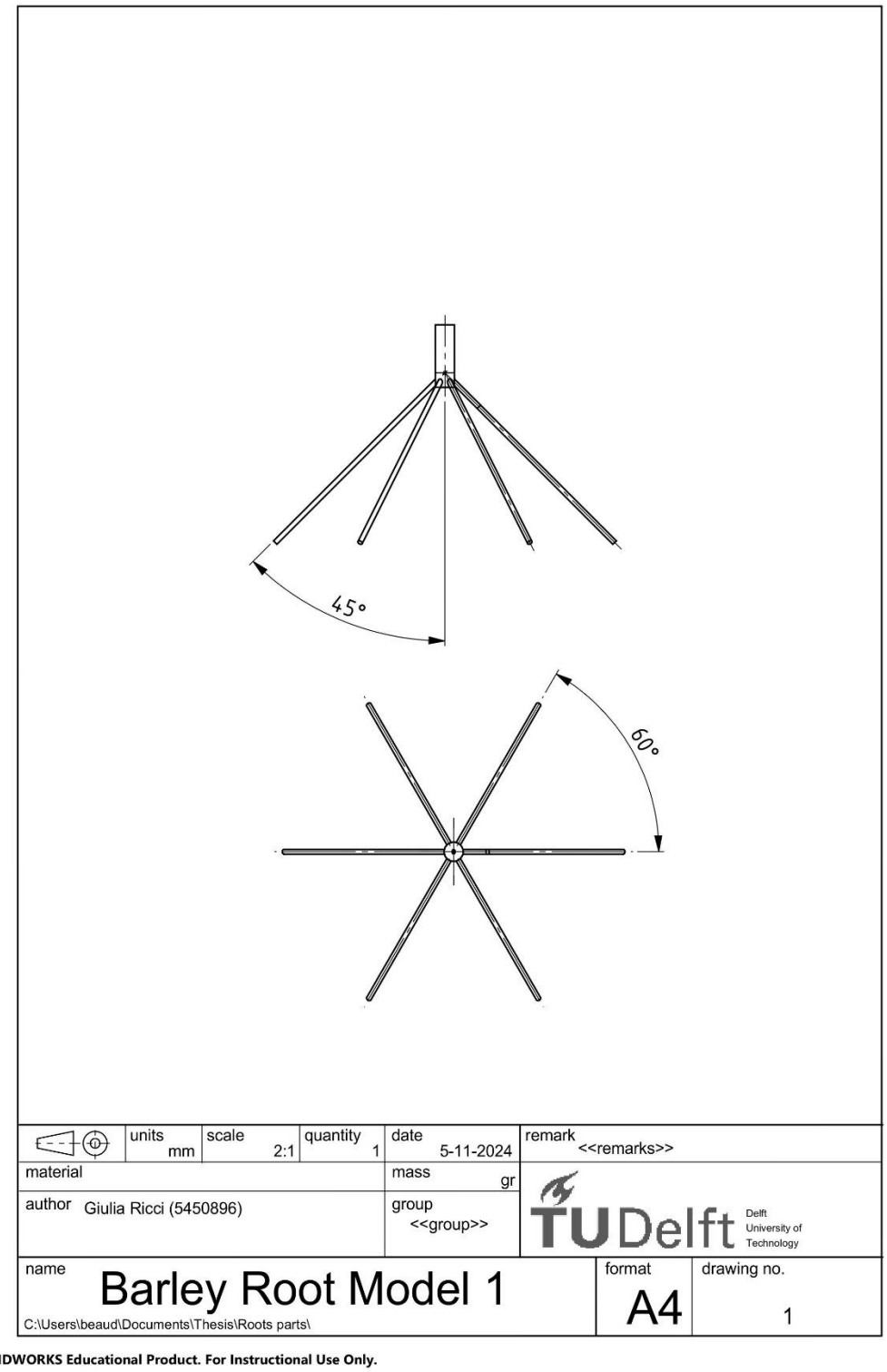

Figure 44: Technical drawing of Model 1 for barley roots, with specified parameters.

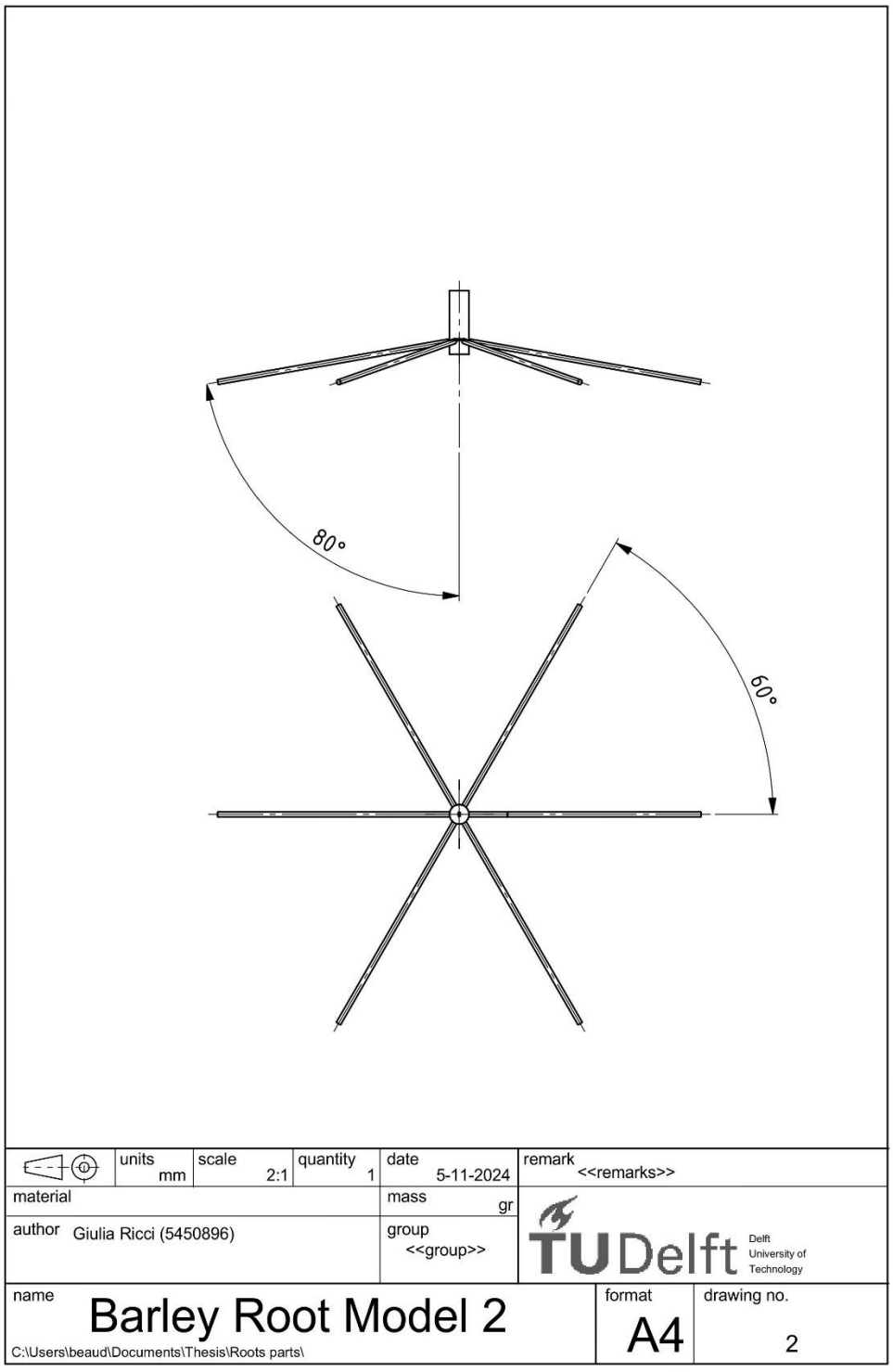

Figure 45: Technical drawing of Model 2 for barley roots, with specified parameters.

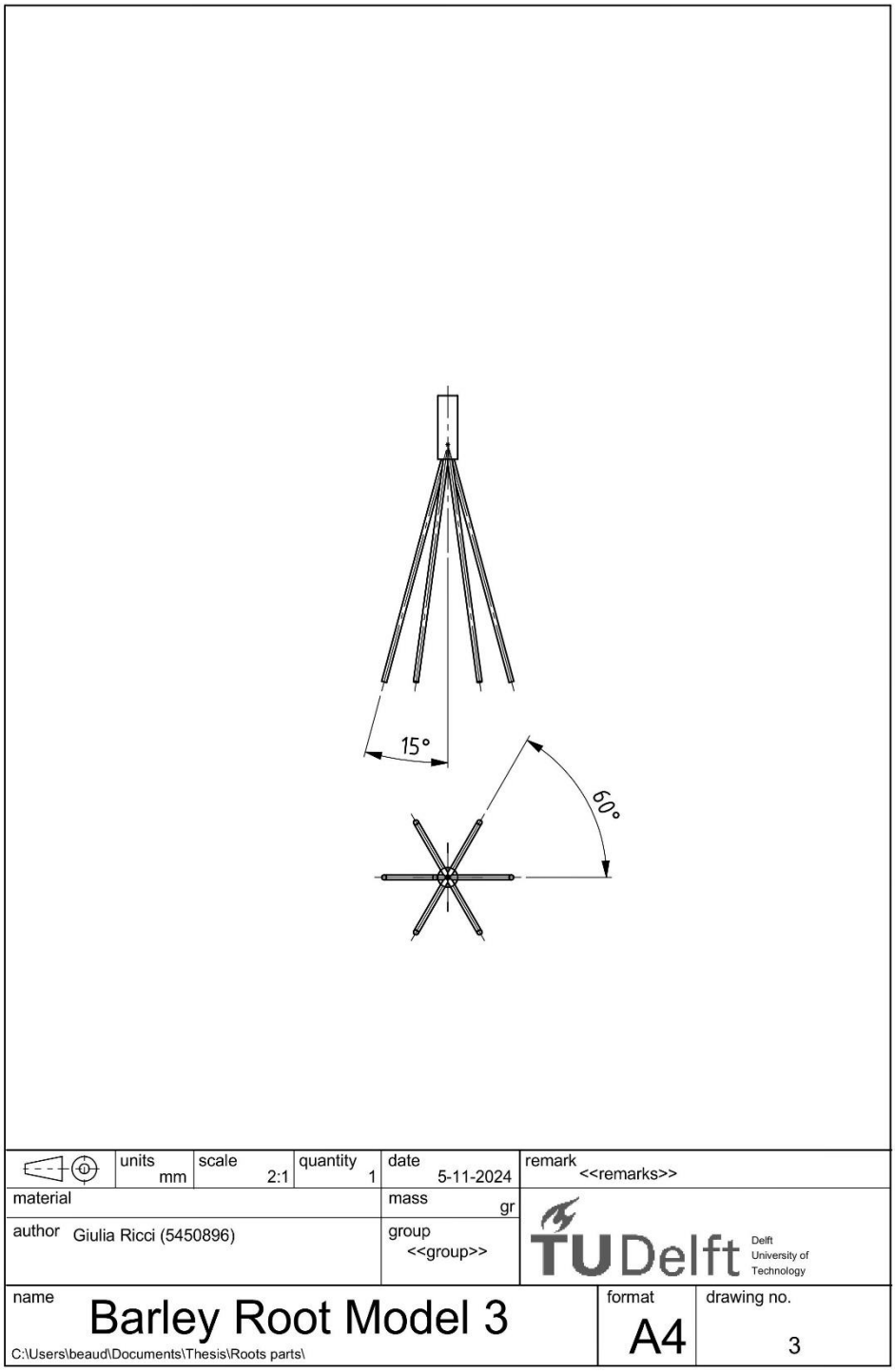

Figure 46: Technical drawing of Model 3 for barley roots, with specified parameters.

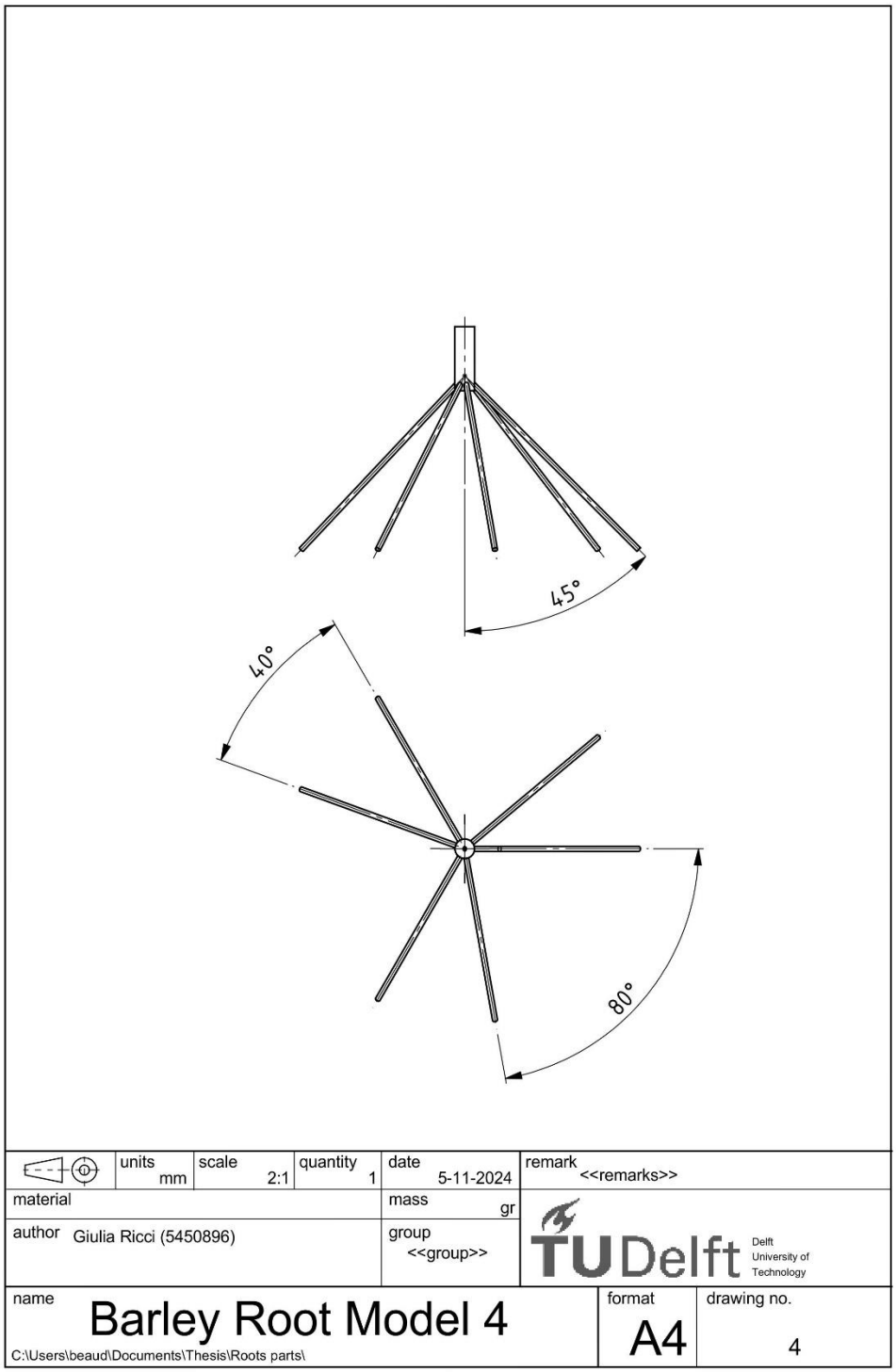

Figure 47: Technical drawing of Model 4 for barley roots, with specified parameters.

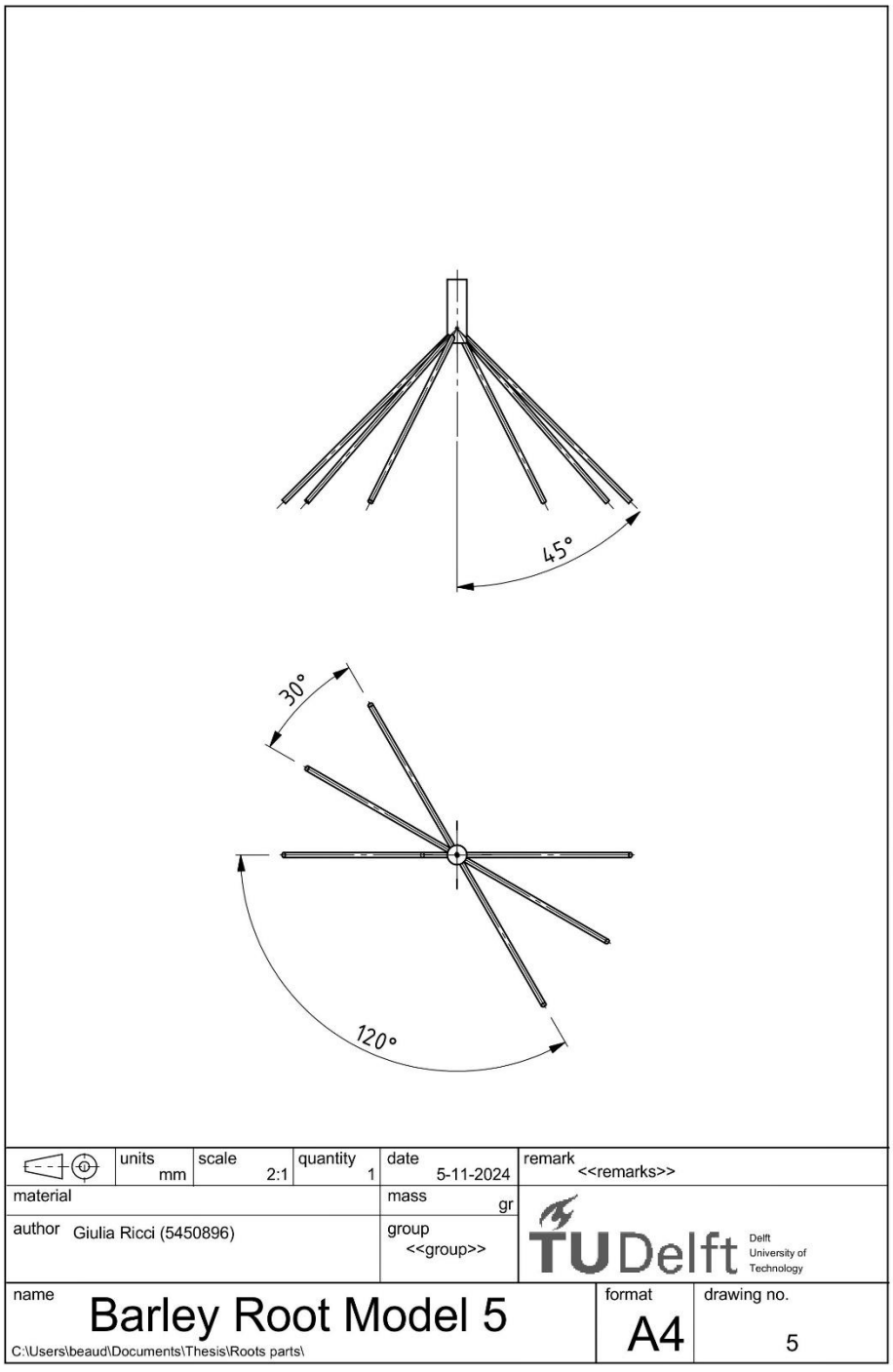

Figure 48: Technical drawing of Model 5 for barley roots, with specified parameters.

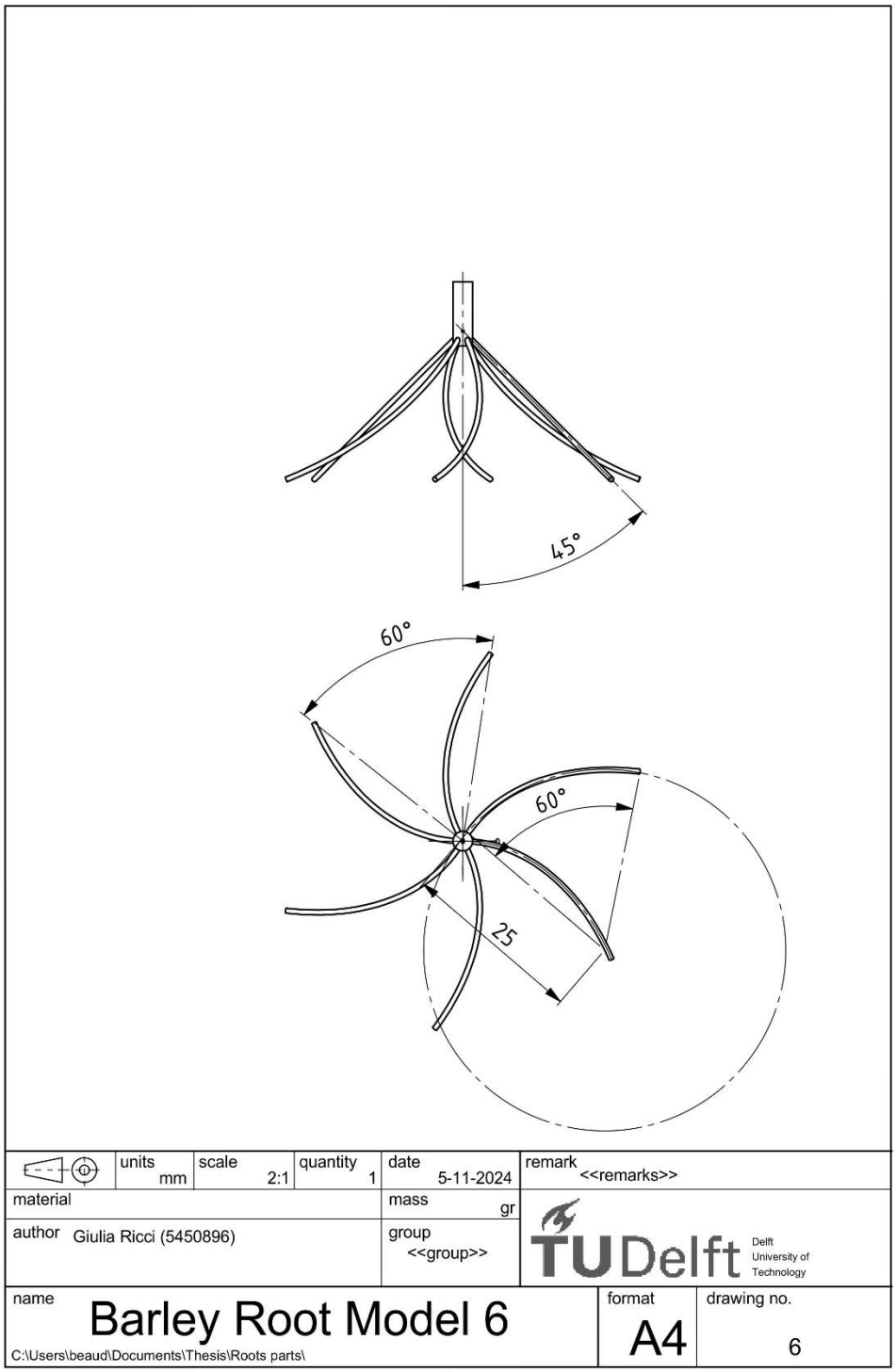

Figure 49: Technical drawing of Model 6 for barley roots, with specified parameters. All lengths are measured in millimeters (mm).

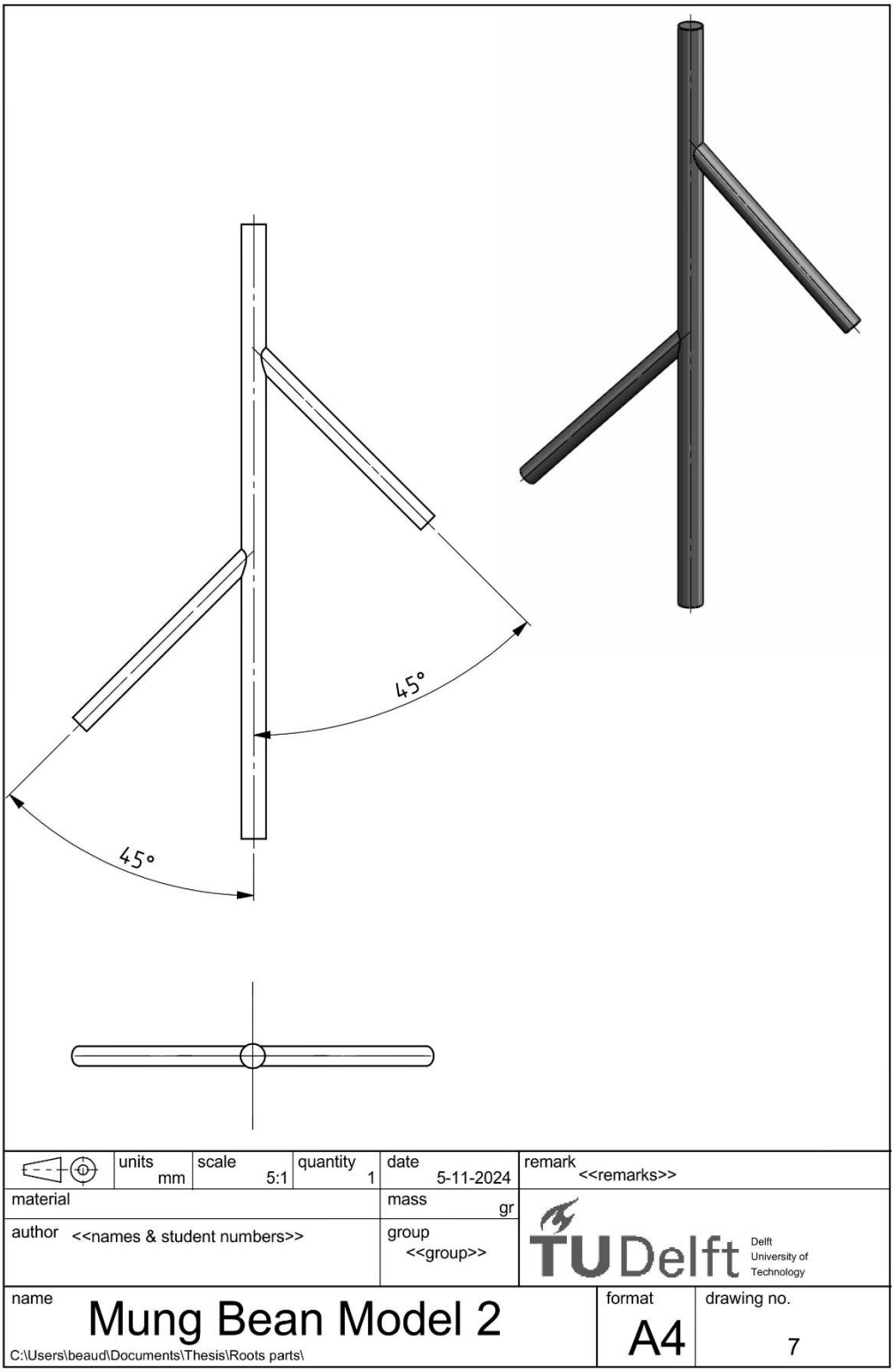

Figure 50: Technical drawing of Model 2 for mung bean roots, with specified parameters.

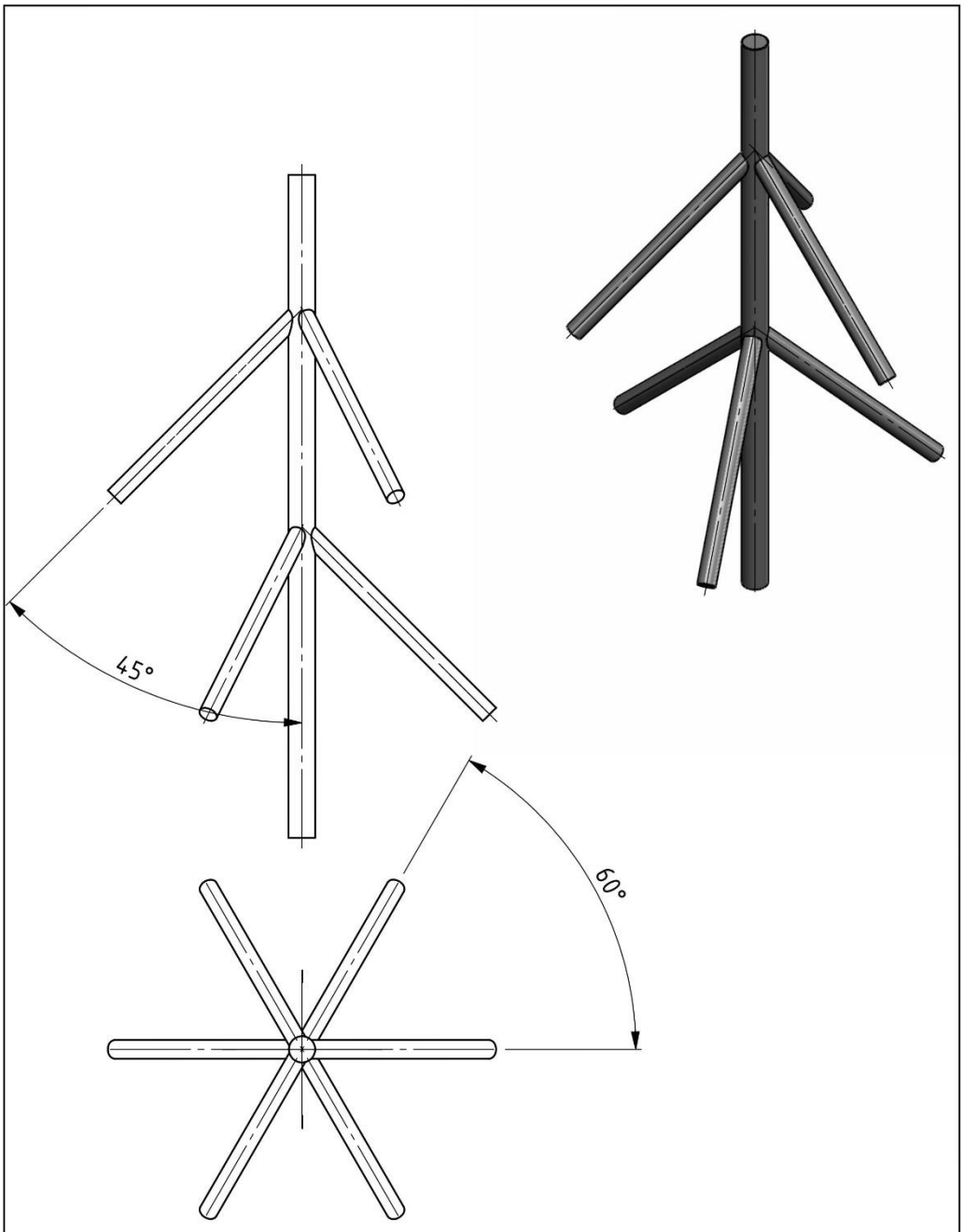

Figure 51: Technical drawing of Model 3 for mung bean roots, with specified parameters.

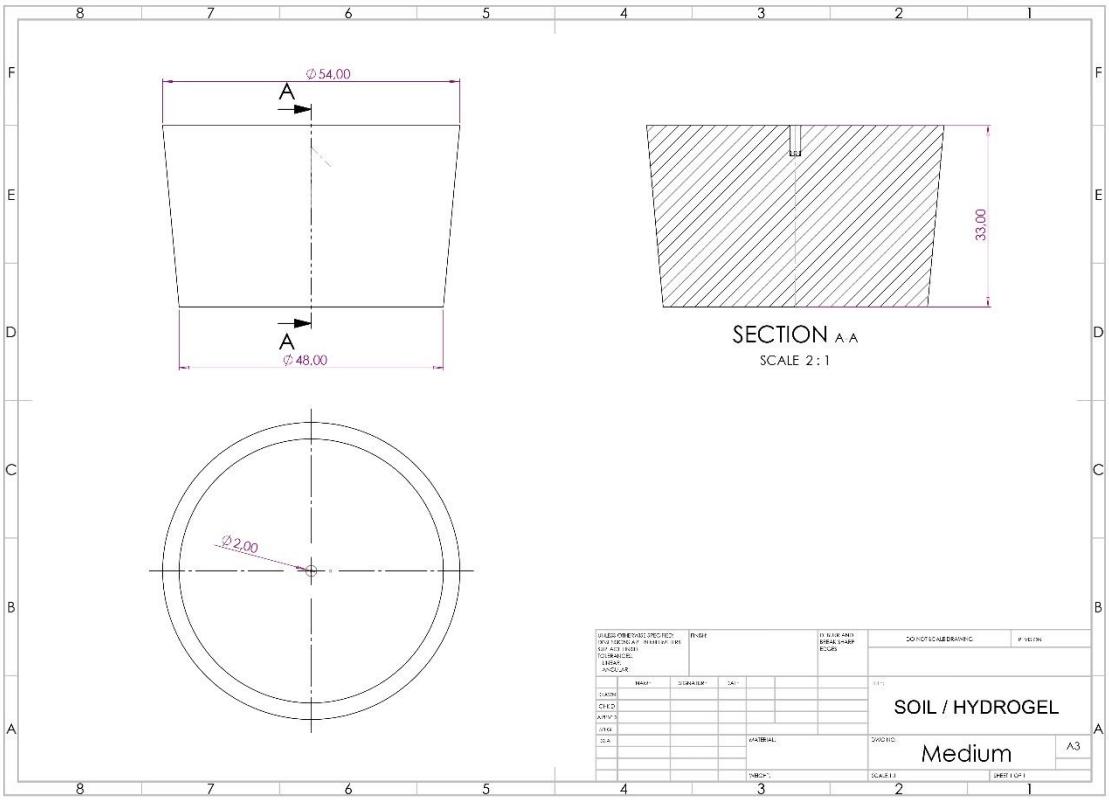

Figure 52: Technical drawing representing both the soil and hydrogel mediums, with specified dimensions and parameters.

Appendices related to Section 2.5: Hydrogel Protocol, Preparation and Planting Methodology.

Table 19: List of substances, suppliers, and product information for hydrogel preparation

Substances	Alginate powder	NPK Fertilizers	Calcium Carbonate	Glucono-delta-lactone	Antifungal
Supplier	Thermo Fisher Scientific	Hermie Online BV	Merck Sigma	Merck Sigma	Pireco
Product code	10468800	168431	239216	G4750	KOMO66414
Phase	Powder	Power	Power	Power	Liquid

Table 20: Comparison table for different protocol versions for hydrogel preparation and seed planting.

Protocol version 1	Protocol version 2	Protocol version 3
Powder preparation: Weigh the correct quantity of each powders with a weighing boat	***Powder preparation:*** 1. Weigh the correct quantity of each powders with a weighing boat 2. place the weighting boat containing the powders in a sealed container 3. sterilize the powders under UV light for 20 minutes *Note: don't open sealed container until next use*	***Powder preparation:*** 1. Using individual weighing boats, weigh the correct quantity of each powder separately 2. place the weighting boats containing the powders in a sealed container 3. sterilize the powders under UV light for 20 minutes *Note: don't open sealed container until next use*
Gel preparation: 1. Grab a sterilized container and fill it up with distilled water 2. add NPK and sodium alginate powder 3. mix manually with a sterilized spatula, then insert magnetic stirrer rod and seal container with a cap 4. leave on magnetic stirrer for 6 to 8 hours 5. once is ready leave in the fridge overnight *Note: magnetic stirrer setting - speed: 2,5 / temp: 0 (valid for all 3 protocol version)*	***Gel preparation:*** 1. grab a sterilized container, fill it up with distilled water and seal it 2. measure the correct amount of antifungal needed 3. add NPK, sodium alginate powder and antifungal 4. mix manually with a sterilized spatula, then insert magnetic stirrer rod and seal container with a cap 5. leave on magnetic stirrer for 6 to 8 hours 6. once is ready leave in the fridge overnight *Note: steps 2-4 are performed in the fume hood*	***Gel preparation:*** 1. grab a sterilized container, fill it up with distilled water and seal it 2. measure the correct amount of antifungal needed 3. add NPK, sodium alginate powder and antifungal 4. mix manually with a sterilized spatula, then insert magnetic stirrer rod and seal container with a cap 5. leave on magnetic stirrer for 6 to 8 hours 6. once is ready leave in the fridge overnight *Note: steps 2-3 are performed in the fume hood*
Crosslinking step: 1. grab a sterilized container and fill it up with distilled water 2. add calcium carbonate powder to the distilled water 3. mix manually with a spatula until obtaining homogenous solution 4. repeat the step 1-3 with GDL 5. in the beaker with gel solution add calcium carbonate solution 6. mix it manually with a spatula until homogenous 7. in the same beaker add GDL solutions 8. mix it manually with a spatula until homogenous 9. with a 1ml syringe withdraw some hydrogel 10. seal the beaker with parafilm and leave it in the fume hood until ready	**Crosslinking step:** 1. grab a sterilized container, fill it up with distilled water and seal it 2. add calcium carbonate powder to the distilled water 3. mix manually with a spatula until obtaining homogenous solution and seal the beaker 4. repeat the step 1-3 with GDL 5. in the beaker with gel solution add calcium carbonate solution 6. mix it manually with a spatula until homogenous and seal it 7. in the same beaker add GDL solutions 8. mix it manually with a spatula until homogenous 9. with a 1ml syringe withdraw some hydrogel 10. leave the beaker and syringe in the green house until ready *Note:* - *steps 2-10 are performed in the fume hood* - *previously clean and disinfect green house with ethanol*	**Crosslinking step:** 1. grab a sterilized container, fill it up with distilled water and seal it 2. add calcium carbonate powder to the distilled water 3. mix manually with a spatula until obtaining homogenous solution and seal the beaker 4. repeat the step 1-3 with GDL 5. in the beaker with gel solution add calcium carbonate solution 6. mix it manually with a spatula until homogenous and seal it 7. in the same beaker add GDL solutions 8. mix it manually with a spatula until homogenous 9. leave the beaker in the green house until ready *Note:* - *steps 2-9 are performed in the fume hood* - *previously clean and disinfect green house with ethanol*
Planting the seed: 1. place the seed in water in a sealed container 2. with a scalpel make a hole in the hydrogel 3. with tweezer grab the seed and insert it in the hydrogel 4. with the 1ml syringe fill up the hole made in hydrogel 5. put the beaker in the green house *Note: leave the seed in water for a min 8 hours to a max of 24 hours (valid for all 3 protocol version)*	***Planting the seed:*** 1. place the seed in water in a sealed container 2. sterilize the seed (used both ethanol and bleach solutions) 3. with a scalpel make a hole in the hydrogel 4. with tweezer grab the seed and insert it in the hydrogel 5. with the 1ml syringe fill up the hole made in hydrogel 6. put the beaker in the green house *Note:* - *steps 1-5 are performed in the fume hood* - *green house has HEPA filter to cover air entries*	***Planting the seed:*** 1. place the seed in water in a sealed container 2. sterilize the seed (used only bleach solution) 3. with tweezer grab the seed and insert it in the hydrogel 4. put the beaker in the green house *Note:* - *steps 1-5 are performed in the fume hood* - *green house has HEPA filter to cover air entries*

Table 21: Step-by-step procedure for hydrogel preparation

#	Step	Risk	Solution
	PREPARATION POWDERS		
1	weigh the correct quantity of powders: • Sodium alginate • NPK • Calcium Carbonate • GDL	Contaminated powder	UV-sterilize powder
2	place the weighting boats containing the powders in a sealed container	Contaminated container	Use pre-sterilized container
3	sterilize the powders under UV light for 20 minutes	-	-
	PREPARATION GEL		
1	grab a sterilized container, fill it up with distilled water and seal it	Contaminated container	Use pre-sterilized container
2	measure correct amount of antifungal needed and add with NPK and sodium alginate to the distilled water	Remark: Minimize the time the containers are open, ensuring they are sealed immediately after any access to prevent air contamination	
3	mix manually with a sterilized spatula, then insert magnetic stirrer rod and seal container with a cap	Contaminated equipment	Use sterilized equipment
4	leave on magnetic stirrer for 6 to 8 hours (speed: 3 – temp: 0)	No risk – sealed container	
5	leave in the fridge overnight	No risk – sealed container	
NB: *steps 2-3 are performed in the fume hood*			
	CROSSLINKING		
1	grab a sterilized container, fill it up with distilled water and seal it	Contaminated container	Use pre-sterilized container
2	add carbonate calcium powder to the distilled water	Remark: Minimize the time the containers are open, ensuring they are sealed immediately after any access to prevent air contamination	
3	mix manually with a spatula until obtaining homogenous solution and seal the beaker	Contaminated equipment	Use sterilized equipment
4	*repeat the step 1-3 with GDL*		
5	in the beaker with gel solution add carbonate calcium solutions (water + calcium)	-	-
6	mix it manually with a spatula until homogenous and seal it	Contaminated equipment	Use sterilized equipment
7	in the same beaker add GDL solutions (water + GDL)	-	-
8	mix it manually with a spatula until homogenous	Contaminated equipment	Use sterilized equipment
9	put the beaker in the green house	Contaminated environment	Ensure the greenhouse is sealed, sterilized and openings covered with hepa filters
NB: *steps 2-9 are performed in the fume hood*			

Table 22: Step-by-step procedure for planting the seed

#	Step	Risk	Solution
	PLANTING SEED		
1	place the seed in water for 8 to 12 hours in a sealed container (max 24 hours)	Contaminated water	Distilled water
2	sterilize the seed	Contaminated seed	Use sterilization methods (e.g., bleach or ethanol)
3	with tweezer grab the seed and insert it in the hydrogel	Contaminated tools	Use sterilized tweezers
4	put the beaker in the green house	Contaminated environment	Ensure the greenhouse is sealed and cover the opening with Hepa filters
NB: *steps 3-4 are performed in the fume hood*			

Appendices related to Section 3.4: FEM Simulation Results, Comparison between FEM result and pullout test

Another post-processing step involved comparing one of the plots from the FEM simulation in soil with data from an actual pullout test. To ensure comparability, the two most similar configurations were selected. The 45° configuration from the FEM simulation was chosen and compared to the tensile test results for barley sample B1, which had a length of 17.9 mm, close to the model's length of 20 mm. Additionally, given the short stem of sample B1, it is likely that root development was minimal, with no secondary branches, aligning well with the characteristics of the selected FEM model. The comparison of the force vs. displacement plots from both sources in shown in Figure 53. Both plots display a linear increase in force up to the peak, followed by a gradual decrease. The FEM simulation reached a maximum force of approximately 5 N, while the tensile test reached around 1 N. The displacement at maximum force was about 1 mm in the FEM simulation and around 2.6 mm in the tensile test.

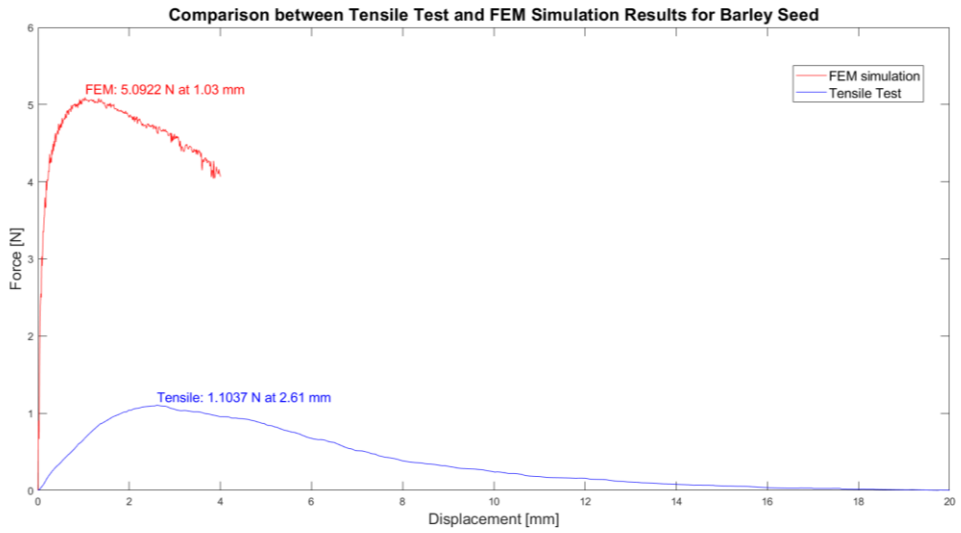

Figure 53: Resulting force vs. displacement plot comparing barley data from the FEM simulation with a 45° configuration in soil and the tensile test for sample B1.

For mung bean, a comparison was also made between one of the FEM models tested in soil and a result from the tensile tests. Test M4 was selected for comparison due to its stem length of 119.8 mm, suggesting, as noted in section 3.1, that it likely developed a taproot with secondary branching points. Consequently, the branch model was chosen from the FEM simulations to ensure compatibility with M4. Figure 54 illustrates the force vs. displacement plots from both the simulation and the tensile test. Both plots feature a linear increase in force up to a peak, followed by a decrease. In the FEM simulation, the maximum force reached approximately 9 N, while in the tensile test it was around 1.3 N. The displacement at maximum force was about 2.5 mm in the simulation, compared to 3.4 mm in the tensile test.

The main goal of this comparison was to evaluate how well the FEM model could approximate the general force-displacement trend seen in real root systems. While the FEM model captured certain aspects of the force-displacement trend, discrepancies were also observed. These findings indicate that, although the model serves as a functional framework, refinements are needed to improve its accuracy in simulating the mechanical responses of real root systems. However, the FEM simulations consistently resulted in significantly higher pullout forces than those observed in the tensile tests. This difference is likely due to the material properties used in the simulations, which were sourced from literature [43], whereas the tensile tests captured the actual intrinsic properties of the barley and mung bean roots. In both root system, the displacement at maximum force occurred earlier in the FEM simulations than in the tensile tests. This

difference can likely be attributed to several factors. Firstly, FEM models often simplify the root structure and material behavior to make simulations feasible. These simplifications can reduce the root's elasticity or ability to deform, causing maximum force to be reached at a smaller displacement compared to the real roots. Additionally, real-life root-soil interactions, such as root hairs, root exudates, and other micro-scale factors, provide additional anchoring and resistance in the tensile tests that the FEM model doesn't fully capture [92, 93].

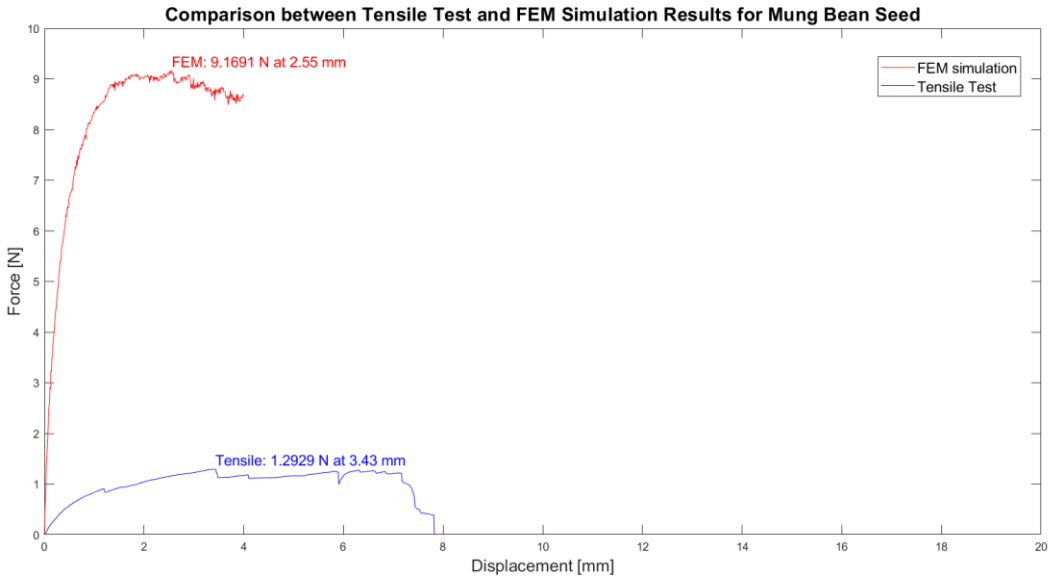

Figure 54: Resulting force vs. displacement plot comparing mung bean data from the FEM simulation with a branch configuration in soil and the tensile test for sample M4.

Appendices related to Section 3.5: Results on Root Growth in Hydrogel

Table 23: Summary of results for different protocol versions on fungal contamination in hydrogel.

Parameter	Protocol Version 1	Protocol Version 2	Protocol Version 3
Antifungal treatment	No	Yes	Yes
Fungal contamination	Yes	Yes	No
Number of sample contaminated	50 out of 50	4 out of 6	0 out of 46
Percentage of contaminated sample per batch	100%	~66%	0%

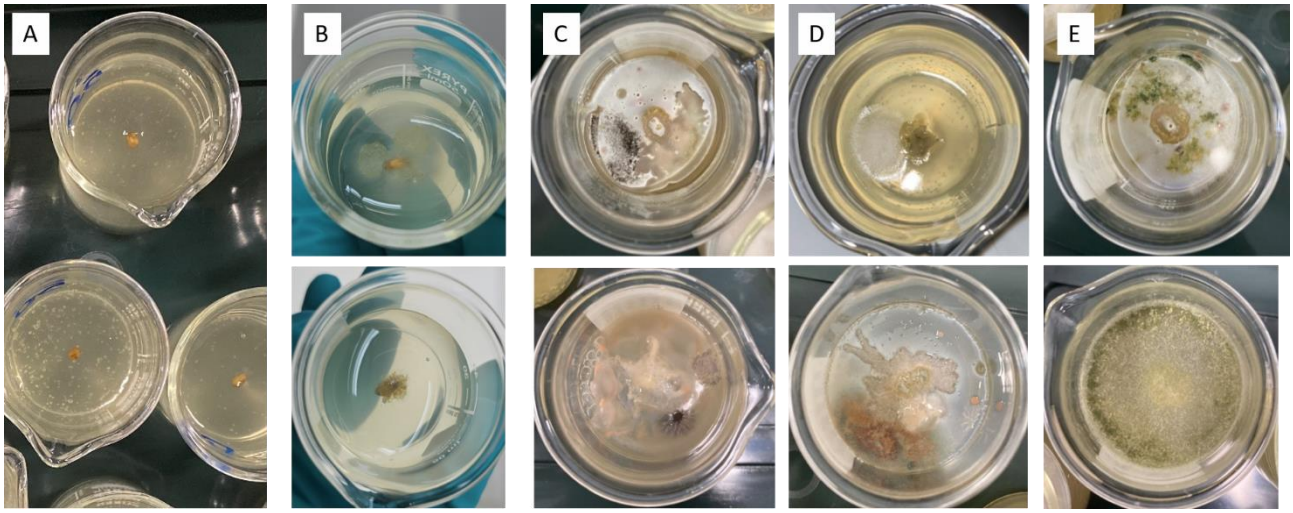

Figure 55: Pictures of fungal contamination for A) protocol version 3, B) protocol version 2 and C-D-E) for protocol version 1.